Energy Measurements in e-p Collisions at HERA Using the PLUG Calorimeter of the H1 Experiment

Dissertation

zur Erlangung des Doktorgrades
des Fachbereichs Physik
der Univesität Hamburg

vorgelegt von

Enrico Panaro
aus Catanzaro

Hamburg

1998

Gutachter der Dissertation : Prof. Dr. Dr. h.c. Gunnar Lindström
Prof. Dr. Hartwig Spitzer

Gutachter der Disputation : Prof. Dr. Dr. h.c. Gunnar Lindström
Prof. Dr. Robert Klanner

Datum der Disputation : 14.07.1998

Sprecher des Fachbereichs Physik und
Vorsitzender des Promotionsausschusses : Prof. Dr. Bernhard Kramer

Abstract

The following work presents an experimental analysis based on data collected during 1994 using the H1 experiment at HERA. Particular enphasis is given to the data analysis of the PLUG calorimeter of the H1 detector.
The most important technical aspects and the performances of the PLUG like stability, energy calibration, response linearity and energy resolution within the configuration of H1 are discussed. From the analysis of the data results that the energy-measurement performance of the calorimeter is limited by the inactive material in front of it. The energy determination is achieved using an original correction technique based on the complete simulation of DIS events in the H1 detector. The PLUG energy resolution within H1 has been determined in the range between 10 and 110 GeV. From this determination it follows that, the energy measurement on a single event basis is possible for emitted energies from 30 to 110 GeV in the calorimeter acceptance. In this energy window the resolution improves with increasing energy varying from 80 to 35 %. The use of the PLUG as a calorimeter is demonstrated using the energy measurement of the hadronic final states of deep inelastic scattering events. The analyzed events belong to the region of the HERA phase space with $2.5 < Q^2 < 100$ GeV^2 and $10^{-5} < x < 10^{-2}$. The transverse energy flow measurement as a function of the pseudo-rapidity (η) is performed in both laboratory and center of mass (CMS) systems. The measurements cover the full H1 calorimeter system's acceptance. The part performed exclusively with the PLUG are in the pseudo-rapidity regions between $3.5 < \eta < 5$ in the laboratory system and between $-3 < \eta^* < -1$ in the CMS. The experimental data has been compared with different Monte Carlo models like HERWIG, ARIADNE and LEPTO. The results of these comparisons are presented in detail.

Kurzfassung

Die folgende Arbeit beschäftigt sich mit der Analyse von experimentellen Daten, die mit dem H1 Detektor bei HERA im Jahre 1994 aufgezeichnet wurden, wobei besonderes Gewicht auf das PLUG Kalorimeter gelegt wurde.
Die wichtigsten technischen Aspekte und die Eigenschaften des PLUG-Kalorimeters, wie z.B. Stabilität, Energiekalibration, Linearität und Energieauflösung werden dargestellt und diskutiert. Durch die Analyse der Daten zeigt sich, daß die Verwendung des PLUG-Kalorimeters zur Energiemessung durch das inaktive Material limitiert ist, das sich räumlich vor der PLUG Kalorimeter im H1 Detektor befindet. Die Energie im PLUG-Kalorimeter wird durch eine besondere Korrektur Technik, basierend auf einer vollständigen Simulation von DIS Ereignissen im H1 Detektor, bestimmt. Die Energieauflösung des PLUG-Kalorimeters im H1 Experiment wurde im Energiebereich zwischen 10 und 110 GeV bestimmt. Damit kann die Energie eines einzelnen Teilchens in dem genannten Energiebereich im H1 Detektor gemessen werden. In diesem Energiebereich verringert sich die Energie Auflösung mit wachsender Energie von 80 zu 35 %. Es wird gezeigt, daß das PLUG-Kalorimeter zur Energiemessung des hadronischen Endzustandes von tief inelastischen Ereignissen verwendet werden kann. Die Ereignisse wurden im Bereich $2.5 < Q^2 < 100$ GeV^2 und $10^{-5} < x < 10^{-2}$ selektiert. Der transversale Energiefluß als Funktion der Pseudo - Rapidität (η) wurde im Labor - und hadronischen Schwerpunktsystem gemessen. Diese Messung erstreckt sich über die volle geometrische Akzeptanz des H1 Kalorimetersystems. Der Bereich in Pseudorapidität von $3.5 < \eta < 5$ im Laborsystem und $-3 < \eta^* < -1$ im hadronischen Schwerpunktsystem wird ausschließlich von dem PLUG Kalorimeter überdeckt. Unterschiedliche Monte Carlo Modelle (wie z. B. HERWIG, ARIADNE und LEPTO) wurden mit den Messungen verglichen. Diese Vergleiche werden im Detail vorgestellt.

Contents

Chapter 1

Introduction

Since the end of the last century with the discovery of X-rays by Röntgen [1] and the electron by Thompson [2], scattering experiments represent the most successful tool for the investigation of the elementary structure of matter.
The determination of the atomic structure was initiated by Rutherford in the years 1910-11. He suggested a scattering experiment, carried out by Geiger and Marsden, in which α-particles from a radioactive source were scattered from thin gold foils. Rutherford interpreted the angular distribution of the scattered particles as an evidence of the point-like dimension of the nuclei.
Half a century later in the 1960's, Hofstadter and other authors [3] demonstrated the spatial extension of nuclei using the scattering of electrons with an energy of a few hundred MeV on fixed targets of matter. Nuclei themselves are composed of protons and neutrons (called nucleons) which were shown to have radii of the order of 10^{-15} m. The evidence of the nucleons sub-structure was demonstrated with a scattering experiment using also electrons with energies of about 3 GeV interacting on a fixed target [4]. These fundamental constituents were called *partons* by Feynman [5] and were later identified with quarks and gluons. The theory which describes the interaction between quarks and gluons is the Quantum Chromo Dynamics (QCD) which today represents the most credited theory of the strong interaction.

With the HERA machine at DESY [1] collisions between high energy electrons[2] and protons (ep) have been accomplished for the first time. HERA provides interactions between electrons with an energy of 27.5 GeV and protons of 820 GeV. This corresponds to a center of mass energy of $\sqrt{s} \simeq 300$ GeV available in the process and a squared four-momentum transfer [3] in the range $0 < Q^2 < 90200$ GeV^2, which would be equivalent to a lepton beam of ~ 45 TeV incident on a fixed target.
The region of phase space of the deep inelastic ep scattering covered at HERA extends the region covered by the existing lepton-nucleon fixed target experiments. Both variables, Q^2 and Bjorken-scaling variable x (defined later in 2.1), are more than two orders of

---

[1] Deutsches Elektronen Synchrotron

[2] In this work the generic name electron is used also for positron

[3] All kinematic variables are defined in the next section

magnitude higher than in the previous experiments. Using electron-proton scattering at HERA it is possible to study the structure of the proton in a new kinematic domain and resolve sub-structures with dimensions below 10^{-18} m.
The research program at HERA covers many of the most important fields of interest in high energy physics today with major efforts being performed in the study of:

- the structure of the proton and of the photon, including interactions mediated by a neutral colour object exchanging the vacuum quantum numbers (*diffraction* phenomena);
- the search for particles beyond the Standard Model (lepto-quark, Super Symmetric particles) up to a mass of 300 GeV/c^2;
- the test of the Standard Model, of the electro-weak interactions and the study of effects mediated by virtual new particles which extend the search of particles with mass larger than the nominal center of mass energy achieved at HERA [6, 7].

The momentum asymmetry of the beams, leading to a center of mass (CM) momentum of $\sim$ 790 GeV/c in the proton (forward) direction, affects aspects of the event topology and kinematics and has therefore influenced the design characteristics of the detectors at HERA.
High energy fluxes and high particle multiplicities are produced particularly in the proton direction [4]. For these reasons, the detectors of both experiments, H1 and ZEUS, possess asymmetric structures with larger detector depths in the proton direction. The detectors of the H1 and ZEUS experiments cover almost the full solid angle around the interaction point. To investigate the recoiling hadrons in the region close to the proton remnant, the H1 detector is instrumented with a Silicon-Copper sampling calorimeter (PLUG) covering small polar angles with respect to the proton direction. The coverage of small angles around the beam pipe is not possible using a liquid argon calorimeter like the main calorimeter of H1. The PLUG is placed between the beam pipe and the return yoke of the H1 magnet. By using the PLUG the acceptance of the H1 main calorimeter is extended from $\eta = 3.5$ to $\eta = 5$ units of pseudo-rapidity [5].
The present work is based on the analysis of experimental data collected by the H1 detector, in the 1994 luminosity run period and on related Monte Carlo (MC) simulations. The principal purpose of the work is to show, how the PLUG calorimeter can be used to complement the energy measurement of the hadronic final state in the forward region of the H1 detector.
A further possibility offered by the PLUG, connected with the triggering and selection of the Large Rapidity Gap (LRG) events is not investigated in this work. The LRG events are an indication of interactions mediated by neutral colour exchanged objects. The use of the PLUG data in the LRG events analysis is already matter of extensive studies within the H1 collaboration [8].

---

[4] With the exception of the large rapidity gap events

[5] The pseudo-rapidity being defined as: $\eta = -\ln\tan\frac{\theta}{2}$ where θ is the angle between the outgoing proton and the scattered particle

The performance of the PLUG as a calorimeter within H1 has been investigated. The limitation on the energy resolution and of the detection efficiency of the primary particles has been demonstrated to be a consequence of the inactive material placed between the interaction point and the calorimeter itself. Several corrections necessary to fulfill the energy measurement have been presented. These are based on the detailed studies of the PLUG response and related simulations.

This work is structured as follows: the chapter 2 contains an introduction to the theory of electron-proton scattering with a short overview of the deep inelastic scattering and of the strong interactions. In its last section different Monte Carlo models of the expected deep inelastic scattering reactions are presented. The event simulations related to these models are later compared with the experimental data. Chapter 3 gives a short technical description of the HERA collider with its performance and of the H1 detector main sub-systems within the configuration of 1994. In the last section the main reasons motivating the construction of a forward calorimeter are presented.
The first part of chapter 4 is devoted to the design and to the technical characteristics of the PLUG calorimeter. The second part contains the data reconstruction procedure and the monitoring of data stability during the full 1994 luminosity period of proton/positron running. The quality of the produced data, upon which the subsequent energy measurements are based, is analyzed in detail using randomly triggered monitor events.
In chapter 5 the energy calibration procedure is presented and the error on the calibration is discussed. The energy measurement of the primary particles is demonstrated to be hampered by the large amount of inactive material present in front of the PLUG calorimeter. To permit the energy measurement of the primary particles a particular technique is introduced. The technique leads to a substantial improvement of the energy measurement. This is demonstrated by the comparison of data and Monte Carlo simulations before and after applying the correction technique. Several detail on the developed correction and on the energy resolution to support the reliability of the PLUG energy measurements are also shown.
Chapter 6 contains the physics analysis starting from the data selection. The analysis presents the transverse energy flow determination in the laboratory and in the hadronic center of mass systems up to a region of pseudo-rapidity never reached before at HERA. The measurement covers a large region of the HERA phase space including events with $2.5 < Q^2 < 100$ GeV^2 and $10^{-5} < x < 10^{-2}$. In order to achieve such a large coverage, data samples originated from both nominal and shifted interaction points of the colliding beams have been used. Using the data sample with shifted interaction point in the forward direction, the acceptance of the H1 detector is also shifted. To the enhancement of the backward acceptance of the H1 detector from $\theta = 173^o$ to $\theta = 176^o$ corresponds the extension of the measurable phase space and a very small reduction from $\theta = 0.6^o$ to $\theta = 0.72^o$ of the acceptance in the forward direction.
A particular emphasis on the measurements is given to the very low x region of the phase space. In this region the hadronic final state measurements may represent a test between the different evolution equation of the perturbative QCD and extend the understanding of the parton dynamic within the hadronic matter.
Chapter 7 contains conclusions from the achieved results and the outlook for the possible future use of this type of detectors.

Chapter 2

Physics background

2.1 Kinematic of the electron-proton scattering

The HERA machine provides the conditions for the study of a large spectrum of physics processes originating from electron-proton collisions. Two multi-task experiments H1 and ZEUS have been built and are operating for investigations regarding the high energy ep scattering.

Experimentally in a such scattering experiment it is possible to consider two different types of measurements: the exclusive and the inclusive. In the first type all particles produced in the final state with their relevant physical values are measured. In this case a specific process can be analyzed by excluding other different processes (therefore exclusive). Examples of reactions for which an exclusive analysis is possible are all the elastic productions of mesons in which all the final state particles are recognized and their 4-momenta are measured.

An interesting example is the pion production with charge exchange:

$$e \; + \; p \longrightarrow e' + \pi^+ + n$$

in which the particles in the final states can be detected providing a forward calorimeter around the beam pipe to tag the neutron in coincidence with the pion detection in a tracking chamber detector and the scattered electron in an electromagnetic calorimeter. In these events, it is possible to measure the production cross section of the identified particle and to study its *profile* (mass, quantum numbers etc.) given certain production conditions, such as for example the center of mass energy of the colliding particles.

On the other hand the inclusive measurement may include many types of reactions. The case of a neutral-current exchange reaction is usually represented as follows:

$$e \; + \; p \longrightarrow e' + X$$

In this reaction the final product X includes all detected particles apart from the scattered lepton e'. The final state X can be treated formally as one particle; therefore one 4-momentum, one mass and one of every other quantum numbers can be associated with this complex system X. The kinematic of the collision is in this case determined also with high precision, but on the other hand the particular properties of the final states X like particle multiplicity, type and individual 4-momenta of each particle which compose the state X are not measured in detail. Thus a certain state X may be produced by many different underlying configuration considered for this measurement as equivalents.

The measurements presented in this work concern inclusive measurements of the neutral-current deep inelastic scattering data sample. The relevant physics variables, observables and the theoretical background related to the measurements at HERA are introduced in the following.

The electron-proton scattering can be studied using a set of kinematic variables measurable in the detector. Using two of these variables and the invariant mass of the system, the kinematic of the collision is completely determined. Usually two variables are sufficient to describe two body scattering, but for high values of momentum transfered the proton is a composite object in which the struck quark takes a part of the proton momentum. Therefore in order to consider this further degree of freedom a third variable is necessary to determine the event kinematics.
To describe different aspects of the process kinematics and to characterize the different regimes, the following Lorentz invariants are used:

- the total invariant mass squared s
- the invariant mass of the hadronic system W
- the square of the four-momentum transfer q^2 or $Q^2 = -q^2$
- the Bjorken scaling variable x, which in the infinite momentum frame of the proton represents the longitudinal momentum fraction carried by the struck quark compared to the proton
- y the energy fraction lost by the incoming lepton in the rest frame of the proton

Refering to the 4-momenta of the particles in the initial and final state as shown in figure 2.1 the presented variables are defined as follows:

$$s = (\mathbf{k} + \mathbf{p})^2 \tag{2.1}$$

$$W^2 = (\mathbf{q} + \mathbf{p})^2 = \frac{1-x}{x}\, Q^2 + M_p^2 \tag{2.2}$$

$$Q^2 = -\mathbf{q}^2 = -(\mathbf{k} - \mathbf{k}')^2 \tag{2.3}$$

$$x = \frac{Q^2}{\mathbf{2p} \cdot \mathbf{q}} = \frac{Q^2}{2M_p\nu} \qquad \text{where} \qquad \nu = E_e - E_e' \tag{2.4}$$

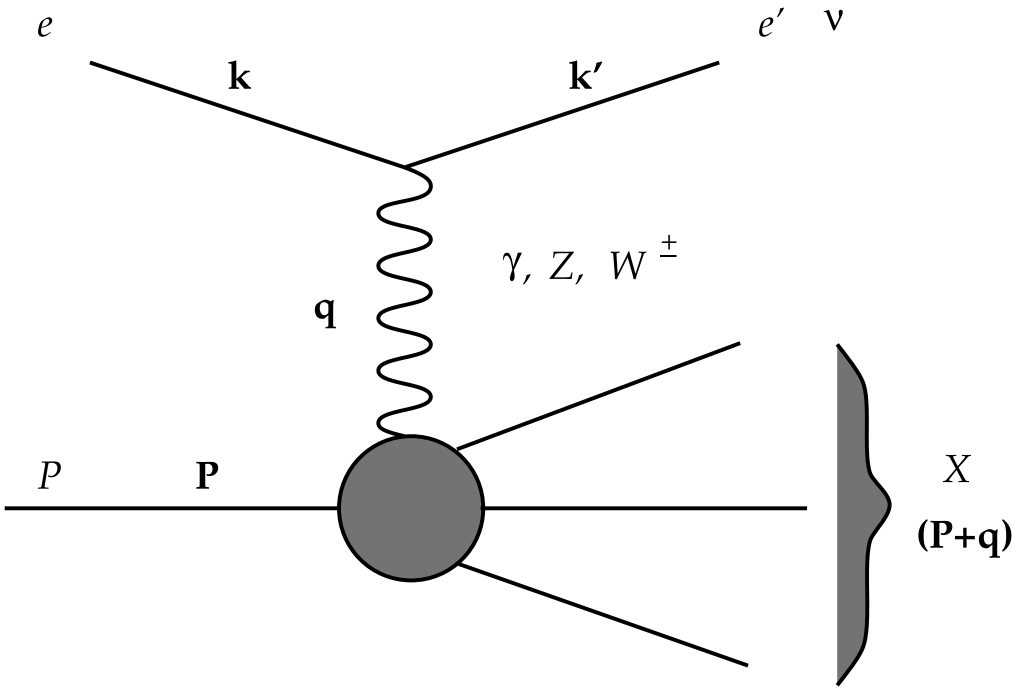

Figure 2.1: *Lowest order e-p scattering representation. The characters in bold indicate the momentum 4-vectors. The particles are indicated with normal characters.* W^+ *and* W^- *are the exchange particles in the charged current reactions.*

$$y = \frac{\mathbf{p} \cdot \mathbf{q}}{\mathbf{p} \cdot \mathbf{k}} \tag{2.5}$$

An initial classification of the processes can be performed using the square of the four-momentum transfer. The different values of Q^2 can be used to identify regions of the phase space in which the scattering amplitude and therefore the cross-section must be calculated with different approaches. It is possible to define a photo-production regime in the region where Q^2 is within the interval $10^{-8} < Q^2 < 10^{-1}$ GeV^2, a transition region in the range $10^{-1} < Q^2 < 1$ GeV^2 and a Deep Inelastic Scattering (DIS) domain defined for even higher values of Q^2.

Experimentally events belonging to the different Q^2 intervals present differing event topologies. The total cross section behavior $\sigma_{tot}(\gamma^* p)$ as a function of W^2 is shown in figure 2.2 . It presents large differences between events with different Q^2 and for a fixed values of the hadronic invariant mass the total cross section decrease when Q^2 increase.

2.2 Deep inelastic scattering and the quark parton model

On the contrary to the electron nucleon elastic scattering in which the kind and number of particles are conserved in the reaction, the deep inelastic scattering is generally char-

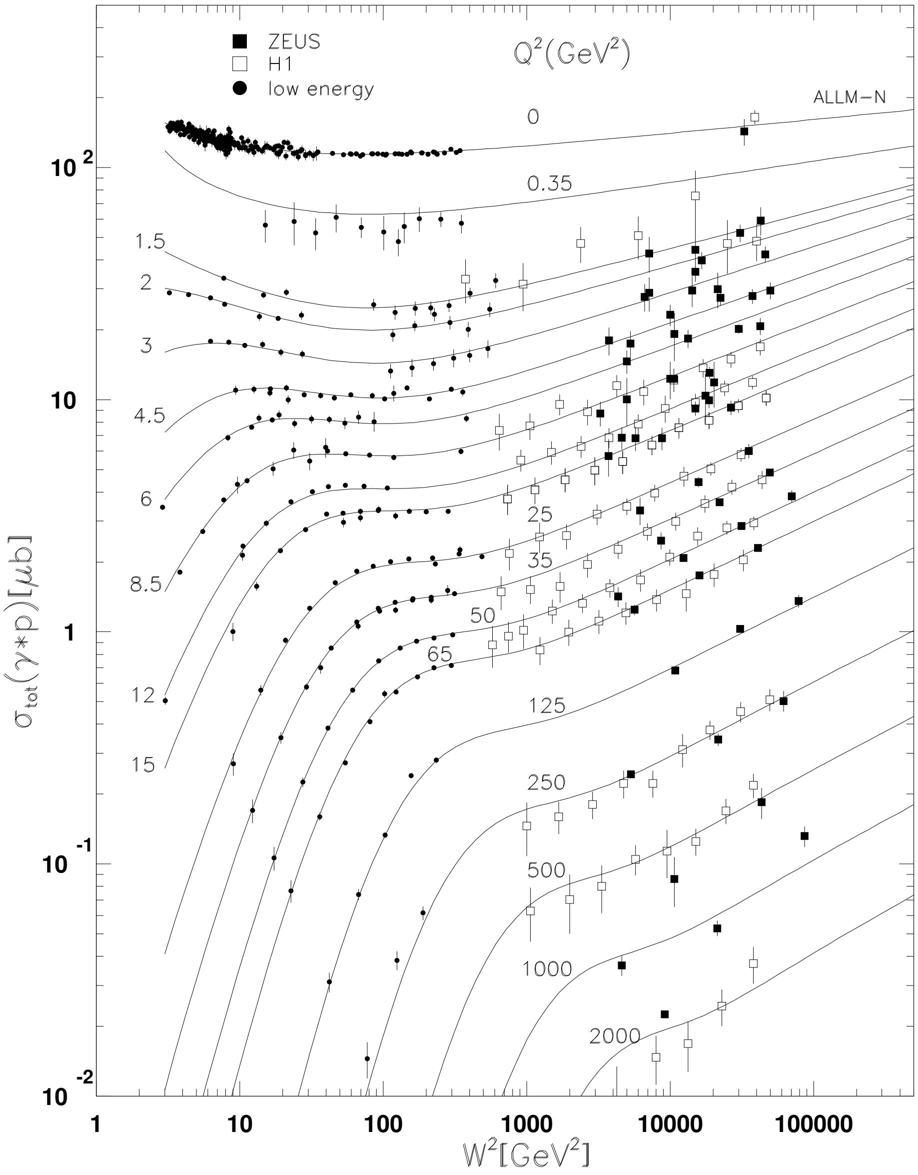

Figure 2.2: *Total e-p scattering cross section as a function of* W^2 *and* Q^2*. For real photons (*$Q^2 \simeq 0$ GeV^2*) the total cross section variation as a function of* W^2 *is limited between 100 and 200* μb*. Much larger variations are observable in the DIS regime for* Q^2 *larger than 10* GeV^2*.*

acterized by the destruction of the nucleon after the interaction with the production and detection of hadrons. This is an indication of interaction with the nucleon components, but the formal definition of DIS is operated through the value of the Q^2 involved in the reaction as stated in the previous section.

In the deep inelastic scattering experiments leptons are used to probe to investigate the structure of the nucleons. Examples of this kind of experiments are E665 at Fermi Laboratory, the European Muon Collaboration, CHARM coll., NMC and many others [9].

In the decade from 1960, experimental data from fixed target experiments using leptons as projectiles revealed that the cross section behaved in the same way as the cross section for scattering by a point-like nucleon with a charge less than unity. This behavior suggested that the lepton was scattered not by the whole nucleon, but only by a part of it, with a point like dimension as it was then proposed by Feynman.

In order to explain experimental results of the lepton-nucleon scattering, Feynman [5] proposed in 1969 the parton model of the nucleon. In this model he assumed that nucleons have a substructure and all constituents are identical having same charge. If the scattering is considered in a frame in which the nucleon is moving with a velocity close to that of light, c, the motion of the constituents of the nucleon will be retarded because of the relativistic time dilatation and the distribution of the charged partons will became disk-shaped as a result of the Lorentz contraction. In this condition the impinging lepton will be scattered instantaneously and incoherently by a parton of the nucleon.

In this simple model the nucleon constituents are considered as non-interacting with each other. This model can be also considered the *lowest order* approximation of the electron-proton scattering at HERA.

The reaction shown in figure 2.1 using a simple diagram, includes charged and neutral-current interactions in the lowest order approximation. The charged current interaction occurs when the boson mediating the interaction transfers electric charge (W^+ or W^-), whereas in the second case the exchanged boson is neutral (γ or Z^0) and no charge is transfered.

Considering the neutral current interactions only, the ratio of the scattering amplitudes of the Z^0-exchange to that of the γ-exchange diagram is:

$$\frac{A_Z}{A_\gamma} \sim \frac{Q^2}{Q^2 + m_Z^2} \tag{2.6}$$

where m_Z is the the mass of the vector boson Z^0. For $Q^2 \ll m_Z^2 \simeq 8000\ GeV^2$ the probability for reactions with Z^0-exchange diagram can be neglected. The scattering amplitude in the limit of $M_{nucleon} \ll s$ is proportional to $1/Q^2$ and the differential cross section in the variables Q^2 and x in the approximation of one photon exchange takes the form:

$$\frac{d^2\sigma}{dQ^2dx} = \frac{4\pi\alpha^2}{Q^4}\Big[(1-y)\frac{F_2(Q^2,x)}{x} + \frac{y^2}{2}\frac{2xF_1(Q^2,x)}{x}\Big] \tag{2.7}$$

The differential cross section is expressed in terms of F_1 and F_2, the proton structure functions for inelastic scattering. Using the following relationship between the structure functions:

$$R = \Big[\frac{F_2(Q^2,x)}{2xF_1(Q^2,x)} - 1\Big] \tag{2.8}$$

where $R = \sigma_l/\sigma_t$ is the ratio of cross sections for the longitudinal and transversal polarized virtual photon, it is possible to rewrite the differential cross section in term of only one structure function :

$$\frac{d^2\sigma}{dQ^2dx} = \frac{2\pi\alpha^2}{xQ^4}\Big[2(1-y) + \frac{y^2}{1+R(Q^2,x)}\Big]F_2(Q^2,x) \tag{2.9}$$

Using the Callan-Gross [10] relation: $F_L(x) = F_2 - 2xF_1(x) \equiv 0$, valid in the frame of the parton model for large values of Q^2 and non interacting charged constituents of spin 1/2, the equation (2.9) simply reads:

$$\frac{d^2\sigma}{dQ^2dx} = \frac{4\pi\alpha^2}{xQ^4}\Big[1 - y + \frac{y^2}{2}\Big]F_2(Q^2,x) \tag{2.10}$$

Before the formulation of the parton model, J.D. Bjorken [11] had already shown that under certain assumptions the structure functions do not depend on Q^2 and are only functions of x. He analyzed the behavior of the simultaneous commutator of the electromagnetic field in quantum field theory and reached the conclusion that if $Q^2 \to \infty$, $\nu \to \infty$, and the ratio $\frac{Q^2}{2M\nu}$ remains constant, the function $F_2(Q^2,\nu)$ can depend only on the finite ratio of the two quantities, that is $x = Q^2/2M\nu$. Since x is dimension-less there is no more scale dependency of the structure functions. This effect, called scaling or scale invariance, was observed for the first time at the Stanford Linear Accelerator (SLAC) [12] (1968). The experimental data also showed evidence of the point-like structure of the nucleon constituents, in the Q^2 dependency of the cross section for inelastic scattering normalized to the cross section from a point like potential. In figure 2.3 showing the proton structure function $F_2(Q^2,x)$ as a function of Q^2 and x the scaling is clearly visible in the lower part of the plot. For a fixed values of x between 0.2 and approx. 0.05 the proton structure function is almost constant over 4 orders of magnitude in Q^2. The small deviation for high values of Q^2 derives from strong interaction radiative effects of the partons. In the same figure the Q^2 dependency of $F_2(Q^2,x)$ becomes stronger as x decreases: this effect is known as scaling violation and depends on the parton interactions in the nucleon.

The considered one photon exchange (see fig. 2.1) approximation succeeds in describing the electron-proton scattering if the structure function is provided. According to the parton model the cross section for inelastic e-p scattering can be described as an incoherent sum of elastic cross sections of electron-parton processes such as $e + q_i \to e' + q_i'$ where the parton is indicated with q_i. The cross section equivalence can be written in the form:

$$\frac{d^2\sigma(ep \to e'X)}{dQ^2dx} = \sum_i \int_0^1 \frac{d^2\sigma_i(eq \to e'q')}{dQ^2dx} f(x')dx' \tag{2.11}$$

where a parton density $f(x)$ has been introduced, such that $f(x)dx$ represents the probability of finding a parton having a momentum between x and $x + dx$. Thus it is possible to express the structure function in terms of parton density distributions. Using the further knowledge that the quarks and the partons have the same quantum numbers it is possible to identify partons with quarks and write the structure function as follow:

$$F_2^P(x) = \sum_i^{N_f}(e_i)^2 x \cdot f_i(x) \tag{2.12}$$

N_f indicates the number of quark flavours and e_i is the charge of the i-flavoured quark. From the momentum conservation follows the momentum sum-rule:

$$\sum_i \int_0^1 x f_i(x) \cdot dx = 1 - \epsilon \tag{2.13}$$

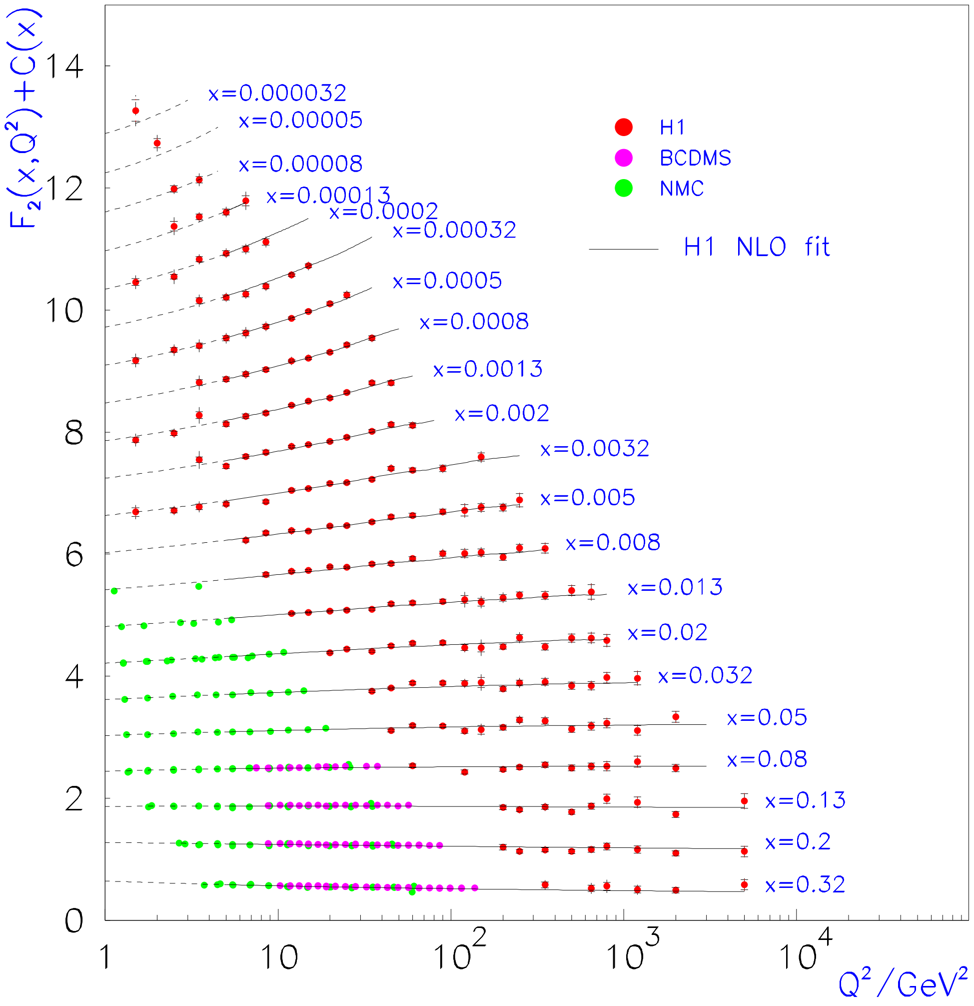

Figure 2.3: *Representation of the Proton structure function F_2 as a function of Q^2 for different x values. In order to emphasizes the different Q^2 dependencies for different values of x a function $C(x)$ is added to F_2 in the plot.*

where ϵ represent the momentum fraction of a nucleon which is not carried by quarks. Experimental results of the electron-nucleon scattering at SLAC over a wide range in Q^2 indicate that $\epsilon \sim 0.5$. This suggests that a large part of the proton momentum is carried by uncharged partons.

In the frame of the Quantum Chromo Dynamic theory (QCD) these neutral objects are identified with gluons; the quanta of the strong interaction. The QCD currently represents the best candidate theory to describe the strong interaction.

2.3 QCD and predictions in the perturbative regime

The Quantum Chromo Dynamic (QCD) is the theory which describes the interaction between quarks and gluons. The fundamental hypothesis of the QCD theory are the following:

- each quark exists in three different colours;
- by exchanging the colour between two quarks or gluons the interactions do not change; this means that the QCD is invariant under the $SU_c(3)$ transformation group[1];
- All hadrons are colour neutral;
- quarks and gluons cannot exist as free particles, they are confined into hadrons.

The gluons are the bosons of the colour field and since they also transport the colour they can interact with each other. This characteristic make the QCD a non-Abelian field theory. A consequence of the gluon-gluon coupling is that the coupling constant between quarks and gluons decreases with increasing squared momentum transferred, Q^2. The coupling constant α_s of the strong interaction thus depends on Q^2 and in the limit of Q^2 tending to infinity, $\alpha_s(Q^2) \to 0$ for $Q^2 \to \infty$. Such limit is called asymptotic freedom; in this limit (i.e. when Q^2 is large enough) the quarks interact only weakly with each other in a hadron so that it is possible to apply the perturbation theory in analogy with QED. In the frame of perturbative QCD it is possible to express the strong coupling constant as:

$$\alpha_s(Q^2) = \frac{12\pi}{(33 - 2n_f)log(\frac{Q^2}{\Lambda^2})} \qquad \text{with } \; n_f \leq 16 \tag{2.14}$$

Where n_f is the number of flavours and Λ is a scale parameter which is at present time not calculable in QCD and which must therefore be determined from experiments. The typical value of Λ determined form DIS and e^+e^- annihilation is between 100 and 500 MeV. The equation 2.14 represents the expression for α_s in the so called leading order approximation.

The calculation of higher order terms of the coupling constant depend on the renormalization scheme used. In the Next Leading Order approximation the QCD corrections interest α_s, but also the quarks and gluons density distributions. The dependency on Q^2 of the density distributions and therefore of the structure function can be calculated using the Dokshitzer Gribov Lipatov Altarelli Parisi (DGLAP) equations [14]. According DGLAP the dependency of the distribution functions on the variable $t = ln(Q^2/Q_o^2)$ with Q_o^2 as an opportune constant value, can be expressed using the following equations:

$$\frac{dq^i}{dt}(x,t) = \frac{\alpha_s(t)}{2\pi} \int_x^1 \frac{dy}{y} \left[\sum_{i=1}^{2N_f} q^i(y,t) P_{qq}(\frac{x}{y}) + G(y,t) P_{qG}(\frac{x}{y}) \right] \tag{2.15}$$

---

[1] The sub-script c in $SU_c(3)$ indicates that the symmetry group $SU(3)$ refers to the colour

$$\frac{dG}{dt}(x,t) = \frac{\alpha_s(t)}{2\pi}\int_x^1 \frac{dy}{y}\Big[\sum_{i=1}^{2N_f} q^i(y,t)P_{Gq}(\frac{x}{y}) + G(y,t)P_{GG}(\frac{x}{y})\Big] \tag{2.16}$$

In the equation 2.15 P_{qq} can be interpreted as the probability that a quark q_j radiates a gluon and decays into a quark q or P_{qG} that a gluon convert into a quark anti-quark pair $\bar{q}q$. In the eq. 2.16 describing the variation of the gluon density $G(t,x)$, P_{Gq} can represent the probability that a quark radiates a gluon or that a gluon decays into two other gluons. From the Altarelli Parisi equations it is possible to express the dependency on Q^2 of the structure function. The predictions of this calculation constitutes a crucial test of the Bjorken scaling hypothesis and of the perturbative theory. The equations 2.15 and 2.16 describe the perturbative development of the parton density distribution functions in the variable $(\alpha_s(Q^2)ln(Q^2/\mu^2))^n$. It is not possible to provide the x-dependency of the parton density from these equations, the x dependency should be assumed as known and parameterized within an interval around the value Q_o^2. Because of the collinear approximation in the DGLAP equations the transverse momentum of successive emitted partons must follow the scheme ($Q_o^2 << p_{\perp 1}^2 << p_{\perp 2}^2 << ... << p_{\perp n}^2 << Q^2$). The validity range of the DGLAP equations in LO approximation is given by the following conditions:

$$\begin{aligned} &\alpha_s(Q^2)ln(Q^2/Q_o^2) \simeq 1 \\ &\alpha_s(Q^2)ln(1/x) \ll 1 \\ &\alpha_s(Q^2) \ll 1 \end{aligned} \tag{2.17}$$

The prediction power of the DGLAP equations regards the evolution of the parton densities as functions of Q^2. The evolution of the parton density as a function of x can be calculated in the very low x range using the Balitski, Fadin, Kuraev and Lipatov (BFKL) evolution equation [15]. The BFKL equation represents the perturbative development of the parton densities as functions of the variable $(\alpha_s ln(1/x))^n$ with a fixed α_s. The validity range of this equation depends on the following condition which are almost complementary to those in eq. (2.17) for the DGLAP prediction:

$$\begin{aligned} &\alpha_s(Q_o^2)ln(Q^2/Q_o^2) \ll 1 \\ &\alpha_s(Q_o^2)ln(1/x) \simeq 1 \\ &\alpha_s(Q_o^2) \ll 1 \end{aligned} \tag{2.18}$$

2.4 Monte Carlo models for event descriptions

The simulation of electron-proton scattering events is of primary importance in order to extract physical quantities from experimental measurements at HERA.
The main reasons behind the implementation of Monte Carlo simulation are:

- the possibility to study the event topology and properties of particular physical processes; this enables the development of cuts to enhance the experimental sensitivity to processes of particular interest

- the evaluation of the non-perturbative part of strong interactions in building the final states (hadronization), giving rise to a better interpretation of measurements at partonic level with higher precision
- the possibility to compare data with the theory when the MC model reproduce the theoretical analytic results and correct the measurement against detector effects.

The simulation of the experiment, performed using the Monte Carlo (MC) techniques, consists of different stages. When the center of mass energy of the colliding particles is as high as it can be at HERA, it is useful to describe the reaction as an interaction of constituent particles. In this sense it is called hard sub-process the interaction of a constituent particle with the mediating particle having the square momentum Q^2 of the reaction. The following phases of the simulation can be considered:

1. the generation of the hard sub-process in which the strong interaction is involved,
2. the parton evolution before and after the hard sub-process,
3. the transition from parton to hadron called *hadronization* or *fragmentation*
4. the subsequent interaction of the particles with the detector components and the detector signal simulation (treated later in the section 5.4)

The first two steps are performed by a MC generator program. Multi-purpose MC generators usually contain the differential cross section for all relevant processes. The starting point of the event generation is the choice of the hard sub-process. In the case of a DIS process with an incoming (ij) and outgoing (kl) lepton parton pair, the total cross section can be expressed by the convolution of the differential cross-section with the appropriate structure function f^p:

$$\sigma_{ij\to kl} = \int\int dx d\hat{Q}^2 f_j^p(x,Q^2) \frac{d\hat{\sigma}_{ij\to kl}}{d\hat{Q}^2} \tag{2.19}$$

where x is the momentum fraction of p taken by the incoming parton j, $d\hat{\sigma}_{ij\to lk}$ is the differential cross section at partonic level and $\hat{Q}^2$ is the square four-momentum exchanged in the hard sub-process.

The electro-weak and QCD processes in leading order are included in the matrix element calculation of the sub-process. Since exact calculations of higher order processes in α_s are very complicated, the parton shower evolution of the initial and final state in Leading Logarithmic Approximation is used to take into account higher order contributions. A scheme for the simulation of ep events is illustrated in fig. 2.4. The use of MC generators using Final State Parton Shower (FSPS) has turned out to be rather successful in describing e^+e^- data from PETRA, PEP and LEP [16].
In the parton shower mechanism, partons with high virtuality evolve producing showers of partons with lower virtuality. The evolution variable (e.g. Q^2) decreases with every successive branching until a lower threshold is reached (usually $Q_o^2 \sim 1\ GeV^2$). This value

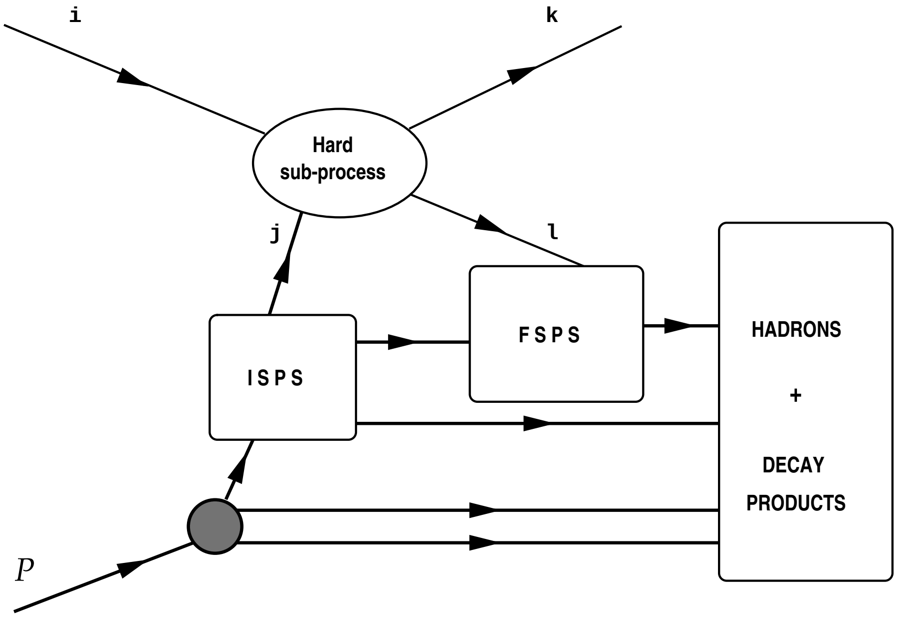

Figure 2.4: *Simplified simulation scheme of a MC event generator; when i and k represent the electron in the initial and final state the sketch illustrate a neutral current DIS event.*

sets the end of the perturbative evolution and of the first phase of the simulation. The branching algorithm is based on the Sudakov form factor:

$$S_a(Q^2, Q_o^2) = exp\Big(-\int_{Q_o^2}^{Q^2} \frac{dQ'^2}{Q'^2} \sum_b \int dz \frac{\alpha_s(Q'^2, z)}{2\pi} P_{a\to bc}(z)\Big) \tag{2.20}$$

$(1-S_a)$ represents the branching probability for a parton a with virtuality between Q_o^2 and Q^2, $P_{a\to bc}(z)$ are the Altarelli-Parisi splitting functions and z is the energy ratio between the partons b and c.

MC programs such as HERWIG, PYTHIA and LEPTO [17, 18, 19] make use of Parton Shower for the simulation of higher order QCD processes and therefore it is said that they represent the DGLAP evolution scheme.

In ARIADNE [20] an alternative way of describing higher order QCD corrections is used. In this Monte Carlo program the mechanism producing the parton radiation is based on the Colour Dipole Model (CDM). According to CDM a gluon g emitted from e.g. a $q\bar{q}$ pair, can be treated as radiation from the colour dipole between q and $\bar{q}$. The emission of a second softer gluon can be treated as radiation from two independent colour dipoles formed between q and g and that between g and $\bar{q}$. This procedure can be easily generalized to a large number of emitted gluons by following this scheme. The CDM used in the e^+e^- simulation is almost equivalent to the Parton Shower. In the case of DIS (lower order) the colour dipole extends itself between the *extracted* point like parton and the composite (therefore extended) proton remnant.

In electromagnetic theory, the emission of short wavelengths from an extended antenna

is suppressed in respect to that from an antenna of smaller size.
In an analogous manner in the colour dipole model, only a fraction

$$a = (\mu/p_\perp)^\alpha$$

of the proton remnant participates to the radiation emission. The parameter μ is proportional to the inverse of the proton remnant size, α (dimensionality of the emitter) is 1 when tuned to the EMC data [21] and $p_\perp$ the transverse momentum exchanged by two partons which form a dipole. For this reason the available phase space for radiation in the target region is reduced when compared with the parton production in e^+e^- annihilation. In CDM, coherence effects between the radiated gluons are automatically taken into account whereas in the Parton Shower mechanism it is necessary to introduce limitation to the angle between the parton and the emitted gluon. This properties of CDM has as consequence that the gluons along the ladder, between the proton and the sub-process (see fig. 2.5), are not ordered in k_t whilst the longitudinal momentum fractions x_i are ordered. This also happens in the evolution of the parton cascade using the BFKL evolution equation. For this reason ARIADNE, based on CDM, is an approximation of the parton evolution in the BFKL scheme [22] even if no BFKL equation is implemented in the ARIADNE MC generator.

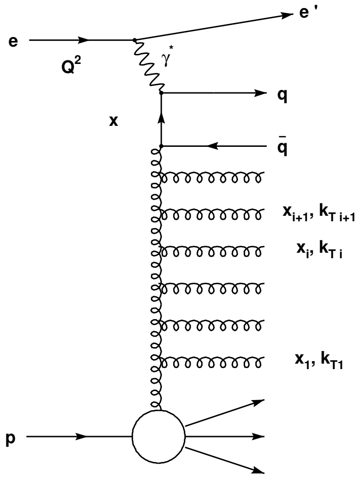

Figure 2.5: *Ladder diagram in the deep inelastic ep scattering.*

Hadronization

It has been shown, that the production of all partons in the event simulation can consist of a sub-process part calculated with the leading order matrix elements and of the evolution of the parton cascade. The last can be calculated according to the two schemes: the Parton Shower in Leading Logarithmic Approximation and the Colour Dipole Model.

The transformation of coloured partons into colour neutral hadrons is described in the hadronization using phenomenological models. This is because there is no satisfactory theory describing the impossibility to observe free quarks (quark confinement problem). Generally processes between partons at a scale where perturbation theory is not applicable, are included in the hadronization phase of the simulation.
The simulation of hadron formation and of the eventual decays are performed in the considered MC generator according to two models. The first is the Lund-String-Model implemented in the JETSET [23] program. This is used in all the considered MCs with the exception of HERWIG, which uses a second model called the Cluster Model [24].
In the Lund-String-Model a parton pair, in which the partons move in opposite directions, transfers part of the kinetic energy to the colour field connecting the partons. The colour field, which does not extend transversally (i.e. it is string-like), has a uniform energy per unit length and corresponds to a linear confinement potential between the partons. The potential has the simple form:

$$U = kd$$

with $k \approx 1\ GeV/fm$ and d being the distance between the partons. In the case of a $q\bar{q}$ pair, the increase of d and consequently of the potential energy, permits the production of a $\bar{q}q$ pair between the initial pair. The originating string can break off with the production of two colour singlet $q\bar{q}$ (mesons). Even if suppressed, the barion production is possible when a diquark anti-diquark is created in the colour field of the string. These hadronization mechanisms are schematically illustrated in fig. 2.6. The production ratio between the number of barions and mesons, can be experimentally determined and implemented in the program. In the model the conservation of the momentum, of the energy and of the quark flavour is valid in every phase of the hadronization process.

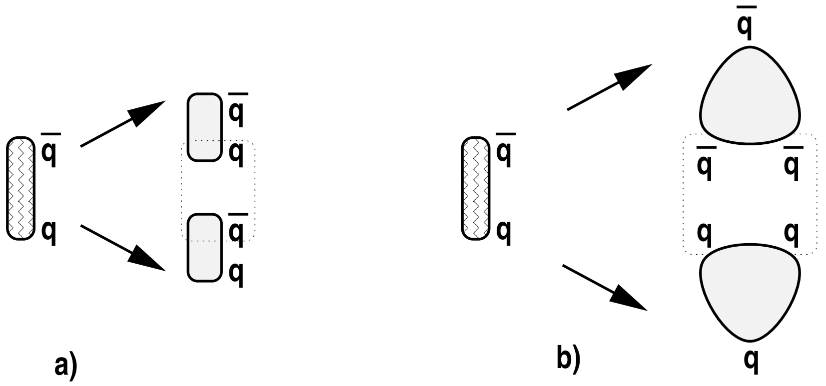

Figure 2.6: *Hadronization according the Lund-string-Model; a) fragmentation into a meson anti-meson b) fragmentation into a barion anti-barion.*

In the Cluster Model the gluons g, originating from parton branching, split non-perturbatively into $q\bar{q}$ pairs. Neighboring quarks and antiquarks can then combine in a colour singlet cluster. The cluster mass spectrum is steeply falling at high masses. The spectrum form depends on the QCD scale, Λ, the perturbative cutoff Q_o (see eq. 2.20) and, to a lesser extent on the non-perturbative gluon splitting [25]. The typical cluster masses are of the order of two or three times Q_o^2. The clusters decay isotropically in their rest frame into hadron pairs with branching ratios determined by the density of states.

Chapter 3

The H1-experiment

3.1 The HERA machine

The HERA[1] collider, built at the DESY laboratory in Hamburg consists of two separate accelerator-storage rings, one for protons[2] and one for electrons or positrons. The machine, located in an underground tunnel, is the world's first example of a hadron-lepton collider. HERA consists of four linear sections coupled by four circular sectors to give a total length of 6.336 Km. In the middle of each of the four straight sections large halls to house the experiments have been built.

The particle beams collide in the north (H1) and south (ZEUS) halls, and are held separate for fixed target experiments in the east (HERMES) and west (HERA-B) halls.

The protons and the electrons are produced and pre-accelerated in a machine system consisting of a linac and two synchrotrons in cascade for each beam. In figure 3.1 HERA and the complex chain of its pre-accelerators at DESY is shown. The particles are injected in HERA with momenta of 40 GeV/c (protons) and 12 GeV/c (electrons or positrons) respectively from the pre-accelerator PETRA. To permit a proton momentum of 820 GeV/c the proton ring is equipped with 696 super-conducting magnets, 280 quadrupoles and 416 dipoles, capable of obtaining a 4.65 T magnetic field when cooled with liquid helium to a temperature of 4.5 K. Conventional magnets are used to bend and focus electrons with momentum up to 30 GeV/c in the ring. To reach high beam currents and high luminosity it is possible to inject a maximum of 210 bunches of particles into each ring. A consequence of this characteristic is that the time interval between two bunch-crossings and therefore between possible consecutive events is $96 \cdot 10^{-9}$ s. This machine parameter is very important for the trigger and acquisition system of the experiments at HERA.

In order to permit the study of background effects in the detector $\sim 10\%$ of the bunches do not collide with other beam bunches; these are termed *pilot bunches*. In this case the protons or the electrons of the pilot bunch can interact only with the residual gas or the

---

[1] Hadron Electron Ring Anlage

[2] It is possible to accelerate also nuclei (light ions) albeit with lower intensity

Figure 3.1: *HERA and its pre-accelerator system at DESY.*

beam-pipe to produce particles in the detectors faking e-p collisions which can be in this way well studied. The rate of these background events at HERA is very high ($\sim$ 100 kHz) so it is important to recognize the topology of these events at trigger level to avoid over burdening the data acquisition with large amounts of unusable data.
In table 3.1 important parameters of the machine are shown. The development during the years of the integrated luminosity produced by HERA for the two collider experiment is summarized in table 3.2.

Parameter		design value		1994 value	
		e-ring	p-ring	e-ring	p-ring
beam energy	(GeV)	30	820	27.5	820
center of mass energy $\sqrt{s}$	(GeV)	314		300	
time between collisions	(ns)	96		96	
particle bunches per beam		210		153 + 15	153 + 17
Luminosity	($\mathrm{cm}^{-2}\mathrm{s}^{-1}$)	$1.5 \cdot 10^{31}$		$1.4 \cdot 10^{30}$	

Table 3.1: *HERA design and achieved performance parameters during 1994.*

Year	1993	1994	1995	1996	1997	Design
Integrated Luminosity (pb^{-1})	0.9	5.6	10.9	15.5	34	100

Table 3.2: *Integrated Luminosity produced at HERA per year.*

3.2 H1 detector

H1 is a multi-task detector with quasi 4π acceptance installed in the north hall of the HERA collider. The purpose of this complex instrument is to explore physics in the largest domain of the phase space accessible at HERA and to ensure as far as possible the detection and related measurements of all particles produced in the collisions.
The overall dimension of H1 is $12 \times 15 \times 10$ m^3 and its estimated weight is 2800 t. H1 consists of several sub-detectors built with an almost cylindric symmetry around the beam pipe. The sub-detectors can be grouped into systems according their function.
In H1 it is possible to measure: charge, charge density, momentum and direction of tracks in the tracker systems; the direction and the energy of charged and neutral particles using the calorimeter systems and to identify muons through the muon systems.
The position of each sub-detector is expressed in a right-hand coordinate system with the origin $O \equiv (0, 0, 0)$ coinciding with the nominal interaction point. The z-axis is parallel to the beam pipe and points in the proton direction while the x-axis is directed to the center of HERA ring. In the associated spherical coordinate system θ is defined as the angle between the generic vector and the z-axis and ϕ as usual the azimuthal angle in the plane x-y.
The following description of the detector components concern the configuration of H1 in 1994, a more comprehensive specification can be found in [26]. Figure 3.2 shows large part of the H1 detector schematically.

Tracker system

The inner tracking system consist of two major parts, the central and the forward tracker, and of the Backward Proportional Chamber BPC. The trackers are numbered in figure 3.2 as (2) and (3) while the BPC placed in front of the Backward Electro-magnetic Calorimeter (12) is visible in the picture but is not numerically indicated.

The central tracker consist of two cylindric concentric drift-wires chambers CJC1 and CJC2, of which CJC1 is the innermost. The chambers are placed symmetrically with respect to the interaction point with the wires parallel to the z-axis covering the polar angle regions of $15^o < \theta < 165^o$. With this device it is possible to determine the position of track points in the $r - \phi$ drift-plane with a spatial resolution of $\sigma_{r\phi} \sim 170\ \mu m$ and in the the z-direction using charge balance calculations, with a resolution of $\sigma_z \sim 3\ cm$. Between the two drift chambers and around the beam pipe there are 2 pairs of chambers. Each pair consist of a drift and a proportional chamber: the drift chamber being used to improve the track determination along z and the proportional chamber is fast and is used for the determination of the interaction time t_0. The precise track reconstruction and the presence of the magnetic field $B = 1.15\ T$ on the beam axis and parallel to the z-direction permits a transverse momentum determination with a resolution of $\sigma_{P_t}/P_t^2 \simeq 10^{-2}$ GeV^{-1}

The forward tracker covers the polar angle region between $7^o < \theta < 25^o$ and is divided into three super-modules along the z direction. Each module consists of drift chambers, divided into planars equipped with parallel wires along 3 different orientations, radials

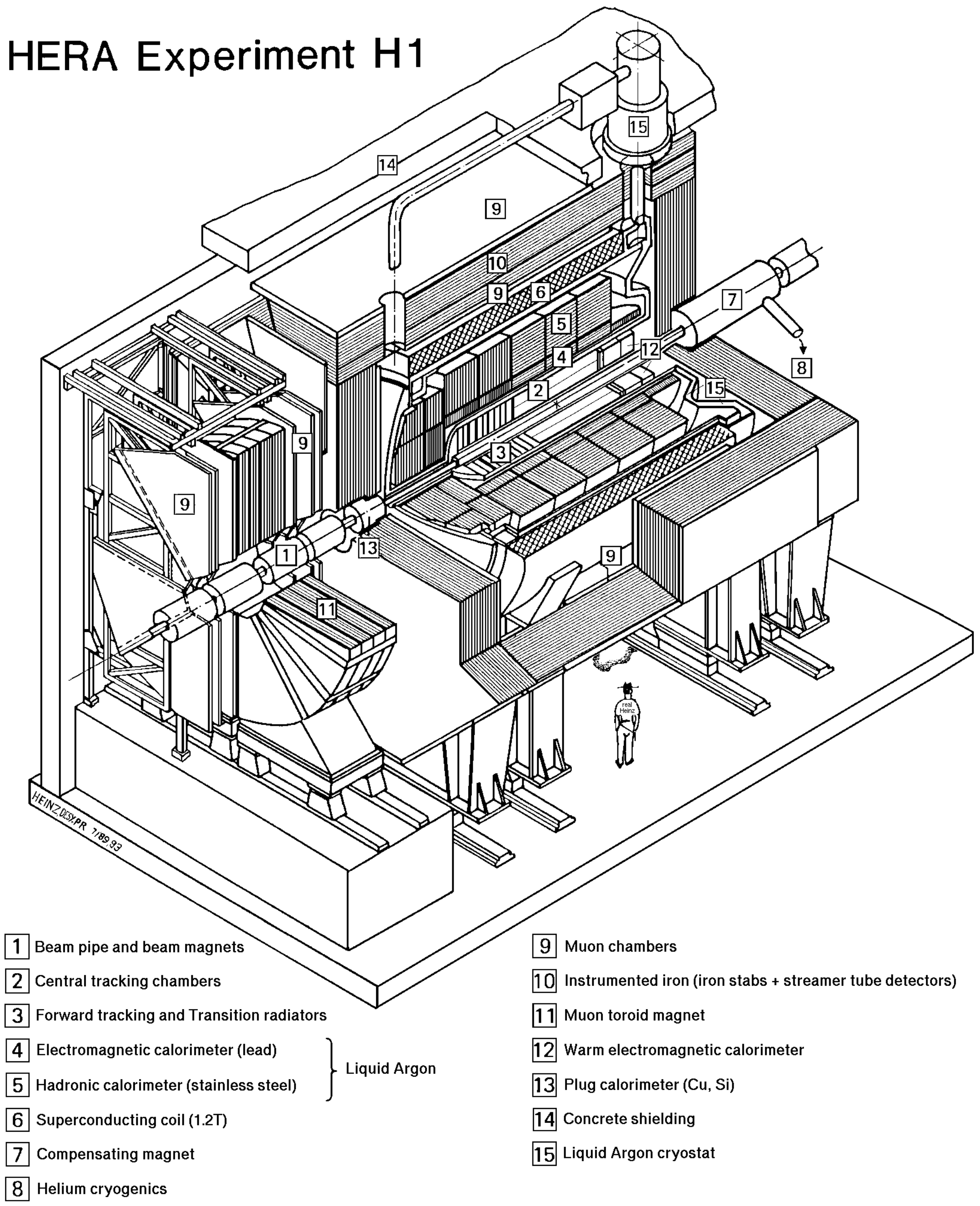

Figure 3.2: *3-D view of the H1 detector. The most important sub-systems are indicated with numbers.*

with radially strung wires, proportional chambers which produce signals for the trigger and of a transition radiation section to aid particle identification.
The precision on the spatial hit determination using the drift chamber is of $\sigma_{r\phi} \sim 170\ \mu$m and $\sigma_{xy} \sim 210\ \mu$ m. The full exploitation of the forward tracker detector is still hampered by the very high hit multiplicity, which makes track reconstruction in an acceptably short computing time a challenging task.

The backward tracking is completed with a multi-wire proportional chamber (BPC) which cover the region between $155^o < \theta < 173^o$. The spatial determination of the impinging charged particles can be made with 2-3 mm precision. Using this information in conjunction with the backward calorimeter and central tracker information, the scattered electron can be identified and its angle can be determined and used for the reconstruction of kinematic variables.

Calorimeters

For the energy measurement of very high-energetic particles and jets, the H1 detector is provided with a system of three calorimeters around the interaction point. A further outer calorimeter, the tail-catcher is described later together with the muon system which together improve the energy measurement for hadronic showers not contained by the calorimeters inside the solenoid.

Moving further out, radially from the interaction point, the next sub-detector is the Liquid Argon calorimeter. It is contained in a 2.8 m radius cryostat and is subject to the 1.15 T magnetic field provided by the H1 super-conducting solenoid (fig. 3.2 (4)(5)(6)). The calorimeter acceptance covers the region defined by $3.6^o < \theta < 154.8^o$ and the full azimuthal angle ϕ.
The calorimeter itself is of the sampling type and consists of eight separate wheels orthogonal to the z-axis. Beginning from the back or -z side, the wheels are named BBE, CB1-3, FB1-2 and F1-2. These names refers to the position in H1 according the scheme: Backward Barrel Electromagnetic, Central Barrel, Forward Barrel and Forward. Every barrel wheel is in the form of an eight-fold segmented wheel; the cracks between the octants are not radially projective in order to minimize inactive regions. The two forward wheels consist of two modules joined together along the vertical axis.
Apart from the BBE which has only an electromagnetic section and the F2 wheel which consists of a hadronic part, the six remaining wheels have both electromagnetic and hadronic sections.
The orientation of the layers in the sampling structure is chosen so that the particles impinge on the absorbers with angles larger than 45^o. This has relevance for the homogeneity of the calorimeter calibration.
The sampling structure for the electromagnetic section consists essentially in a 2.4 mm thick lead-absorber layer and of 2.35 mm gaps filled with liquid Argon as active medium, while in the hadronic part 16 mm thick stainless-steel layers are followed by 4.8 mm gaps. The sampling structures are constant over the whole calorimeter while the cell size and the calorimeter depth with respect to the interaction point varies as a function of θ. The

depth of the electromagnetic section expressed in the number of radiation lengths X_o, varies between $20 < N_{X_o} < 30$, and the longitudinal read-out segmentation between 3 and 4 . For the hadronic section the number of interaction lengths (λ) varies from 5 to 8 as θ decreases and the read-out segmentation varies between 4 and 6.
The high granularity of the calorimeter ($\simeq$ 45000 channels) permits good electron-pion separation and the recognition of the electromagnetic part of the hadronic shower due to electromagnetic decays of π^0 and ρ's. Thus using software weighting functions it is possible to achieve a response ratio of electromagnetic to hadronic $\frac{e}{h} \simeq 1$ even without hardware compensation [13] and also more uniform response to hadronic showers reducing large fluctuations [27].

The energy resolution to electrons is $\sigma_e(E)/E \simeq 0.12/\sqrt{E/GeV} \oplus 0.01$ and to hadrons $\sigma_h(E)/E \simeq 0.5/\sqrt{E/GeV} \oplus 0.02$. These values have been obtained in test beam experiments [27, 28].
The error on the energy scale has been evaluated on real data using the conservation of the transverse momentum in QED compton processes and DIS. The value is quoted $\sim 1\%$ to the electromagnetic and $\sim 5\%$ to the hadronic scale [83].

The Backward Electro-Magnetic Calorimeter (BEMC) indicated with (12) in fig. 3.2 is a Lead-scintillator sampling calorimeter. It covers the polar angle interval with θ between $153^o < \theta < 176^o$ and the full 360^o azimuthal range. The 88 stacks that comprise the calorimeter are assembled inside an aluminum barrel with a radius of 81 cm which fits inside the liquid argon cryostat together with the tracker system. The sampling structure consist of 2.5 mm lead alternated with 4 mm scintillator plates and the total depth expressed in number of radiation length X_o is $N_{X_o} \simeq 22$. This corresponds to about one interaction length ($\sim 1\lambda$). The electromagnetic showers originating from the scattered electron are completely contained whilst hadronic shower are only partially contained, the energy deposited in the calorimeter being on average 30% of the hadronic shower energy. The main task of the BEMC is the measurement of the scattered electron position and energy, the resolution can be expressed as $\sigma_e(E)/E \simeq 0.1/\sqrt{(E/GeV)} \oplus 0.01$ where the noise dependency has been neglected.

The PLUG calorimeter indicated with (13) in fig. 3.2 covers the acceptance region between the beam pipe and the liquid argon calorimeter, $0.6^o < \theta < 3.5^o$. A detailed description of this calorimeter follows in the next chapter.

Time of Flight scintillators

To reduce the rate of the proton induced background being triggered at the first level trigger (L1) two scintillating counter systems are placed upstream with respect to the nominal interaction point. The first system, ToF, is located behind the BEMC at z = -1.94 m and consists of two pairs of scintillator planes separated by Δz $\simeq$ 30 cm. The paired scintillators planes are separated by a lead layer to reduce the coincident noise induced by synchrotron radiation. The very high time resolution of the ToF $\sim 1-2$ ns permits the separation of proton induced background from events coming from the

interaction point. This is possible because, the particles generated upstream which travel in time with the proton bunch hit the ToF $\sim 13ns$ before the particles coming from the interaction region. Using the ToF signal in the trigger permits the vetoing of background events falling outside of the interaction time-window.
The second system, the Veto Wall, consists of two scintillators wall pairs placed at z $\simeq -6.5\ m$ and z $\simeq -8.1\ m$ which improve the background rejection efficiency and provide also information on the beam condition in a similar manner to the ToF scintillators. A further small time of flight system, the FToF is placed in the forward region at z $\simeq 7$ from the interaction points and is used to veto.

Muon system

This system provides the detection and when possible the momentum measurement of penetrating muons. The muon system consist of 16 layers of limited-streamer tubes covering the angular acceptance $4^o < \theta < 171^o$ and in the forward direction more layers of drift chambers together with a toroidal magnet form the Forward Muon Spectrometer (see fig. 3.2 (9)(10)(11)) with an acceptance of $3^o < \theta < 17^o$.
The planes of streamer tubes instrument the inner and outer muon chambers and the iron-yoke of the H1 solenoid. Muon chambers cover both the inside and outside of the iron-yoke; the chambers consist of three layers of streamer tubes. The instrumented iron-yoke consists of ten slabs stainless-steel (7.5 cm thick) interleaved with the remaining streamer tube layers. The central muon tracking system also constitutes a sampling calorimeter (tail-catcher) that can measure the hadronic shower leaking from the main calorimeters. The energy resolution to hadronic showers is $\sigma_h(E)/E \simeq 1.0/\sqrt{E/GeV}$.

Luminosity system

The main tasks of the luminosity monitors are the determination of the absolute luminosity in the beams interaction region and the tagging of the scattered electron at very low angles ($\theta \sim 180^o$) in the photo-production regime. Another use of the system is the detection and energy measurement of the photons related to events with emission of radiation in the initial state. In these events the resulting initial energy of the electron participating in the e-p scattering process is lowered with respect to the nominal beam energy.

The determination of the luminosity is performed using the Bethe-Heitler Bremsstrahlung process [29] $e+p \rightarrow e+p+\gamma$ for which the cross section is very well known. The luminosity monitor consists of two electromagnetic calorimeters one called electron tagger (ET) placed at z $= -33.4\ m$ and the second, the photon tagger (PT), placed at z $= -102.9\ m$. An absorber, to suppress synchrotron radiation, and a $\check{C}$erenkov counter used as a veto to select the photons are placed in front of the photon tagger. The calorimeters consist of 49 (ET) and 25 (PT) scintillator crystals (KRS-15) with a length of 20 cm corresponding to 21.5 X_o. The area dimensions are respectively: $15.4x15.4\ cm^2$ for the ET and $10x10\ cm^2$ for the PD. The detectors resolution is $\sigma(E)/E \simeq 0.1/\sqrt{E/GeV} \oplus 0.01$. After acceptance correction the relative error on the integrated luminosity is $\sim 2\%$ [30].

3.3 The trigger system

The most important task of the H1 trigger system is to filter out relevant events for physics analysis and to facilitate the permanent storage of the full detector information. The system must be capable of distinguishing background from physics signals, using the event topology and the timing of the detectors signals. This distinction must be performed as soon as possible to avoid acquisition dead time and the subsequent loss of luminosity produced by HERA for the experiment.
The high frequency bunch crossing of HERA (10.4 MHz) and the luminosity[3] $L \sim 1.5{\cdot}10^{31}$ $\mathrm{cm}^{-2}\mathrm{s}^{-1}$, obtained using high current beams, produces large flow of information related to the interaction of particles within the detectors.
The induced background originating from the interaction of the proton beam[4] with the mechanical part of the machine (beam-wall) and with the residual gas in the beam pipe (beam-gas) can produce event rates of the order of $\sim$ 100 kHz and $\sim$ 1 kHz [31] respectively.
The different kind of physics processes have cross sections varying over several orders of magnitude. This is partially illustrated in fig. 2.2 and summarized in table 3.3 where the cross sections and the expected frequency for different processes are reported. To permit high efficiency in capture of rare processes it is necessary to evaluate as much as possible sub-detector data. The H1 trigger consist of four decision levels[5] see fig. 3.3. The first level, Level-1, performs the first decision to keep the event according to a large number of logical coincidence criteria of different trigger signals; the so called "trigger elements". The Level-1 trigger only produces a "keep" decision (i.e. keep the event) however this decision can be vetoed by a signal coming from the time of flight system or the veto wall. In case of a potentially good event, the decision as to whether to readout the full event or not must be taken before 24 bunch crossings, where the time interval between two consecutive bunch crossings is BC = 96 ns. The full sub-detector information must be therefore stored in memory for at least the time needed for this decision. For this purpose the full data of the different sub-detector is written in a storage pipelines (fig. 3.3) of

process	cross section μb	rate Hz
HERA background		$\approx 10^5$
photo-production	~ 150	$\approx 10^3$
DIS $Q^2 \simeq 2 \cdot 10^3$ GeV^2	$\sim 10^{-2}$	$\approx 10^{-1}$
CC DIS $p_t > 25$ GeV	$\sim 5 \cdot 10^{-5}$	$\approx 10^{-3}$
W production	$\sim 4 \cdot 10^{-7}$	$\approx 10^{-5}$

Table 3.3: *Cross sections and expected rates for different processes estimated for the design luminosity value.*

---

[3] Design value

[4] The electron beam originate synchrotron radiation which is also source of background

[5] During the 1994 luminosity period only Level-1 and Level-4 were used

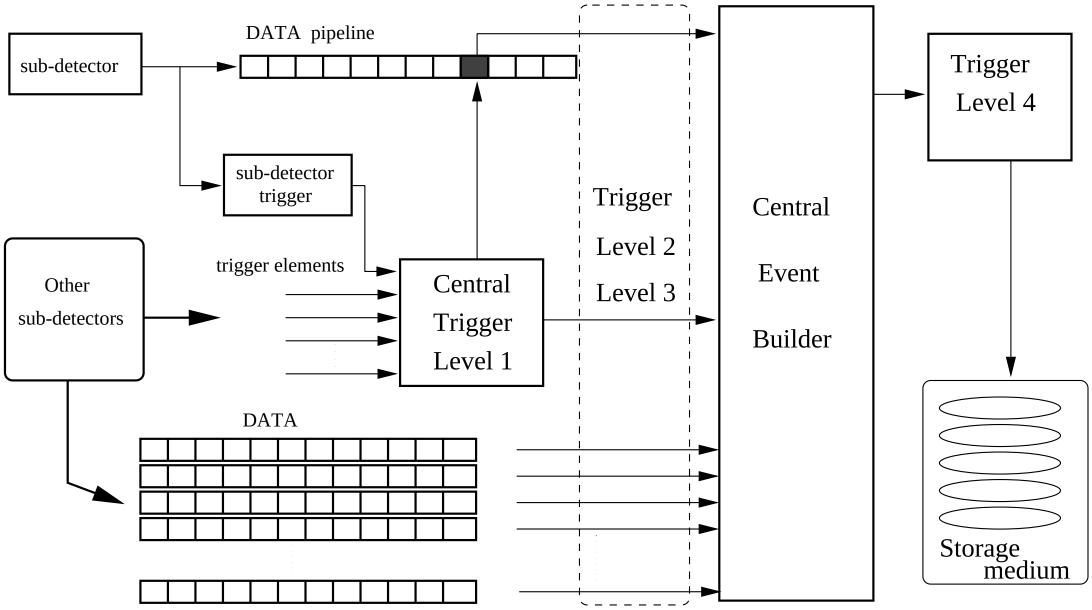

Figure 3.3: *Schematic representation of the H1 trigger system.*

differing lengths according to the sub-detector type. The pipeline lengths varies between 27 and 35 bunch crossings and permits Level-1 to run dead time free. As soon as Level-1 sends the L1-keep signal (to keep the detector data for further evaluation), writing of the data into the pipelines is stopped until the data of each sub-system are transferred to the central event builder.

During this time (i.e. 1-2 ms) all events occurring in H1 are invisible to the Data Acquisition, because the storage pipelines are frozen and cannot be written with new events. During this time the information can be used by two further trigger systems, Level-2 and Level-3. They can produce the decision to abort the building and read-out of an event after 20 μs and 800 μs respectively. The acquisition phase introduces a dead time which is proportional to the amount of data related to the event. The size of the proton induced background events is very large therefore they contribute largely to the dead time if they are not effectively suppressed at trigger Level-1.

Once all information is collected by the central event builder the event is passed to trigger Level-4. At this level a set of 30 processors running in parallel performs a limited data reconstruction on individual events. Here the full detector information is used and sophisticated software cuts are applied. At this level a rather detailed event classification is performed and the remaining background events are discarded. The events which pass this selection are written permanently at a rate of $\sim$ 10 Hz.

In addition to physics triggered events a further class of events are also accepted: these are internally triggered by random monitor triggers. These events are used mainly for two reasons: the monitoring of the detector response and for the calculation of trigger efficiencies. The rate of random trigger events collected for monitoring is of the order 0.1 Hz.

3.4 Motivation for the very forward calorimeter

In an ideal particle scattering experiment, the measurement of all final state particles is desired. However in a collider experiment such as H1 this is not possible since remnant particles with high momenta, traveling almost parallel to the beam axis, are down the beam-pipe itself and remain undetected.

The primary motivation to instrument the very forward region of H1 with a calorimeter is the desire to extend the acceptance region beyond that of the liquid argon calorimeter to $\theta < 3.5^{\circ}$ with respect to the proton direction. The use of a compact calorimeter with high granularity placed around the beam pipe enables the measurement of energies and positions of charged and neutral particles scattered at very small angles θ .

The importance of these measurements is emphasized by the momentum asymmetry of the electron and proton beams of the HERA machine: the electron-proton center of mass moves in the laboratory system with a momentum of $\approx 790\ GeV/c$ along the proton direction. Hence large energy flows are expected and indeed observed in the forward region of the H1 detector.

In essence a calorimeter is a block of matter in which particles interact and deposit their energy. The calorimeter part, where the deposited energy is transformed into a measurable quantity, is usually indicated as active material. The produced signal is in general of electrical or of optical nature and is proportional to the deposited energy.

In sampling calorimetry only a fraction of the material building the calorimeter is active. Sampling calorimetry with high granularity represents one of the most successful techniques to measure simultanuosly the energy and the position of hadrons and electrons over an energy range from several to 100-1000 GeV [32, 33]. The expected particle spectrum close to the proton beam at HERA lies within this energy range and therefore calorimetry appears to be a well suited technique to perform the measurements.

The measurement of the hadronic final states in the region around the proton remnant using a sampling calorimeter close to the beam pipe is a matter of interest in several fields of the HERA-project research as illustrated by the following points:

- In deep inelastic electron-proton scattering (DIS) events, the proton deprived of one or more constituents does not behave in most cases as a bounded state [6]. Part of the so-called proton remnant can have a relatively large transverse momentum due to the color interaction between partons and can be detected using a calorimeter close to the beam pipe. This measurement provides information on the partons inside the proton.

- Events in which a very forward jet is emitted can be detected and measured using a forward calorimeter. The measured rate of such events in DIS constitutes an important test for the perturbative-QCD theory [34] for which some predictions are also available [35].

---

[6] This is in general true, however in Large Rapidity Gap events, constituting 6-10 % of the DIS sample, the proton remains intact after the interaction.

- In the case of charged current reaction of the type:

  $$e^-(e^+) \ + \ p \longrightarrow \overline{\nu}(\nu) \ + \ X \tag{3.1}$$

  where the scattered lepton is a neutrino, the calculation of the kinematic variables y , Q^2 and x can only be obtained using information given by the outgoing hadronic system X. Using the method introduced by Blondel and Jacquet [36] the kinematic variables are calculated using the measurable final state X in the detector, and the known quantities such as the center of mass energy $\sqrt{s}$ and the energy of the electron E_e in the initial state. Thus the resolution of the kinematic variables improves with increase in the number of particles of X that are measured within the detector.

- Important uses of the forward calorimeter are the selection of Large Rapidity Gap events [8], the rejection of experimental backgrounds and to aid in the analysis in the search for super symmetric particles [38]. In all of these applications the forward calorimeter information is used in conjunction with data from other detectors.

Thus the instrumentation of the low θ region of H1 with a calorimeter is qualitatively well motivated in different important fields of research at HERA.

Chapter 4

The PLUG-calorimeter in H1

Construction constraints

The cryostat for the liquid argon, in which the main H1 calorimeter is housed, consists of an aluminum double walled tank with a vacuum gap (fig. 4.3). The forward acceptance of the liquid argon calorimeter is, for this reason, limited to $\theta \geq 3.5^o$. Within this detector configuration no free space for a forward calorimeter is available between the cryostat and the beam-pipe.
The only place suited for a forward calorimeter, capable of closing the gap in acceptance caused by the cryostat, is the $\sim$ 35 cm radius hole in the middle of the forward end-cap of the iron yoke. Due to the geometric constraints the maximum longitudinal dimension that the PLUG calorimeter can have, is $\sim$ 68 cm. Beyond the limitation on the dimensions connected to this location other strong constraints related to the magnetic field in this region must also be considered. The presence of the highly inhomogeneous magnetic field of the order of 1 Tesla generated by the H1 solenoid, affects the choice of the readout technique. In fact the use of scintillators with photo-multipliers would require here particular care in order to maintain gain and noise under control. Furthermore it is prohibited to use ferromagnetic material near the beam pipe as absorber material, as its presence would disturb the magnetic focusing of the electron beam thereby hampering the attainment of high specific luminosity.

4.1 Selection of readout and sampling technique

The decision to build a sampling calorimeter in the forward region of the H1 detector was constrained by the physical performance required and the feasibility connected with the limited place available. A complete discussion of the properties and advantages of the sampling detection technique and the different technologies to realize such a calorimeter can be found in [32, 39, 41] and the references given therein.

To achieve the most compact design for a sampling calorimeter the use of silicon detectors for the instrumented part is favored. Reasons supporting the choice of silicon as the readout material are as follows: the small thickness of Si-detectors (for ex. ~ 400 μm as used in the PLUG), permits the use of the absorber material in almost the whole available calorimeter length, thus maximizing the shower absorption [42]. In addition it is possible to realize very fast readout electronics by installing this close to the detector itself .

The silicon detectors function at low bias voltage and are insensitive to magnetic fields. They can operate at normal ambient temperature and within normal atmosphere environments. The resultant simplicity of operation of silicon detectors can minimize the detector down-time enhancing the operation efficiency of the calorimeter.

The performances of the silicon detector are very high; a typical value of the signal to noise ratio is $(10:1)$ to minimum ionizing particles (MIP). The charge collection time is of the order of 10 ns and a charge collection efficiency is 100% [47].

The signal calibration is independent of the particle used this enables the possibility to perform absolute calibrations using, for example, α particles from a radioactive source. The signal calibration is constant over the largest range of ionization density and no signal saturation is observable (i.e. the detector response is linear).

The realization of a very compact calorimeter depends firstly on the choice of the absorber material. The parameters which define the shower development in a block of matter, connected with the energy deposition, are the nuclear interaction length λ, in the case of hadronic showers, and the radiation length X_0 for electromagnetic showers. To achieve the highest shower containment within a fixed length, the material chosen as an absorber must have the shortest possible interaction length λ. In table 4.1 some physical properties of atomic elements usually used in the construction of calorimeters are listed [43].

Material	Z	A	ρ [gcm^{-3}]	λ [cm]	X_0 [cm]	λ/X_0
G10	-	-	1.7	53.05	19.4	2.7
Al	13	26.98	2.70	39.4	8.9	4.4
Si	14	28.09	2.33	45.5	9.36	4.9
Fe	26	55.85	7.89	16.72	1.76	9.5
Cu	29	63.55	8.96	**15.06**	1.43	10.9
W	74	183.85	19.3	9.58	0.35	27.3
Pb	82	207.19	11.35	17.09	0.56	30.5
U	92	238.03	18.95	10.5	0.32	32.8

Table 4.1: *Physical properties of the most frequently used absorber materials in the realization of calorimeters*

Considering only the interaction length the most suitable materials are generally those with the highest density ρ and highest atomic mass A. This is because, to first approximation the nuclear interaction length $\lambda \propto 1/(A^{\frac{2}{3}}\rho)$, since the nuclear radius $r \propto A^{\frac{1}{3}}$. In particular tungsten (W) would be the best choice with an interaction length of only $\lambda = 9.58$ cm.

The energy linearity and resolution of a sampling calorimeter depends also on the sampling

frequency of the shower development. In order to obtain the required energy resolution performance $\sigma_e(E)/E \simeq 100\%$ the hadronic shower should be sampled at least every half interaction length. Furthermore, to maintain sensitivity to the electromagnetic shower no more than six radiation lengths should be left without instrumentation [42].
For example a tungsten-based forward calorimeter could be designed for H1 having an absorption depth of $\approx 5\ \lambda$ and ≈ 20 instrumented layers. This calorimeter would fit in the available space, but would be very expensive due to the large number of silicon detectors required for the instrumentation.

An alternative choice of absorber is the use of copper. In this case, because of the ratio of $\lambda/X_0 = 10.9$, the number of instrumented layers can be limited to eight for a total absorption depth of $\simeq 4\ \lambda$. The resulting shower containment is worse than for the tungsten case, but is nevertheless sufficient to absorb, on average, about 85% of the emitted energy. In fact the expected energy spectrum of the particles emitted within the calorimeter acceptance, exceeds 40 GeV only for less than 3% of the cases, as it is shown in fig. 5.5. Thus considering figure 4.1 [32, 33] where the fraction of energy escaping from the calorimeter is plotted as a function of calorimeter depth for different energies of the incident hadrons, follows that $4\ \lambda$ absorbs between 92 and 80% of the energy of particles between 5 and 40 GeV. This confirms the average value of absorbed energy given before. A moderate sensitivity to electromagnetic showers is also achieved. In fact with the first active layers after about $5.5\ X_0$ approximately 50% of the energy of a 10 GeV electron is deposited in the calorimeter and is sampled by at least 2 active layers as shows in figure 4.2 [32].

4.2 Design characteristics

The PLUG calorimeter is housed in the forward end cap of the iron yoke between the liquid argon cryostat and the C3 collimator (fig. 4.3). It consists of two half cylinders each of which are attached to one of the iron yoke shells. Each half cylinder consists of nine copper absorber plates and eight instrumented modules mounted together on a non-magnetic stainless steel frame (fig. 4.4).
The absorbers have a thickness of 6.5 cm and are interleaved by 1.5 cm gaps into which the 1.4 cm thick instrumented modules are inserted. The last absorber, nearest to the C3 collimator, is only ~ 2.5 cm thick and constitutes a shield for the synchrotron radiation. The inserted modules consist of two copper plates of 0.5 cm thickness between which the readout board supporting 42 silicon detectors is contained. The instrumented board is shown in fig. 4.5. The cross sectional view of a module is shown in fig. 4.6. The figure shows also a Si-detector glued on its ceramic support with the contact pin soldered on a readout board. The resulting sampling structure of the calorimeter consists therefore mainly of 7.5 cm copper and 400 μm of silicon.
In the original design the first active layer was placed behind the first copper-absorber. This was subsequently changed by locating the first detector layer in front of the first absorber in order to minimize the effect of the intervening inactive material between

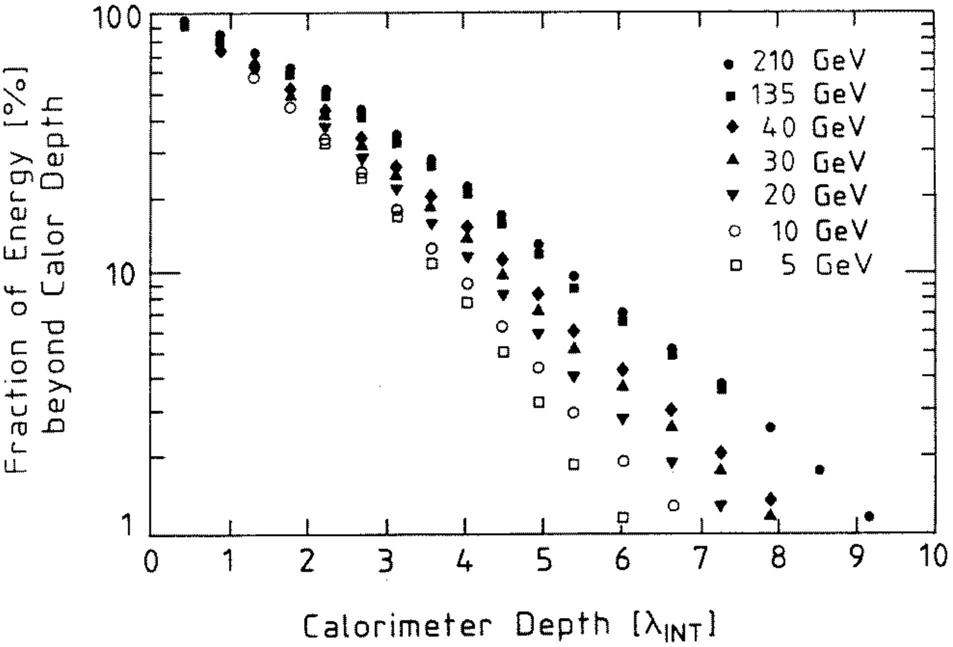

Figure 4.1: *Hadronic shower development: energy fraction of incident hadrons beyond the calorimeter as a function of the interaction length lambda* λ

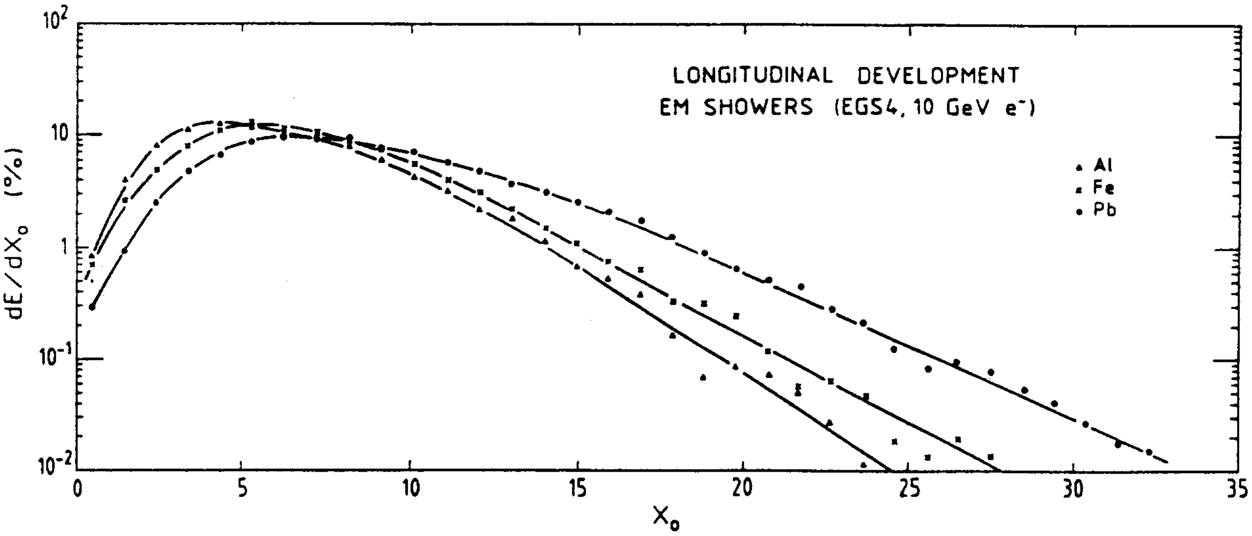

Figure 4.2: *Electromagnetic shower development for 10 GeV electrons: specific deposited energy as a function of the radiation length* X_0

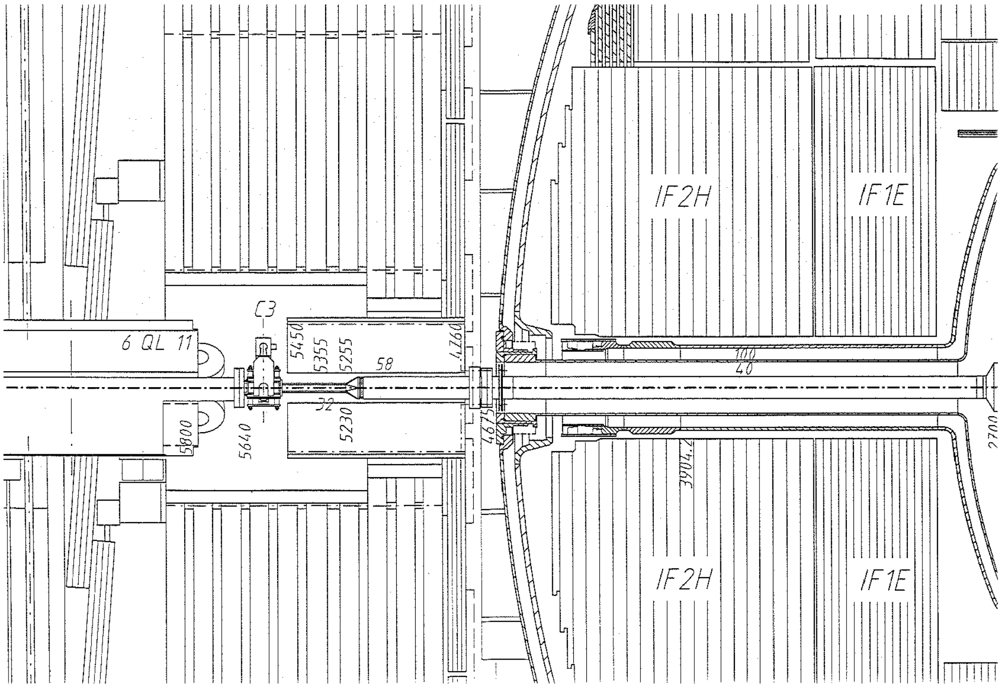

Figure 4.3: *Section of the forward part of H1 detector; the PLUG calorimeter is visible in the middle of the figure near the C3 collimator. The double walled cryostat and the inner forward modules (IF2H, IF1E) of the LAr are illustrated on the right part of the figure.*

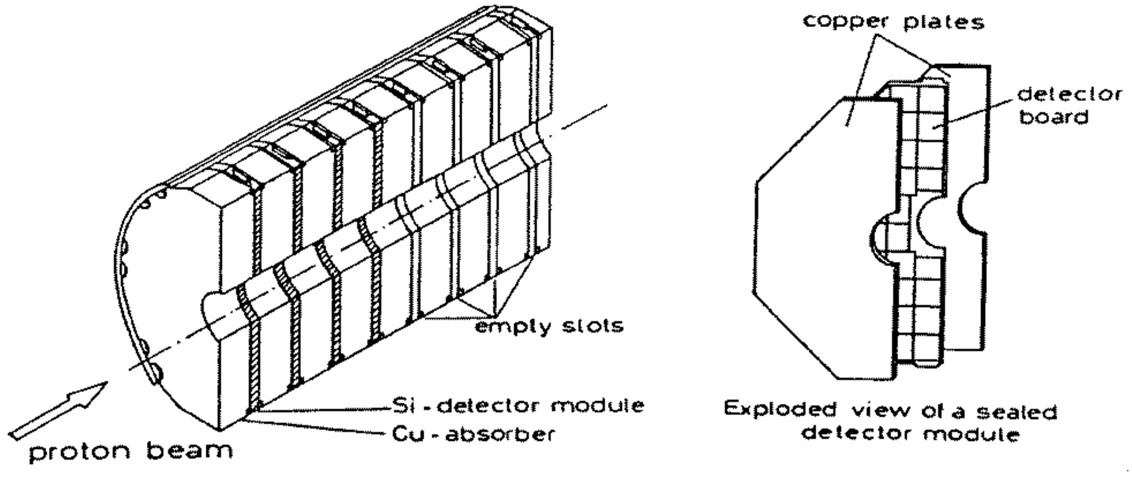

Figure 4.4: *Half-PLUG structure and module view*

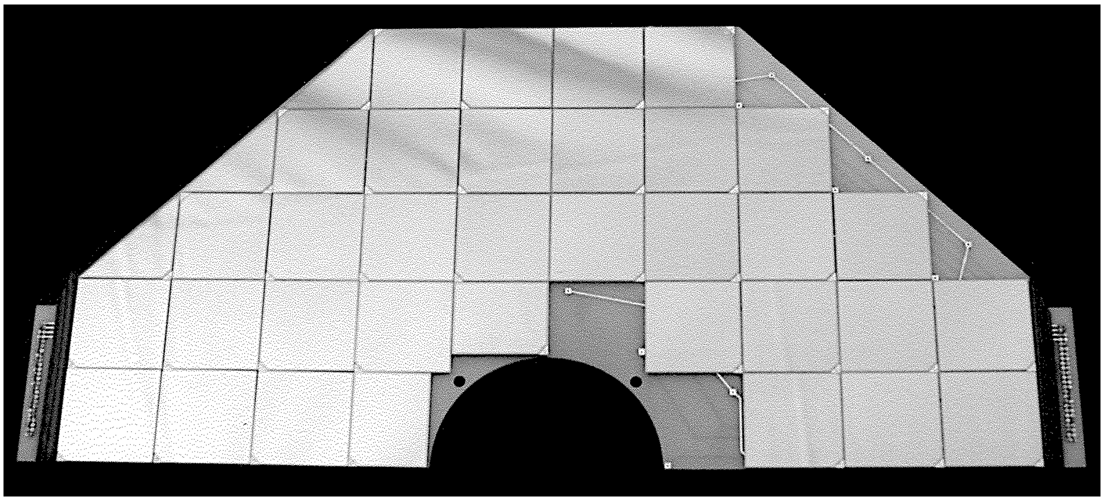

Figure 4.5: *Readout board with Si-detectors. This board is contained within two copper slabs each 5 mm thick and constitute a PLUG detector module.*

the PLUG and the interaction region[1]. This inactive material works, in this case, like an absorber of the sampling calorimeter. The quantitative consequences of the inactive material on the energy measurement are discussed in the next chapter.
The major characteristics of the PLUG are given in table 4.2 The granularity of the calorimeter is determined by the silicon diode dimensions (5×5 cm^2), giving an obtainable angular resolution $\sigma_\theta \simeq 10$ mrad. The longitudinal read out segmentation is in four sections so that for eight instrumented layers the signals of two detectors with same the x-y coordinate in two consecutive layers are summed into one electronic signal channel. The typical volume of a calorimeter cell is therefore $5 \times 5 \times 16$ cm^3.
However, during the luminosity run periods 1995 and 1996 the instrumentation of the PLUG was limited to four detector layers. In this PLUG configuration, each readout channel corresponds directly to only one single Si-diode rather than two. This option was mainly motivated by an enhancement of operational efficiency and improved monitoring of the channel response. The improvements due to the one to one detector to channel mapping.

4.3 Silicon diodes

The silicon detectors used in the PLUG calorimeter are metal-semiconductor surface barrier diodes (see fig. 4.7). They are fabricated using ~400 μm thick n-type silicon wafer

---

[1] The amount of inactive material in the forward region of the LAr cryostat was increased with respect to the original design in order to provide more mechanical stability to the cryostat

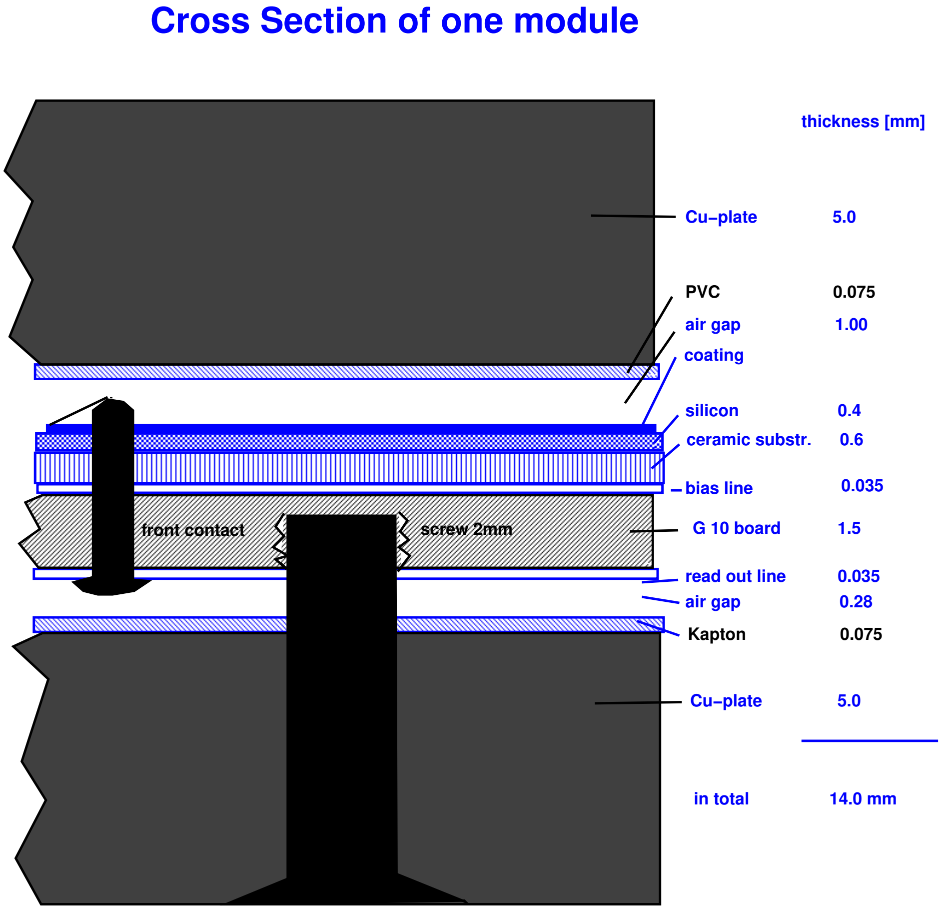

Figure 4.6: *Detail of the module cross section with material thickness*

substrates having high resistivity (≈ 5 kΩ cm) [47]. The gold and aluminum metal coatings are in contact with the silicon for more than 96% of the detector area and in the border regions they overlay an insulating silicon-oxide region forming a metal-oxide-silicon, or MOS, structure. For polarity reasons the gold-side MOS is responsible for the steep decrease of the detector capacitance with increase of the bias voltage when $V_{bias} \simeq V_{fb}$ where V_{fb} is the flat band voltage [48]. This is clearly shown in figure 4.8. When the bias voltage $V_{bias} > V_{fb}$ the diode capacitance vs. voltage C(V) curve no longer depends on the MOS structure.
With increasing reverse bias voltage the electric field extends into the depth of the silicon, finally reaching the rear electrode at the so called depletion voltage V_{dep}. For any operating voltage $V \leq V_{dep}$ the diode works essentially as a solid-state ionization chamber in which the active thickness corresponds to the detector thickness.
When ionizing particles penetrate the silicon lattice, electron-hole pairs are *produced*. The charges drift in the presence of the electric field and are collected by the detector electrodes to give rise to an electric signal proportional to the deposited energy (see fig. 4.7). The energy amount absorbed to produce an electron-hole pair in the silicon is 3.6 eV.

weight	1480 kg
radial dimensions (overall) (instrumented part)	 6 cm $\leq$ r $\leq$ 30 cm 6 cm $\leq$ r $\leq$ 26.5 cm
longitudinal dimensions (overall) (instrumented part)	 475 cm $\leq$ z $\leq$ 542 cm 475 cm $\leq$ z $\leq$ 539 cm
instrumented length	64 cm $\simeq$ 4 λ
instrumented height	20.5 cm $\simeq$ 1.4 λ
angular range instrumented range	$0.6^o \leq \theta \leq 3.5^o$ $0.65^o \leq \theta \leq 3.2^o$
number of layers × layer length	8 × 8 cm
layer structure	6.5 cm Cu absorber + 1.4 cm module (see fig.4.6)
shower scales in Cu	1 λ = 15.06 cm, 1 X_0 = 1.44 cm
Si-detector dimension	25 ; 20 and 12.5 cm^2
number of detectors in 1 layer	2 × 42 = 84
total number of detectors	672
number of electronic channels	336

Table 4.2: *Design Parameters of the PLUG Calorimeter*

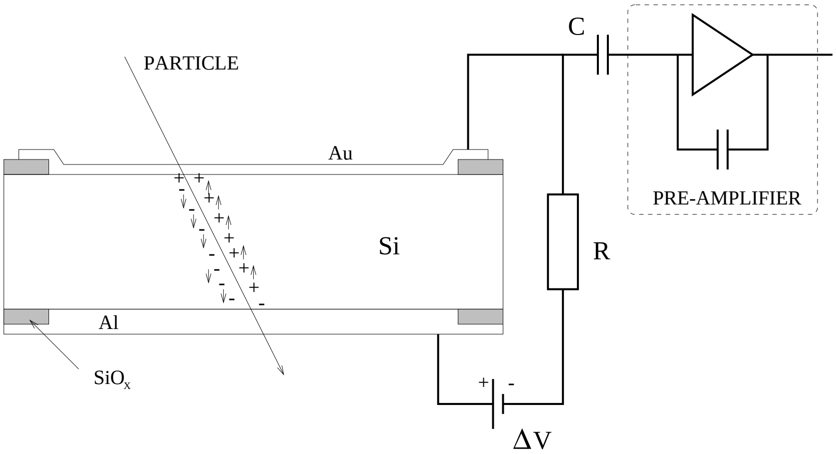

Figure 4.7: *A single PLUG silicon diode*

This quantity is about one order of magnitude lower than the energy absorbed in the production of an electron-ion pair in a gas. It follows that the number of charged carriers and also the signal pulse height per unit of absorbed energy of ionizing particles is much larger than for gas or scintillator detectors and furthermore it is independent, to on the kind of particles and their energies [50]. For these reasons a particle and energy indepen-

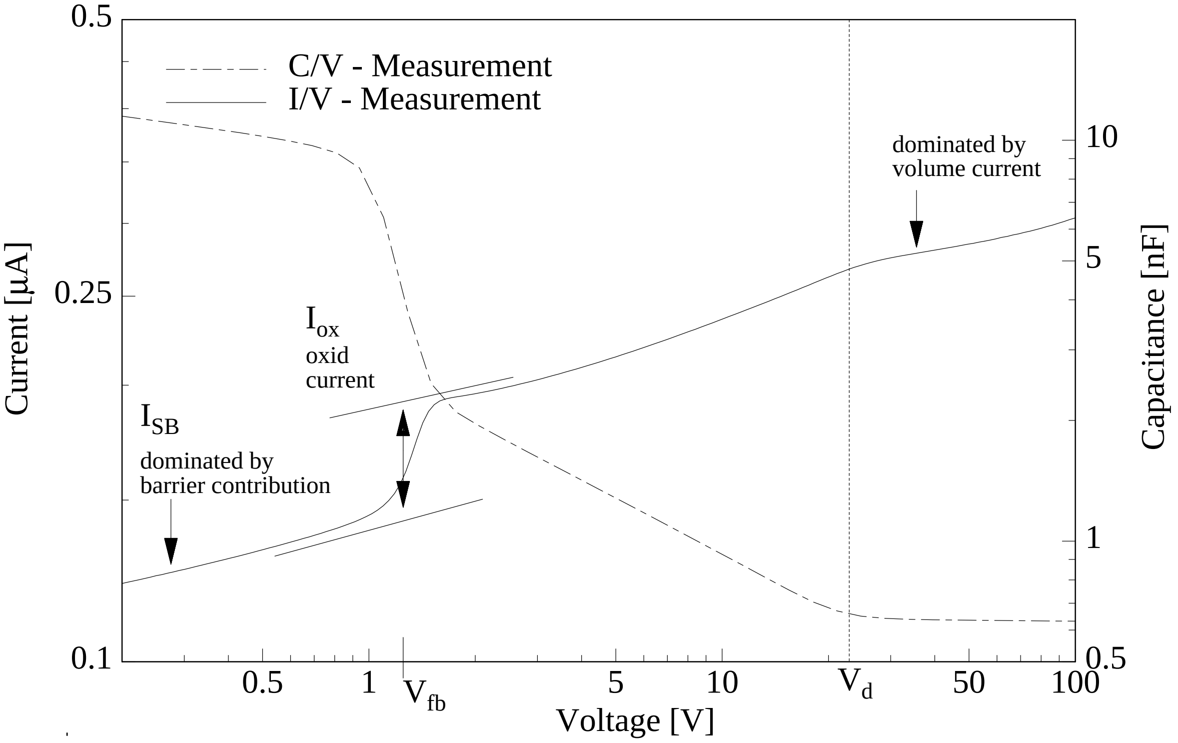

Figure 4.8: *Silicon diode current and capacitance vs. voltage characteristics*

dent calibration of the silicon detectors can be achieved.

The relationship between applied voltage V and the active thickness of the detector is calculable; by assuming the specific resistivity of the silicon wafer as a constant, the following results are obtained:

$$\begin{aligned} x(V) &= d \cdot \sqrt{\frac{V+V_b}{V_{dep}+V_b}} \qquad &for \qquad &V \leq V_{dep} \\ x(V) &= d &for \qquad &V > V_{dep} \end{aligned} \tag{4.1}$$

Where $V_{dep} \approx 50\ V$ is the depletion voltage and $V_b \simeq 0.5\ V$ is the potential due to the metal-silicon contact (Shottky). Using these relationships it is possible, when the applied voltage is known, to calculate the depletion level of the detector and therefore calibration factors can be calculated even for bias voltages $V \leq V_{dep}$. The relationship between the relative variation of the active thickness of the diode and the relative variation of the bias voltage is:

$$\frac{\Delta x}{x} \simeq \frac{1}{2} \cdot \frac{\Delta V}{V} \tag{4.2}$$

where V_b has been neglected, because $V_b \ll V$.

The response of the PLUG detectors $R(V, E_0)$ to particles at fixed energy E_0 and as a function of V was investigated on a test beam experiment at ITEP[2] [49]. It was shown

---

[2] Institute for Theoretical and Experimental Physics, Moscow

that using 5 GeV pions and for different bias voltage values with $V \geq V_{dep}$, the detector response $R(V, E_0)$ is constant within less that 1% variation. This implies that the calibration for a fully depleted detector is independent of the applied voltage.
The charge collection efficiency for the PLUG Si-diodes was also studied in detail to verify the calibration stability even after irradiation with 25 MeV protons at a fluence of 10^{12} p/cm^2. The results reported in [47] confirm the 100% charge collection efficiency for non-irradiated detectors and a variation of 0.6% after the fore mentioned irradiation.
Several physical properties of a Si-detector can be studied using the characteristic curves of the diode. It is worthwhile to consider the capacitance and the current as a function of the voltage. These functions are both shown in figure 4.8 for one PLUG diode having a depletion voltage of $\sim$ 25 V.
From the capacitance-voltage curve (C(V) function) it is possible to measure the depletion voltage (V_{dep}) necessary for the optimal operation of the detector [44]. When the voltage is increased the depleted silicon volume between the electrodes increases and the capacitance of the detector decreases until the silicon volume is completely depleted.
The current-voltage curve (I(V) function) can be described as a sum of three current contributions: barrier, oxide and volume. An important property of the current curve is that for voltage values larger than V_{fb} (see fig. 4.8) the current I(V) depends on the volume current which in turn is correlated to the number of charge generation centers in the silicon. A change of the volume current is usually an indication of bulk damage of the silicon due to hadronic radiation.
A slow increase of the detector reverse current has been observed during the 1994 luminosity period (see fig. 4.9), which is possibly the result of bulk damage [48]. However the

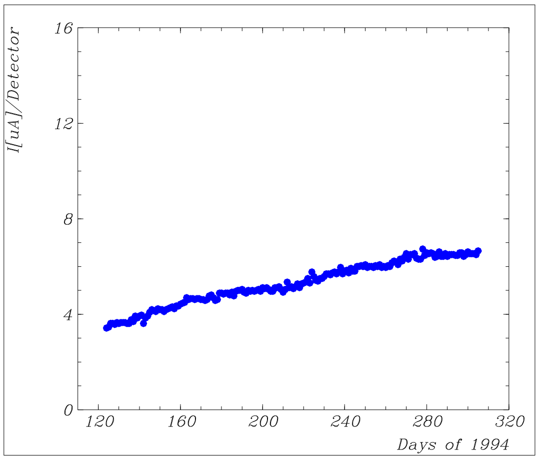

Figure 4.9: *Example of detector current evolution as a function of the day of 1994 is shown. The bias voltage applied to the detector was constant over the period.*

atmospheric condition of the PLUG environment other reasons such as humidity or ozone formation affecting the detector surfaces could not be excluded.

4.4 The readout system

The readout electronic for the PLUG calorimeter is in large part the same as that used for the liquid argon calorimeter. A detailed description of the single components can be found in [52, 53, 54, 55].
To illustrate the most relevant components of the PLUG acquisition chain and the connections between these components, a block diagram is shown in figure 4.10. The signals produced by the 672 Si-diodes of the fully instrumented calorimeter are merged, as explained previously in section 4.2, into 336 channels in four adapter-boxes (ADBX) each one of which is attached to one analogue-box (ANBX). The adapter-box consists of passive components and of an 8-fold multi-layer board (see fig. 4.11) where signals from the detectors, pulses from calibration pulsers and the bias channels from the voltage supplies are connected and redistributed.

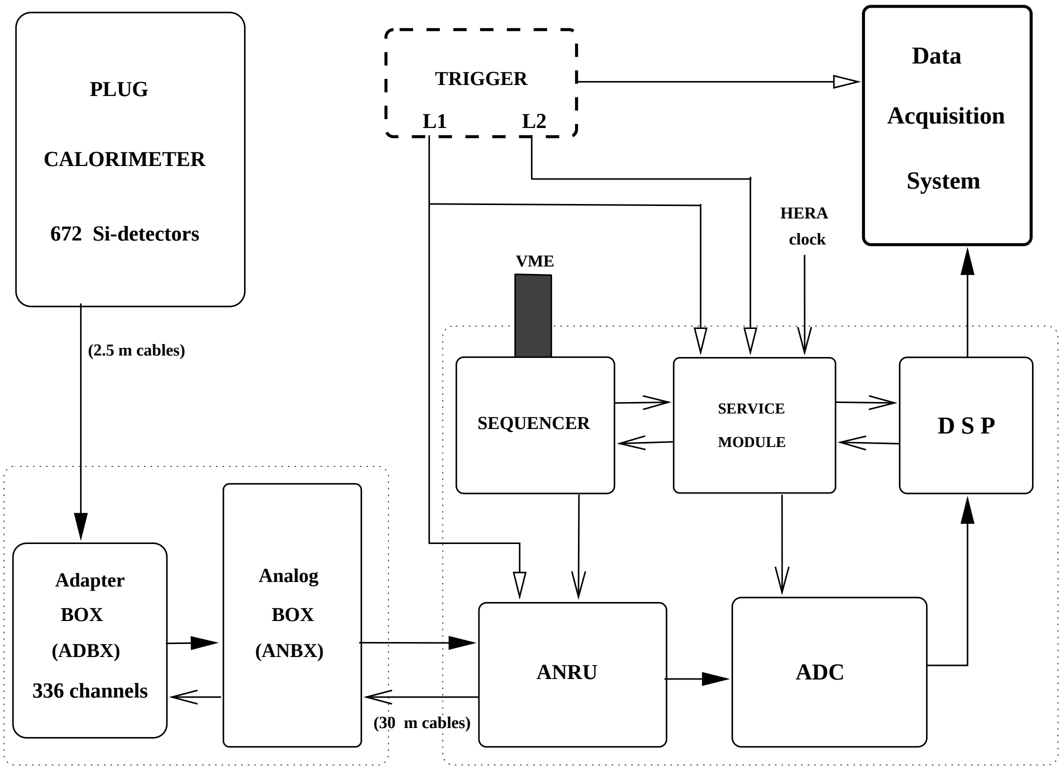

Figure 4.10: *Acquisition system of the H1-PLUG calorimeter*

One adapter-box enables the connection of 1/4 of the PLUG detectors (PLUG-quadrant) to one analogue-box which contains the analogue electronics for the amplification and shaping of the signals. The maximum value of the signal pulse height is registered and stored by a sample & hold circuit. Subsequently when the signals of all channels are present, they are multiplexed outside of the analogue-box to the analogue receiving units (ANRU) placed in the H1 electronics trailer.
The signals are then digitized by the Analogue to Digital Converter (ADC) unit and

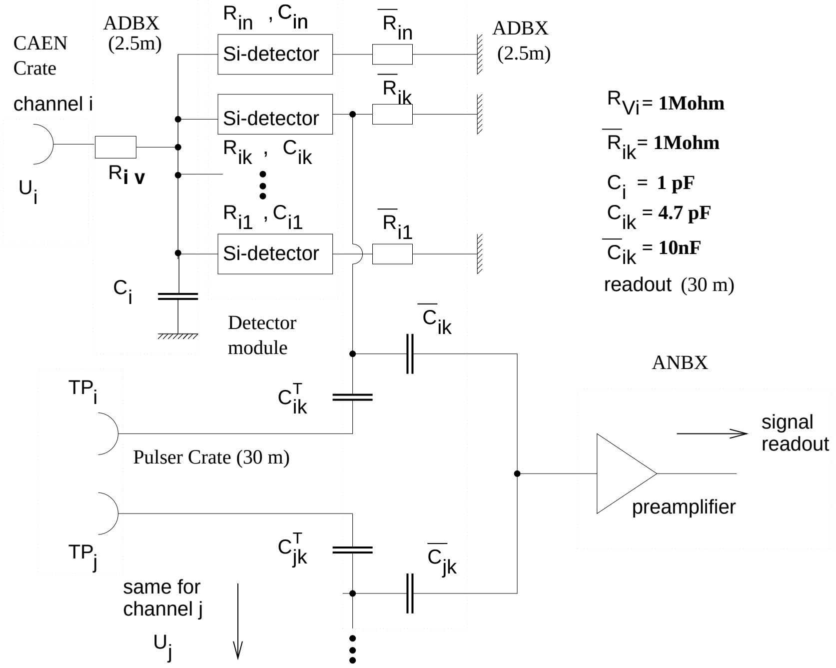

Figure 4.11: *Some details of the electronics of one PLUG adapter-box (ADBX). Si-detectors and pre-amplifier in the analogue-box, are also shown*

processed by the Data Signal Processor (DSP) using additional information such as the calibration constants for individual channels.
The calibration system, also placed in the H1 electronic trailer, consists of 32 pulse generators. They are driven by an OS9 computer system using a H1 software calibration program capable of providing several calibration options; operative details of which can be found in [56]. The pulse generators provide sharp rising ($\tau \simeq 5$ ns) pulses with programmable amplitudes in the range 0 - 1.03 V . The pulsers can inject charge into the inputs of the pre-amplifiers via individual charge terminators. By recording the ADC responses related to different pulse amplitude it is possible to perform the charge calibration of each electronics channel of the PLUG over the full dynamic range of the ADC. Details on the absolute calibration procedure will be given in ch. 5.2. The day by day calibration of the electronics provide also a constant inter calibration between the channels.

The bias voltage for the Si-detectors of the PLUG is provided by two CAEN supplier systems (mod. SY127) giving a total of 80 independent voltage channels. The voltage supply of the 42 detectors of a calorimeter module is provided using eight separate voltage lines as visible in fig. 4.12 (quarter of ring). As shown on fig. 4.12 3, 5, 6 and 7 detectors are connected in parallel to each bias channel. The detectors belonging to one bias channel have been sorted to have similar depletion voltages in order to avoid the application of bias voltage 10 to 20% higher than the depletion voltages. In total 128 voltage lines are present for the fully instrumented PLUG. In order to limit the number of bias channels to 80, the two outer voltage lines of each module are merged into one bias channel. With this configuration up to 14 detectors are connected to one bias channel [3]. The choice to merge the supply of outer detectors is because they are less subject to current increase due to radiation damage; the responsible hadronic flux being much stronger at smaller radii [51].

Radiation damage and current trips of the bias supplies because of machine accidents such as an accidental or incomplete beam dump, or bad beam background conditions can produce noisy calorimeter channels.

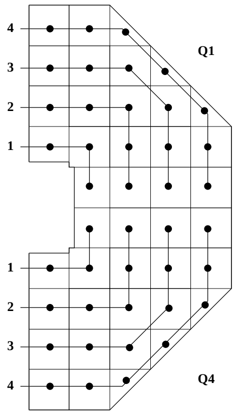

Figure 4.12: *Voltage supply scheme of one PLUG module*

In the next sections two procedures to suppress and investigate the noisy channels of the calorimeter are presented. The first is related to automatic monitoring of individual calorimeter channels and the second is based on the off-line analysis both based on artificial random trigger (random trigger) events.

4.5 Data reconstruction

With the data reconstruction procedure the information produced by the electronics of the H1 detectors is transformed into physics information as used in the event analysis.

The information flow starts at the detector level. The charge pulses due to ionization are amplified and subsequently digitized by an ADC. The digital signals from individual channels are than transformed with a digital signal processor which equalizes the different channel gains, subtracts pedestals and uses programmable thresholds to reduce the volume of data (see fig. 4.13).

The data reduction depends on the applied threshold which usually is $2\sigma_i$ of the pedestal distribution of the channel i. With this choice the expected number of channels which have randomly a signal beyond the threshold is 5% of the total number of channels.

The PLUG-raw data produced from the DSP consists of address (code) and the detected

---

[3] In the 95 configuration this was no longer necessary, because of the reduced instrumentation of the calorimeter previously discussed

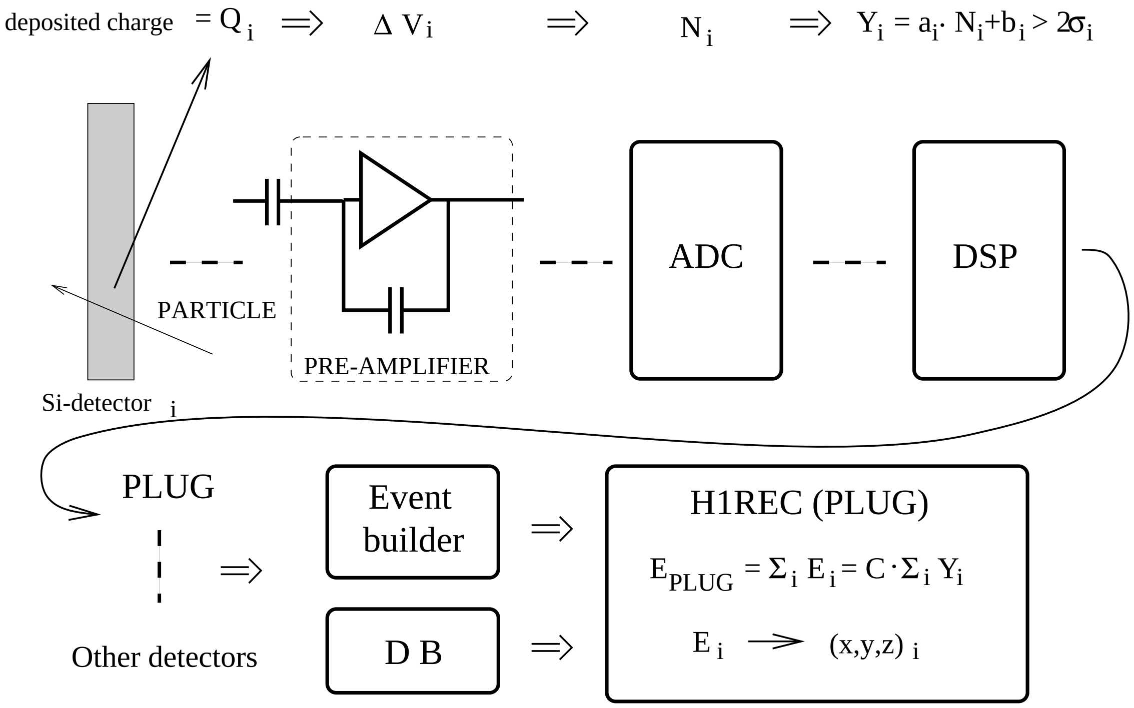

Figure 4.13: *Simplified scheme of the data transformation from the detector signal (Q_i) to reconstructed data. After the analogue to digital conversion the signal is processed by the DSP. It performs a linear transformation of the signal of each channel. This corresponds to the gain equalization for each of the 336 channel and the pedestal subtraction. The reconstruction program performs further operations and rescales the signals of deposited energy in GeV units taking into account the calorimeter sampling fraction.*

energy for each calorimeter channel above the specified threshold. The event builder merges the data made available by each H1 sub-component and produces the H1-raw data [57].
Further information necessary for the PLUG data reconstruction is produced by the PLUG monitor program (see ch. 4.6). This information is stored in the H1 data base (DB). The monitor program (PLMONI) runs in parallel to the data taking and produces online information on the signal behavior of each channel randomly triggered. The main input for the reconstruction program are the data written by the event builder program.
The data reconstruction procedure requires the signal of each of the calorimeter channel present and its identification address. The digitized signals, which represent the energy deposition in the calorimeter cells, are converted in to deposited energy expressed in GeV taking into account the calibration constant. The composition of the calibration constant is discussed later in section 5.2. To the address identifying the electronic channel is associated the coordinate of the calorimeter cell expressed in centimeters in the H1 laboratory frame. By combining this information it is possible to associate each calorimeter cell with a 4-vector used later in the event analysis. For example the components of the momentum

4-vector associated to the particles hitting the i-cell are as follows:

$$\mathbf{P_i} \equiv (E^i/c, P^i_x, P^i_y, P^i_z)$$

$$P^i_x = E_i \cdot \frac{x_i}{R}; \qquad P^i_y = E_i \cdot \frac{y_i}{R}; \qquad P^i_z = E_i \cdot \frac{z_i}{R}$$

where it has been assumed a primary particle with negligible mass originated from the nominal vertex position (R is the distance between the cell i and the nominal vertex position). The data reconstruction is performed by the H1 reconstruction program [4]. This program is as far as possible modularly constructed, so that each H1 sub-detector is represented by one or more independent software *modules*. For the PLUG two modules exist: the PLUG-scale (PSCALE) and the PLUG-cluster (PCLUST), called in sequence by the main program. The first module performs the corrections [5] and data rescaling while the second orders data within a cluster structure used to combine PLUG information with the information of the other H1 calorimeters (for detail see [58]).

The reconstruction makes use of all accessible information of the calorimeter data and of the absolute energy calibration described in ch. 5.2. The information is stored in the form of BOS [59] banks in the raw data and in the H1 DB. The following information is used during the reconstruction [60]:

- channel signals, channel addresses (raw data)
- calorimeter configuration, geometrical channel mapping, thickness of each Si-detectors (DB)
- calibration constants and noise of calorimeter channels (DB)
- channels monitoring results (PLUG monitor program → DB)
- user steering cards for noise cuts and *hot channel* suppression (DB)

The PLUG reconstruction procedure consists of two parts, one for the run start and one for the event processing. In the run start procedure, all run-dependent information is acquired once. The run-dependent information is all but the event information (i.e. channel signals and related addresses). In the second part each event belonging to the run is processed. During the event processing the handling of the raw-data and the scaling into calibrated energy by looping over all channels of the calorimeter is performed. In the channel loop the following cuts and eventual corrections are accomplished:

1. noise cut for channels with a signal below 3σ of the pedestal distribution, in order to further reduce the data volume
2. *hot channel* suppression according to criteria specified in the next section

---

[4] H1REC: standard program of the H1 Collaboration for the data reconstruction

[5] As for example the noise suppression

3. correction for non-fully depleted channels, if necessary (bias correction: see section 4.3)
4. energy conversion into GeV units and assignment of H1-coordinates to the channels.

The final results consist of the cell calibrated energy and position of the calorimeter cell in the H1 coordinate system. For every H1-run the reconstruction program produces a set of distributions and plots, the L5 histograms, which permit a fast check of the calorimeter performance and of the reconstruction procedure (see [60]).

4.6 Analysis of the random trigger events

Online - the PLUG-monitor program

The function of the PLUG-monitor program is to collect run by run information about the stability and noise of each PLUG channel. This information is then stored in the H1 Data Base as BOS banks and is used to exclude badly behaving channels during the data reconstruction.

A channel which shows sizeable variation in performance (in the sense specified later), during the operation time is indicated here as a *hot channel*.

To test each individual channel, the program uses the latest calibration parameters and the random trigger events present in the raw-data. The algorithm used by the monitor program works as follows: the program collects up to 3000 random trigger events and produces the signal distribution of each channel. In the ideal case without beam induced background, coherent noise etc. the pulse height distribution of one channel is the noise distribution around the pedestal value (pedestal distribution). Because of the on-line zero suppression for the data reduction, the recorded events populate the regions of the distribution with an absolute value larger than $2\sigma_i$ of the noise (or pedestal) distribution of the channel i (see fig. 4.14). By comparing this distribution with the pedestal distribution produced during the calibration (produced $\sim$ at least once a week without beams) it is simple to determine quantitative differences and thus to identify " *hot channel*" candidates.

In practice, during data taking the particle beams can produce further signal pile-up and noise so that differences between the quoted distributions may be always present.

The semi-empirically developed criteria to recognize *hot channels* is to set a label, consisting of a single bit, to one channel when the signal exceeds 4σ of the calibration noise in more than 10% of the random trigger events. The candidate channels are then excluded during data reconstruction.

The validity of this criteria is demonstrated by figure 4.15 where the channel maps of the random trigger events for an individual acquisition run before and after the *hot channel* suppression are shown. Although the situation during the 1994 luminosity run was not optimal and had improved considerably ever since, the *hot channel* suppression lead to an exclusion of about 10% of all channels. In fig. 4.15 (a) there are about 20 channels producing many more hits than expected. These channels also fulfill the exclusion the criteria to recognize the *hot channel* based on the channel signal and are filtered out as shown in fig. 4.15 (b).

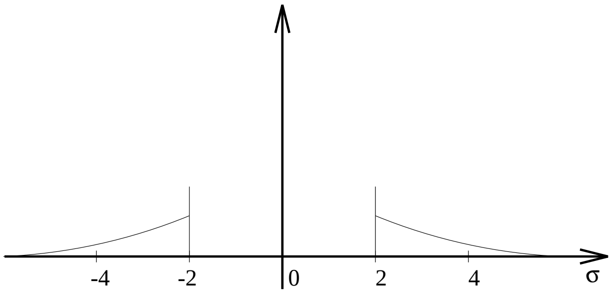

Figure 4.14: *Schematic representation of the noise distribution after the 'zero suppression'.*

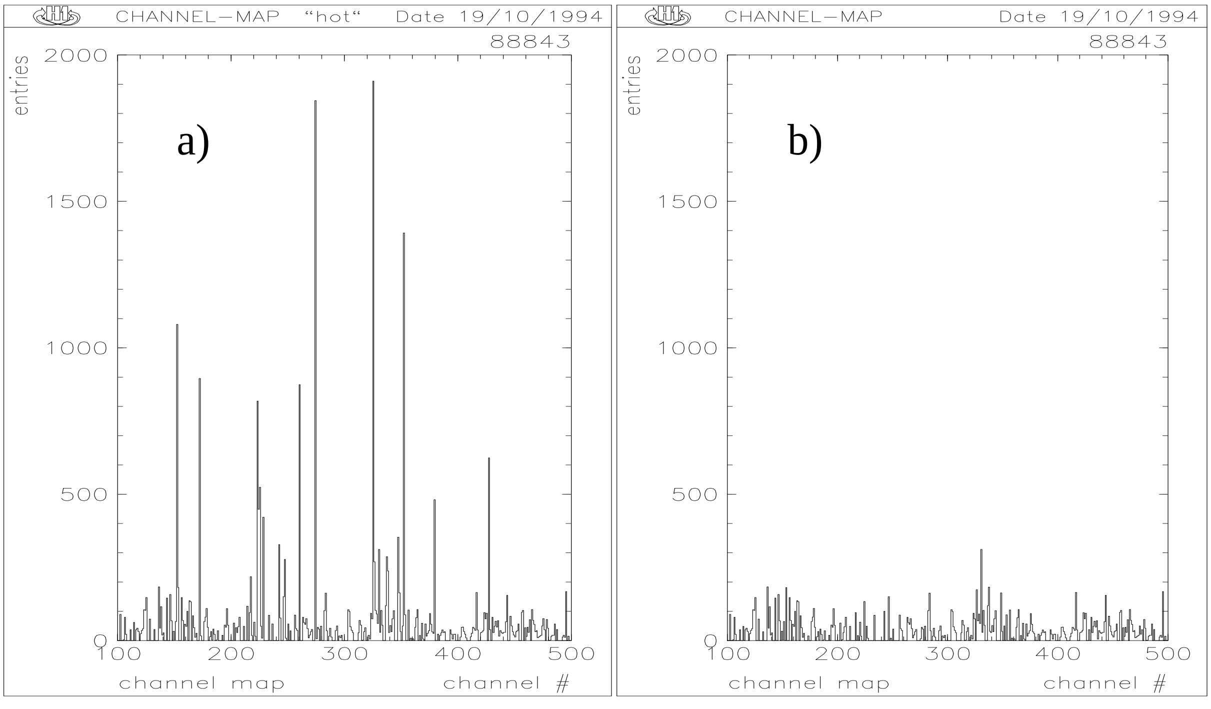

Figure 4.15: *(a) PLUG channel maps before and (b) after hot channels suppression. The entries are the numbers of random trigger events for which a channel gives a signal above $2\ \sigma_i$. The total number of random trigger events in these plot was 3000.*

Off-line

In addition to the online monitoring with *hot channel* suppression, it was necessary during the luminosity run period of 1994 to verify the behavior of the PLUG data and their reliability. To accomplish this task, events selected using random triggers have been analyzed.

These data cover the whole period of positron running. The integrated luminosity for this period was about 3.5 $pbarn^{-1}$ distributed over 1807 H1-runs for the physics analysis.

To monitor the PLUG performance over all runs, the average PLUG event energy per run $< E_{PLUG} >$ and the average cell multiplicity per run $< N_{cells} >$ have been considered. The plots of these variables vs. run number are illustrated on the left-hand side of fig. 4.16 . The plots reveal the existence of runs with unexpectedly high values of average energy and multiplicity. The mean energy reaches 50 GeV and a mean cell multiplicity of 35. These large values are a clear indication of problems affecting the calorimeter during these runs. In the right-hand side of figure 4.16 the distributions of these variables are shown. The shaded overlayed distributions are obtained by applying the following cuts: The values are obtained by considering fits of the two distribution as shown in fig. 4.17.

$$\langle E_{PLUG} \rangle \; < \; 8\, GeV \qquad and \qquad \langle N_{cells} \rangle \; < \; 8 \tag{4.3}$$

The fit using two Gaussians is justified by the assumption that at least two beam-background regimes existed during the luminosity period 1994 . In other words the runs belong to two different Gaussian distributions with very similar means (in fig. 4.17 P2 and P5 are equal within the errors). The first describes the bulk of the runs and the second broader distribution describes runs where the PLUG mean response fluctuates more because of larger beam background and signal pile-up. Using the criteria in (4.3) only 3% of the 1807 considered runs are excluded from the analysis performed later in this work and good PLUG data quality is thereby ensured. The exclusion of these runs is equivalent to a loss of about 100 nbarn^{-1} of data and is a negligible loss for the measurements presented later.

The distributions of the total energy in the PLUG, the total cell multiplicity and the energy spectrum of the calorimeter cells are shown in figure 4.18. Each of these distributions is shown using two samples. One including all runs and the other excluding runs according to the conditions (4.3). The distributions, obtained including all runs, present a second maximum which has no physical meaning. This suggest the existence of problems affecting the acquisition electronics or the detectors themselves. The distributions obtained using the second sample do not show the second maximum.

Looking at the PLUG channel maps it is for example possible to identify the exact location of the noisy channels. Figure 4.19 shows the spatial channel map of the calorimeter cells for the four PLUG layers. The first layer is the nearest to the interaction point and the coordinates x and y refer to the H1 coordinate frame. The box dimensions in the plots are proportional to the deposited energy in the calorimeter cell. The non homogeneous distribution of the pulse height gives evidence for channels affected by problems.

That current trips of the bias supply are the cause of the high noise is very improbable, because the affected channels belong to at least 11 different bias voltage channels. The suspicious channels are present in every PLUG layer and all of them are connected to one

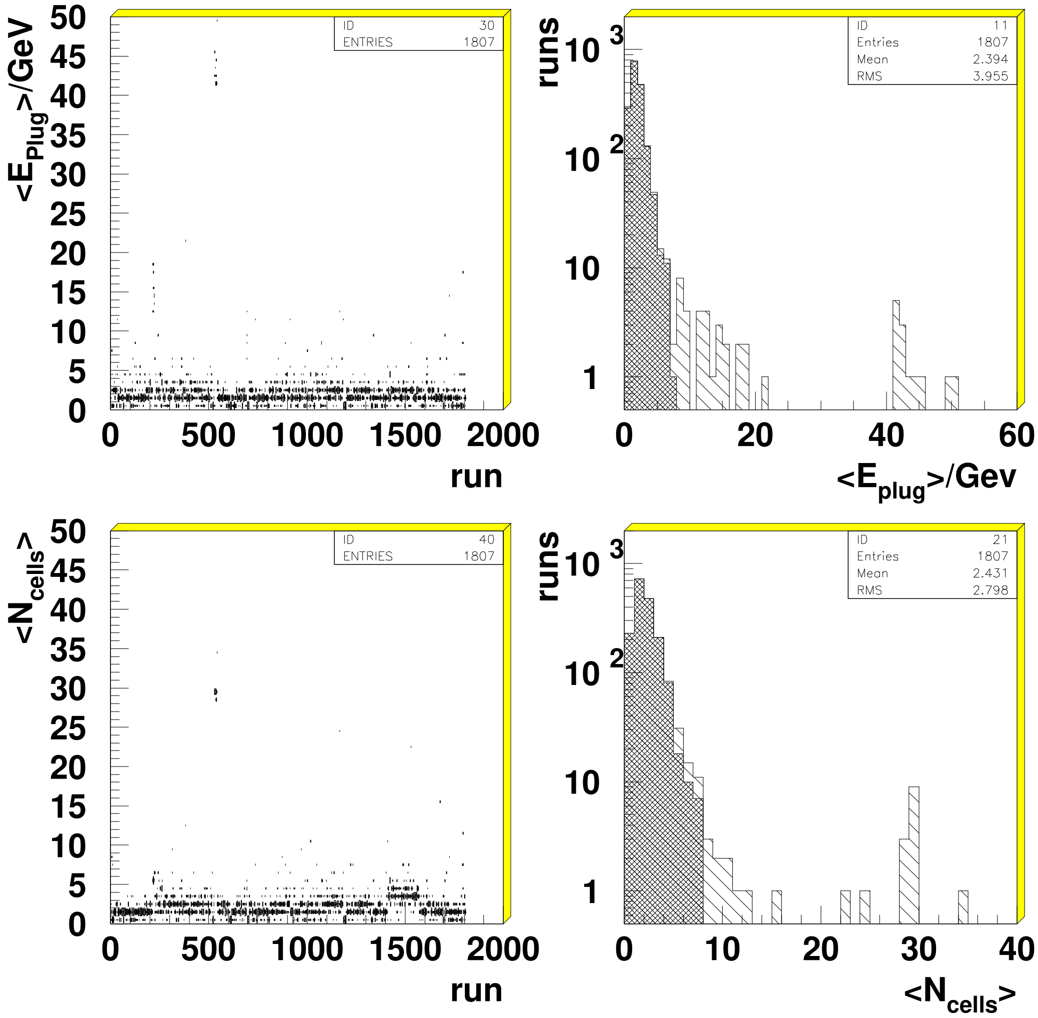

Figure 4.16: *On the left-hand side the plots of the average energy per run vs. run index and the average cell multiplicity per run vs. run index are shown. On the right-hand side the distribution of these average values are shown. The shadowed distributions are obtained requiring the conditions (4.3)*

PLUG analogue-box supplying a PLUG *quadrant*. This is an indication that the problem might be probably connected to the multiplexing of the channel signals or induced by electronics of neighboring sub-systems.
Using this analysis on the random trigger events it is possible to lock the noisy cells for these runs and avoid the loss of data. For the following analysis in the loss of 100 nbarn^{-1}

of data is not important.

The random trigger data will be used later to perform a statistical subtraction of the energy due to the noise and the pile-up in the energy measurement.
The existence of a long tail in the distributions shown in figure 4.18 is to be attributed to pile-up and coincidence of the random trigger signal with beam wall and beam gas events present with a rate $\approx 100\ kHz$ in the experimental region (see table (3.3)).

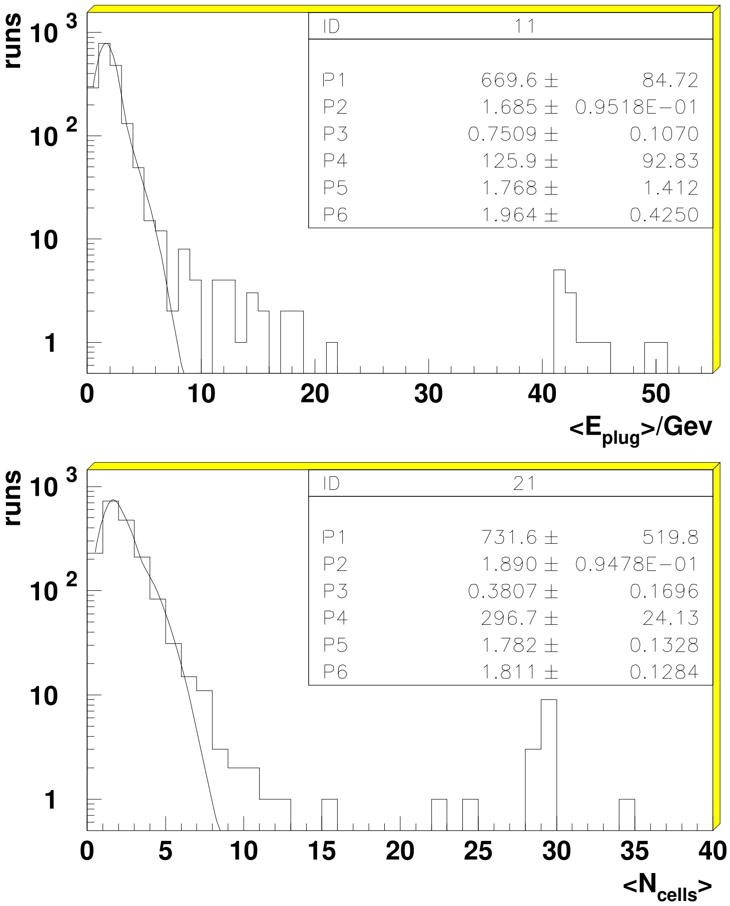

Figure 4.17: *Average energy and multiplicity distribution fits using double Gaussian function. The parameters P1 ... P6 are the max height, mean and* σ *of the first and the second summed Gaussian functions.*

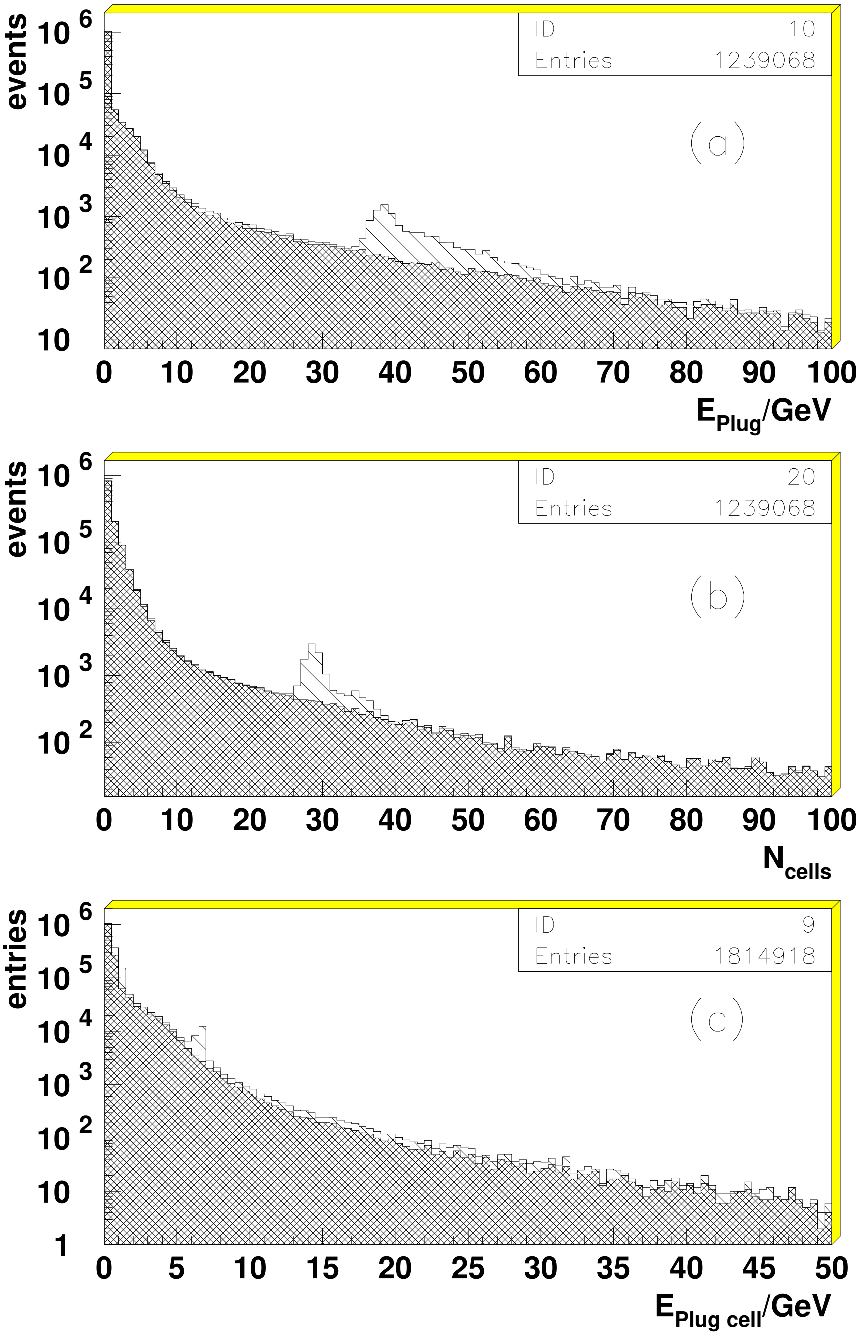

Figure 4.18: *The distributions shown here are related to random trigger events collected during 1994 positron running (1807 runs between run N. 82961 and 90419). They show (a) the total energy in the PLUG, (b) the PLUG cell multiplicity and (c) the PLUG cell energy spectrum. The shaded histograms in each plot are after the exclusion of runs with electronics problems*

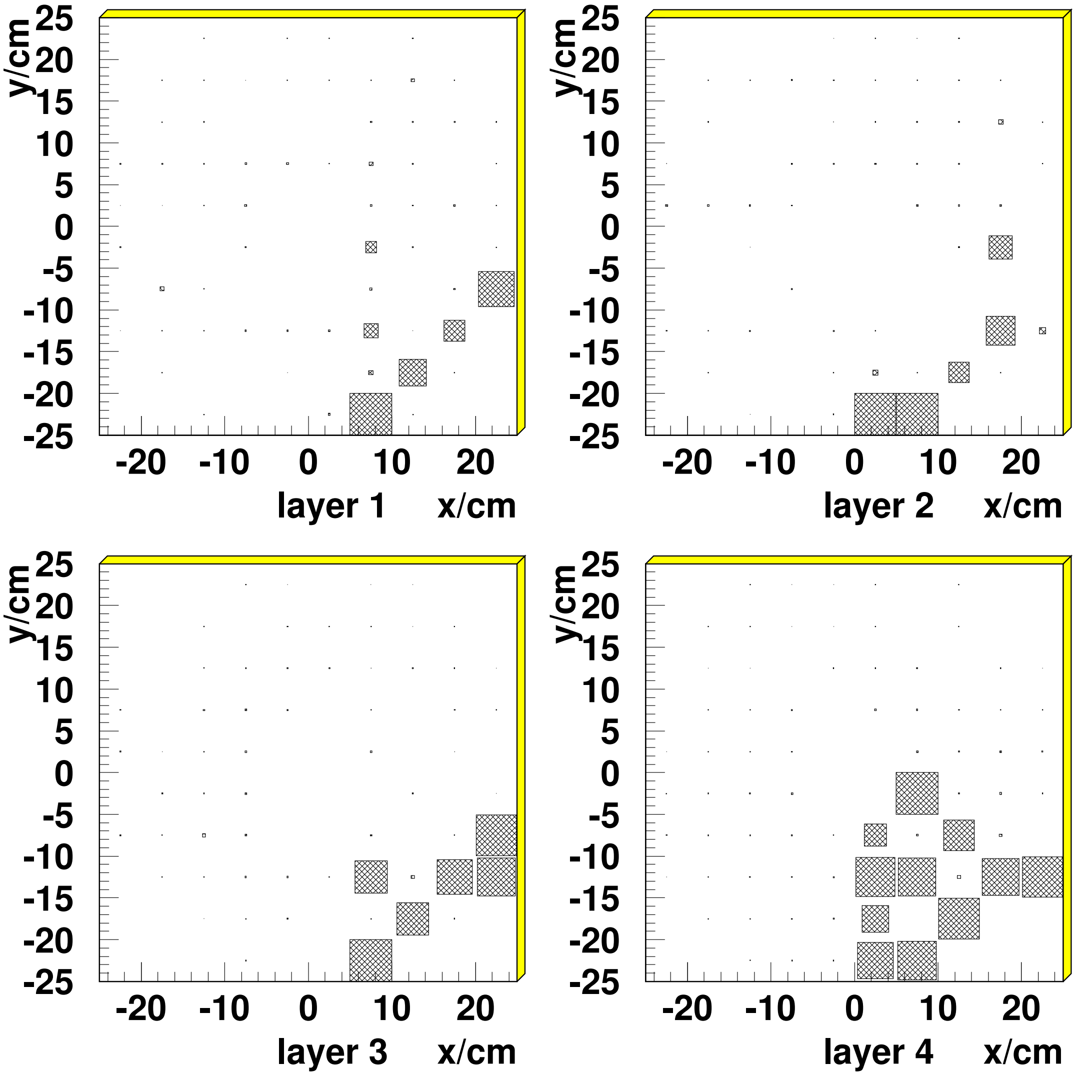

Figure 4.19: *The energy deposition in the calorimeter cells of the four layers obtained using random trigger events. The shadowed area is proportional to the energy deposition in the calorimeter cell. The events belong to runs for which the mean energy and the mean multiplicity per run is larger than 8 GeV and 8 cells respectively*

Chapter 5

Energy measurement with the PLUG

5.1 The measurement method

In this chapter the most important aspects of the energy measurement performed using the PLUG calorimeter are discussed.

The energy calibration of the PLUG calorimeter represents the foundation of the energy measurement with this device and it is based on two main parts. The first consists of determining the relationship between the deposited energy in the active region of the calorimeter and the pulse height of the produced signal. In the second part of the calibration, the ratio of visible energy over the energy of the incoming particle is investigated. This is called in the following effective sampling fraction (S_f^{eff}) of the calorimeter. The determination of S_f^{eff} is achieved using MC-simulations and is supported by the results of test beam experiments on Si-instrumented calorimeters.

Once these two main calibration parameters are known, the measurement of the total deposited energy in the calorimeter is performed by measuring the total pulse height corresponding to an event and rescaling this value according to the calibration of the electronics and to the effective sampling fraction.

The energy measurement can be used in the physics analysis of ep scattering events, but only when this is correlated with the energy of the particles originating from the interaction point and scattered within the calorimeter angular acceptance. Because of the presence of inactive material distributed between the nominal interaction point and the PLUG calorimeter, a considerable fraction of particles emitted within the PLUG angular acceptance are absorbed or scattered off the solid angle of acceptance before they can reach the calorimeter. The main consequence is that the energy deposited in the PLUG is on average much lower than the energy of the primary particles.

In ch. 5.5 a method is presented, which permits the determination of the energy of the primary particles using a large part of the information contained within the PLUG data. Using this method, to correct for the energy losses in the inactive material, the energy distribution of particles in the PLUG angular acceptance can be reconstructed. The correlation plot of generated energy vs. *corrected* energy indicates that the method permits an energy measurement on an event by event basis.

5.2 Energy calibration of the PLUG calorimeter

The starting point for the energy measurement using the PLUG is the calibration of the Silicon diodes and of the H1-PLUG readout electronics.
The idea is to calibrate a charge injector consisting of a charge capacitor and of a precision pulser, with the PLUG silicon detector response to a well known energy deposition (see fig. 5.1). Then using the calibrated charge injector, the signal which would be given by an irradiated PLUG silicon diode is reproduced. The relative uncertainty on the energy calibration of the charge injector is below 0.1 % and therefore negligible for the calibration constant determination. The use of the charge injector allows the transfer of the energy calibration of the Si-detectors to the H1-PLUG electronics as illustrated in fig. 5.2.

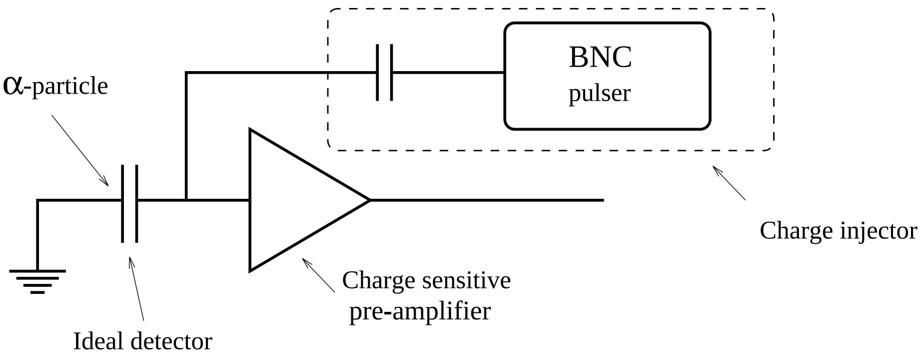

Figure 5.1: *Charge-injector calibration sketch. The charge signal from a silicon detector due to detection of an* α*-particle of energy* E_α *can be reproduced with high precision from the charge injector system.*

The energy/signal calibration of the charge injector was performed in the laboratory[1]. The experimental setup is shown in fig. 5.3. For the realization of the measurement a PLUG Si-detector has been irradiated with α-particles from a curium radioactive source having the following decay mode [43]:

$$^{244}_{96}Cm \longrightarrow \begin{cases} \alpha_1 & 5.763\,MeV & 24\% & + \text{Pu L x} - \text{rays} \\ \alpha_2 & 5.805\,MeV & 76\% \end{cases}$$

When one of these particles impinges upon a silicon diode, it is stopped by the silicon within a range $r \simeq 30\ \mu m$ [63]. The particle releases the total kinetic energy and produces in the silicon a large number of electron-hole pairs exactly proportional to the α-particle

---

[1] I. Institut für Experimentalphysik Universität Hamburg.

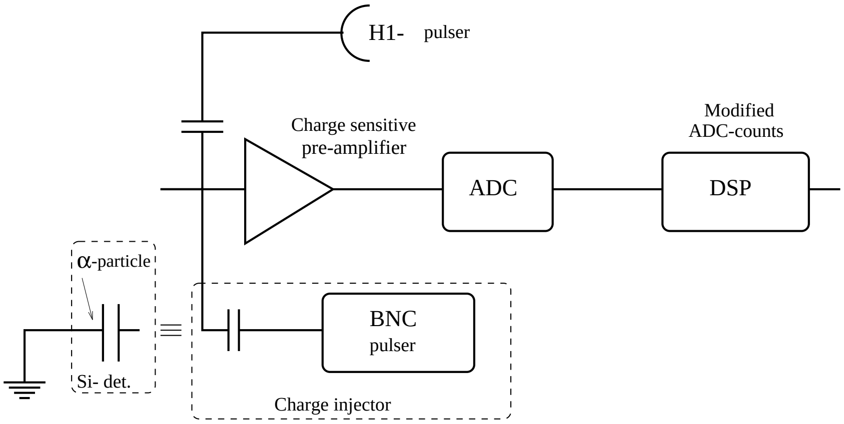

Figure 5.2: *H1-PLUG electronics calibration sketch. The energy calibrated signal from the charge injector is processed like the signal of a PLUG detector. Thus the ratio energy over ADC counts can be derived.*

energy. The number of electron-hole pairs produced, is of the order of 10^6 since the energy needed to produce one pair is $\epsilon = 3.6$ eV and the collection charge efficiency is $\sim 100\%$ (see ch. 4.3 and 4.1).

Using the multi-channel analyzer as illustrated in the experimental setup (fig. 5.3), it was possible to record the spectrum of the Curium source detected using the Si-diode and two reference signals produced by the charge injector. The reference signals are obtained by setting two different amplitude levels on the pulser. This permits the calculation of the pulser setting which corresponds to the energy $E_\alpha = 5.805$ MeV of α-particles chosen for the calibration. Figure 5.4 shows the spectrum of the Curium source and the two peaks produced by injecting charge in the acquisition circuit.

The use of the charge injector allows the transfer of the laboratory calibration of a PLUG detector to the H1-PLUG electronics. The signal due to the α-particles (5.805 MeV) is then measured within each channel of the H1-PLUG electronics (described in ch. 4.4). The average measured result is $\langle E_\alpha \rangle = (71.2 \pm 0.2)\ ADC_{counts}$. The distribution of the α-signal for the different PLUG channels is stable in time being $\sigma(E^i_\alpha)/\langle E^i_\alpha \rangle \simeq 0.03$. From this measurement the ratio $C_{el} = \frac{Energy}{ADC} = 81.5 \pm 0.2$ KeV is derived [61, 62].

The determination of the $\frac{Energy}{ADC}$ ratio sets the scale of the "visible" energy i.e. the energy deposited in the active part of the calorimeter.

Effective sampling fraction

Formally the total absorbed energy in the calorimeter, can be obtained by dividing the energy deposited in the active part of the calorimeter by the sampling fraction (S_f). Where S_f is defined as the ratio between the deposited energy in the active material and

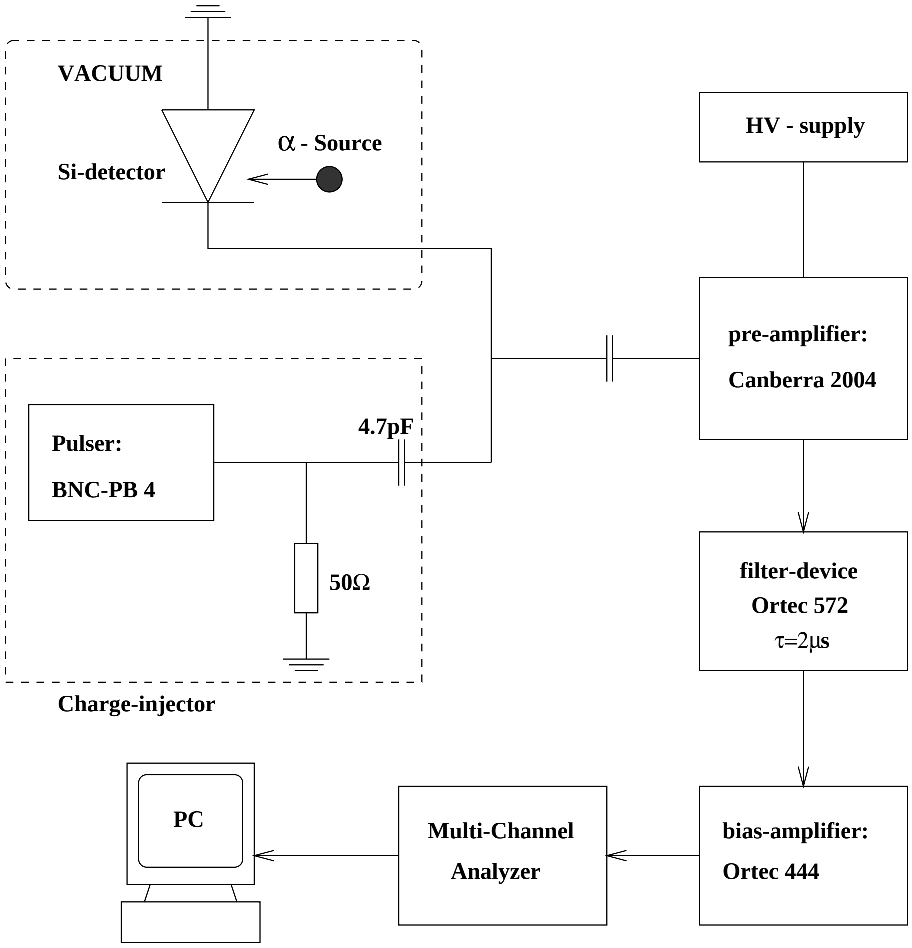

Figure 5.3: *Laboratory setup for α-signal measurement and charge-injector calibration. The source and the silicon detector are located in a vacuum chamber.*

the deposited energy in the whole calorimeter. The expression of this definition reads[2]:

$$S_f = \frac{\int_{act} \frac{dE}{dx} dx}{\int_{act} \frac{dE}{dx} dx + \int_{abs} \frac{dE}{dx} dx}$$

This definition would be adequate (for the actual energy calibration) only for calorimeters in which the total energy of the incoming particle is absorbed (i.e. for a calorimeter depth $\geq 8\lambda$). A more useful definition of the sampling fraction, for the application to calorimeter with limited length, is the ratio between the energy deposited in the active layers and the

---

[2] The sampling fraction is often defined as:

$$f_{samp} = \frac{(dE/dx)_{MIP}[1\ readout\ layer]}{(dE/dx)_{MIP}[1\ readout + 1\ absorber\ layer]}$$

where $(dE/dx)_{MIP}$ indicate the mean specific energy loss for Minimum Ionizing Particle (MIP) in a given material [71].

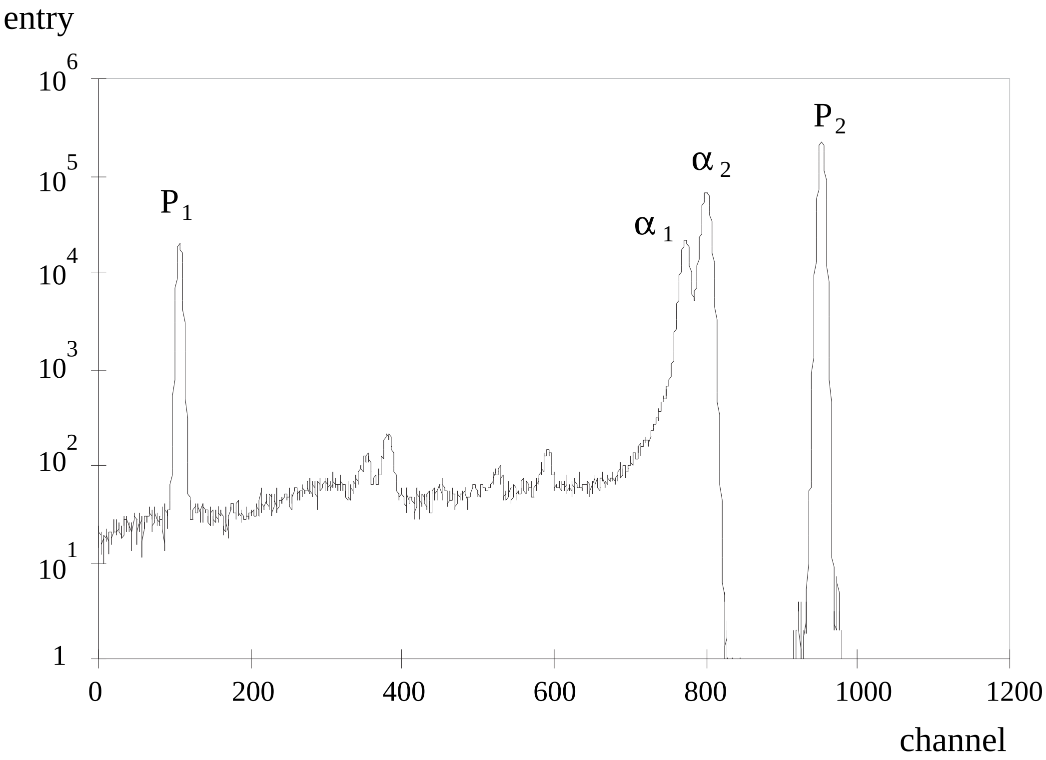

Figure 5.4: *Pulse-height spectra of a* $^{244}_{96}Cm$ *α-source.*

energy of the incoming particles:

$$S_{frac} = \frac{\int_{act} \frac{dE}{dx} dx}{E_{inc}}$$

The ratio defined here permits the determination of the energy of the incident particles even in case of limited calorimeter length. With such a definition the sampling fraction depends on the geometry and materials used in the construction of the calorimeter, but also on the type and energy of the incident particle. Last dependence exists for each calorimeter, in which the relative response to electromagnetic and to non-electromagnetic shower components is not equal to 1 ($e/h^{intr} \neq 1$ in case of non-compensating calorimeters) [70, 71].

The dependence of the sampling fraction of the PLUG has been studied for electrons and charged pions as a function of the particle energy using MC simulations. The results of this study are reported in the first three columns of table 5.1 [42]. The entries in the last column are the values for a sampling fraction calculated for the expected mixture of incident hadrons produced during the hadronization phase (see ch. 2.4). For the calculation of $S_f^{mix}(E)$ the following simple formula has been used:

$$S_f^{mix}(E) \simeq \frac{1}{3}\Big[2S_f^{\pi^-}(E) + S_f^{e^-}(E)\Big] \qquad (5.1)$$

This equation is based on the following approximations:

1. the number of pions produced during the hadronization is on average one order of magnitude larger than the number of other produced hadrons and for the high

i	E_i /GeV	$S_f^{e^-}(E_i) \times 10^{-3}$	$S_f^{\pi^-}(E_i) \times 10^{-3}$	$\sim S_f^{mix}(E_i) \times 10^{-3}$
1	2.0	1.23	0.76	0.92
2	8.0	1.33	0.81	0.98
3	16.0	1.32	0.81	0.98
4	32.0	1.31	0.83	0.99

Table 5.1: *PLUG sampling fractions for electrons ($S_f^{e^-}$), and negative pions ($S_f^{\pi^-}$) calculated with MC simulations for different energies (E_i) of the incident particles. In the fourth column the sampling fraction for the expected mixture of incident hadrons is indicated (S_f^{mix}). The errors on the sampling fractions due to the MC calculation are negligible. The error on the determination of the sampling fractions due to reliability of the simulations will be discussed in the next section.*

energies of the incoming hadrons the strong interaction depends only weakly on the type of hadrons involved.

2. the mean multiplicity of each type of produced pion is the same; this because for the strong interactions occurring during the hadronization all pions are equivalent particles.
3. the charged pions ($\pi^{\pm}$) are equivalent in producing hadronic showers, thus the sampling fraction for pions with opposite charge is the same ($S_f^{\pi^+} = S_f^{\pi^-}$);
4. the interaction of a neutral pion with the calorimeter is experimentally equivalent to the electron interaction [3] ($S_f^{e^-} = S_f^{\pi^0}$);

From points 1. and 2. it follows that:

$$S_f^{mix}(E) \simeq \frac{1}{3}\Big[S_f^{\pi^+}(E) + S_f^{\pi^-}(E) + S_f^{\pi^o}(E)\Big] \tag{5.2}$$

Considering points 3. and 4. eq. (5.2) can be transformed into eq. (5.1).

In order to complete the calibration, it is necessary to determine the effective sampling fraction (S_f^{eff}) independently from the energy of the incident particles. A good approximation of the effective sampling fraction can be obtained using the following formula:

$$S_f^{eff} = \sum_i P(E_i) \cdot S_f^{mix}(E_i) = \frac{1}{3}\sum_i P(E_i) \cdot \Big[2S_f^{\pi^-}(E_i) + S_f^{e^-}(E_i)\Big] \tag{5.3}$$

where the factors $P(E_i)$ are the probabilities to find a hadron with energy E_i in the interval $(E_i, E_i + \Delta E_i)$.
The values of $S_f^{mix}(E_i)$ are given in table 5.1 while the probabilities $P(E_i)$ can be obtained from the energy spectra of the particles generated after the hadronization. Figure 5.5 shows the energy spectra of particles produced in the PLUG angular acceptance range

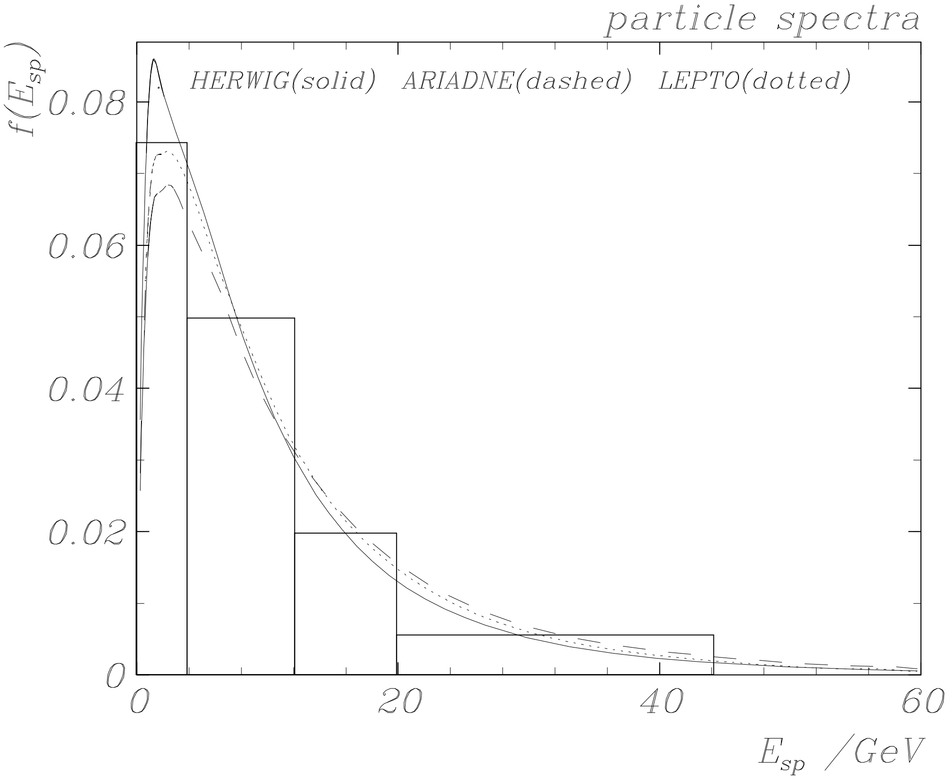

Figure 5.5: *Energy spectra for single particle generated in the PLUG angular acceptance using different MC models. With the chosen normalization $f(E_i)$ is the probability density. The overlayed histogram has been used in the determination of S_f^{eff} using eq. (5.3).*

using some different MC models presented in ch. 2.4 . Since different models produce very similar energy spectra [4] the determination of S_f^{eff} is model independent to a good approximation. The overlayed histogram, shown in the same figure has been used for the determination of the probabilities in eq. (5.3). The obtained result for the effective sampling fraction calculated using eq. (5.3) (and (5.6) for the error) is:

$$S_f^{eff} \cong (0.964 \pm 0.081) \times 10^{-3}$$

---

[3] This is because π^o's (mean life $\tau \sim 8 \cdot 10^{-16}$ s) decay essentially to gamma pairs ($\simeq$ 98%) or a gamma plus an electron-positron pair ($\simeq$ 2%) [43]

[4] However differences between the MC models can be observed in the multiplicity distributions (see fig. 5.22).

this finally allows the determination of the deposited energy in the PLUG cells using the equations based on the following:

$$E_i = \frac{C_{el} \cdot K_i}{S_f^{eff}} \cdot N_{ADC} \tag{5.4}$$

where the index i runs over the individual calorimeter channels and K_i is the inter-calibration factor between the channels.

5.3 Calibration error determination

This section deals with the calculation of the errors concerned with the PLUG calorimeter calibration. The calculation is based on the error propagation derived from equation (5.4) which contains the possible error sources in a compact form.
The relative error on the energy deposited in the PLUG can be expressed by adding in quadrature the three contributions present in eq. (5.4) as expressed in the right-hand side of the following equation:

$$\frac{\Delta E_i}{E_i} = \sqrt{\left(\frac{\Delta C_{el}}{C_{el}}\right)^2 + \left(\frac{\Delta S_f^{eff}}{S_f^{eff}}\right)^2 + \left(\frac{\Delta K_i}{K_i}\right)^2} \tag{5.5}$$

The first term $\Delta C_{el}/C_{el}$ expresses the relative error on the calibration of the H1-PLUG electronics; it is below 0.1% as stated in the previous section and it is negligible.
The contribution $\Delta K_i/K_i$ arises from the different gains of the individual channels and is also negligible, because each time the calibration parameters are down loaded in the DSP an equalization of the gains occurs and $\Delta K_i \to 0$ [5].
However, unlike the previous terms the contribution to the error depending on S_f^{eff} is not negligible. S_f^{eff} is a derived quantity (see eq. (5.3) and (5.1)) which depends on the following three functions: $S^{\pi^-}(E)$, $S^{e^-}(E)$, $P(E)$. Thus the knowledge of the error on the single functions is necessary for the propagation of the error on S_f^{eff} .
The determination of the error on the charged pion sampling fraction $S_f^{\pi^-}(E)$ is performed by comparing experimental data from a pion test beam experiment performed at ITEP(Moscow) [49] with the respective Monte Carlo simulation obtained using GEANT [72] with GHEISHA [74] as shower code.
The test-beam experiment was performed using PLUG Si-detectors as active material in a sampling calorimeter with iron as absorber material. The sampling of the deposited energy was performed using a readout layer every $\lambda/2$ of absorber material. This corresponds exactly to the PLUG sampling structure and therefore the relative difference between data and simulated response provides a determination of the relative error on the sampling fraction $S_f^{\pi^-}$ of the PLUG calorimeter. The result of the data-MC comparison for 5 GeV impinging pions is shown in fig. 5.6. The shape of the shower development

---

[5] The distribution of the gains a_i for different PLUG channels is stable in time being $\sigma(a_i)/\langle a_i \rangle \simeq 0.03$

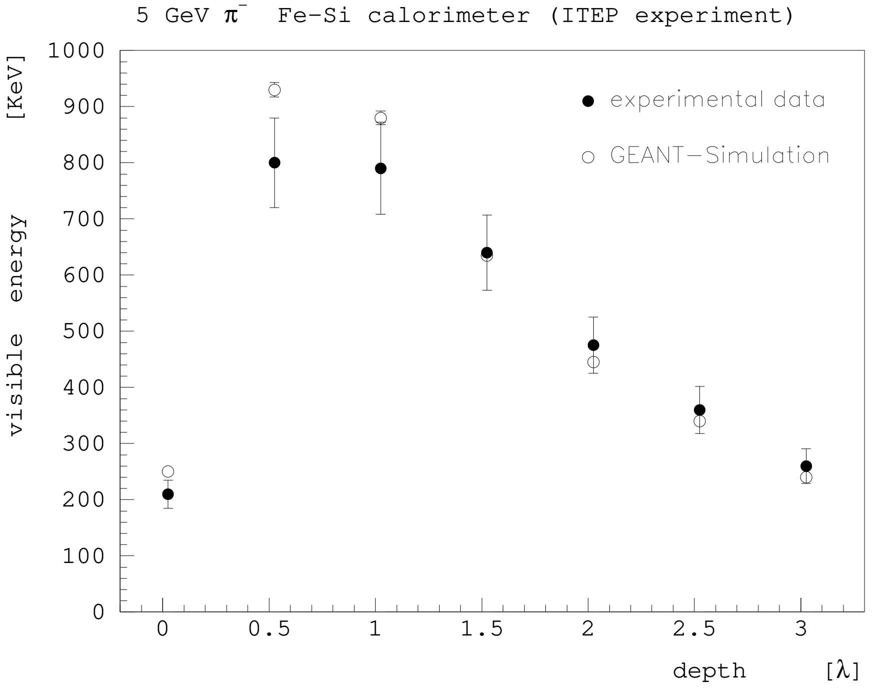

Figure 5.6: *Data-MC comparison of the energy measured in the silicon as a function of the calorimeter depth for 5 GeV* π^- *.*

is well described by the simulation; the relative difference between data and MC of the total response integrated over three interaction lengths is $\simeq$ 5%.

The ITEP experiment confirms the possibility of simulating the energy deposition in the active material due to hadronic showers, within good accuracy. Also test-beam experiments performed by the SICAPO Collaboration, using Fe-Si and U-Si sampling calorimeters, confirm the possibility of simulating the hadronic shower development within 5 - 10 %. Results of data and MC-simulation of these test-beam experiments can be found in [64]. By relying on the results of the ITEP experiment, a conservative estimate of the relative error on the determination of the charged pion sampling fraction is: $\Delta S_f^{\pi^-}/S_f^{\pi^-} =$ 10%. The error is assumed to be constant or at least not larger then 10 % over the energy interval from 2 to 32 GeV used for the S_f^{eff} determination performed here.
The error associated with the determination of the *electromagnetic* sampling fraction $S_f^{e^-}$ is assumed to be constant to first order over the considered energy interval (see table 5.1) and to be not larger than 3 %. This error magnitude is also a conservative estimate: experimental data of a silicon calorimeter test beam with electrons have been reproduced within an accuracy of $\simeq$ 2% for e^- energy between 2 - 6 GeV [45, 46] using EGS4 [65]. The reliability of the data simulation of a silicon instrumented calorimeter using EGS4 and GEANT has been demonstrated experimentally allowing for the small thickness of the Si-diodes in the simulation [66, 67, 68, 69]. Figure 5.7 shows the electromagnetic

shower development induced by 6 GeV electrons in a silicon tungsten calorimeter and the comparison with the simulations [64]. The error associated with the energy spectrum of

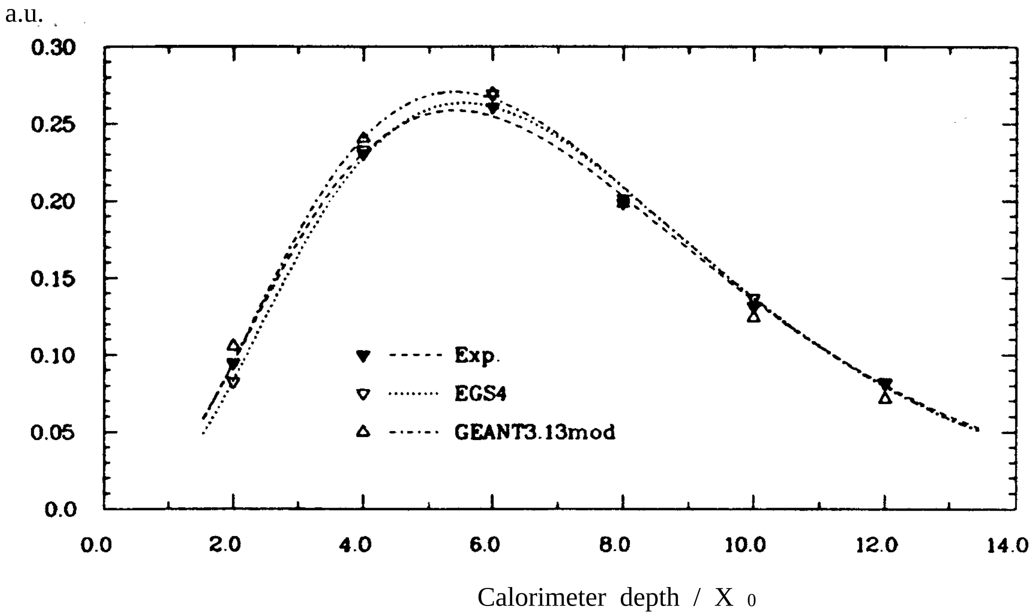

Figure 5.7: *Electromagnetic shower development induced by 6 GeV electrons in a Si-W calorimeter compared with MC simulation.*

the particles hitting the calorimeter is estimated from the different energy spectra shown in fig. 5.5 obtained using different models. The magnitude of the relative error is in this case 5 %. Thus by adding the three error terms weighted according to eq. (5.3), it is possible to calculate the relative error on S_f^{eff} using the following equation:

$$\begin{aligned} \frac{\Delta S_f^{eff}}{S_f^{eff}} &= \sqrt{\left(\frac{\Delta P}{P}\right)^2 + \left(\frac{2\Delta S^{\pi^-} + \Delta S^{e^-}}{2S^{\pi^-} + S^{e^-}}\right)^2} \\ \frac{\Delta S_f^{eff}}{S_f^{eff}} &\simeq \sqrt{\left(\frac{\Delta P}{P}\right)^2 + \left(\frac{2}{3}\frac{\Delta S^{\pi^-}}{S^{\pi^-}}\right)^2 + \left(\frac{1}{3}\frac{\Delta S^{e^-}}{S^{e^-}}\right)^2} \simeq 0.084 \end{aligned} \tag{5.6}$$

which is also the relative error on the energy deposition in the PLUG calorimeter.

5.4 The simulation of the PLUG calorimeter in H1

The full simulation of an experiment like H1 can be divided in several parts (see ch.2.4). In this section the interaction of generated particles with the H1 detector is discussed. Particular emphasis is given to the region between the nominal interaction point and the PLUG since this produces relevant effects on the PLUG energy measurement. The simulation of the detector and of the interaction between particles and the detector or

accelerator components represents a fundamental element in high energy physics experiments. The precision of the simulation determines the interpretation of the measurement and the evaluation of the associated errors.
The simulation code of the PLUG used in this work is contained in the H1SIM [73] software package of the H1 collaboration which permits the full simulation of the H1 detector. Figure 5.8 shows the geometric description of the H1 detector as implemented in the simulation. The description of the detector geometry and the interaction of the event particles with the detector material is based on GEANT3.15 (1994) and earlier versions. The simulation of the calorimeter information, the data structure, their format and the effects due to the H1 processing electronics is performed by special H1 routines of H1SIM[6].

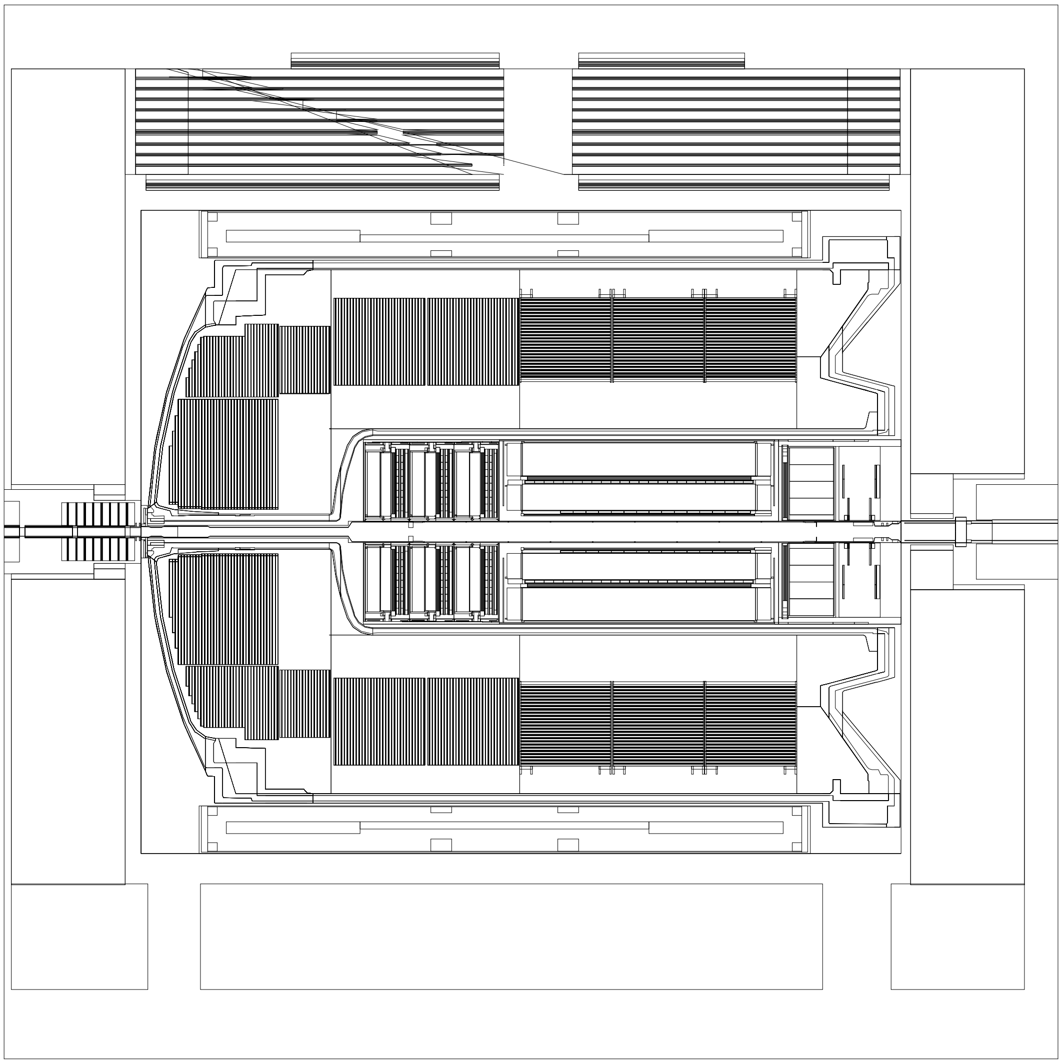

Figure 5.8: *Main part of the H1 detector as implemented in the H1 simulation program.*

---

[6] The package has a modular structure. A software "module" exists for every sub-detector: the PLUG data simulation is obtained by calling the PDIGI sub-routine.

The different transport codes available in GEANT permit the tracking of the produced secondary particles according to the particle type and their energies. For the simulation of the electromagnetic interaction of electrons, positrons and photons essential parts of the EGS4 simulation code have been included. The simulation of the energy loss by ionization of the charged particles is performed by special sub-programs in GEANT according to the energy losses in the specified material. The fluctuations around the average value of the energy deposition ionization are simulated using approximated Landau probability distributions. The explicit production of δ-ray and their simulation is also performed.

The simulation of the hadron-nuclear interaction and the consequent hadronic shower development can be performed using the GHEISHA simulation code or using CALOR89 [78].

GHEISHA is used in H1 as standard code for the production of simulated data. It utilizes different collision models depending upon the energy involved in the hadronic interaction. A general characteristic of this code is the parameterization of physical variables tuned to experimental data. The use of different parameterizations in GHEISHA is often inspired by theoretical models, however this code does not represent the simulation of a model or of a theory [74]. In spite of the raw parameterization and interpolation of the hadronic cross section at momenta below a few GeV, the nuclear resonance region, the calculated calorimetric response is in good agreement with the signal response of different calorimeter types.

The CALOR89 package consists of several programs permitting the detailed simulation of hadronic interactions down to an energy of 1 MeV. For the interaction of hadrons with momenta larger than 10 - 15 GeV/c the program uses FLUKA [75], which is also available as a GEANT option and for particle momenta below 10 - 15 GeV/c the code HETC [76] is used. Finally CALOR89 allows a particular detailed tracking of low energy and of thermal neutrons performed by MORSE [77] simulation code.

The use of this code is clearly advantageous for experiments using compensated calorimeters where low energy neutrons play a fundamental role in the understanding of the detector response [78].

Different simulation options exists for both hadronic transport codes (GHEISHA and CALOR) of H1SIM. These permit the simulation of the detector with different levels of detail and within different energy cuts on the particles tracked[7]. The minimum energy value allowed in GEANT is 10 KeV which is low enough to permit realistic simulations in Si-sampling calorimeters.

The simulation of the PLUG calorimeter in particular is characterized by the small Si-detectors thickness. In order to obtain reliable results the user-simulation parameters[8] have been optimized according to the studies cited in ch.5.3 and have been implemented in H1SIM [42].

The detailed simulation option requires very high computation times, thus its use is re-

---

[7] The user can set the minimum values of energy below which the energy of the particle is deposited in the present detector volume and no further tracking is performed.

[8] CUTELE, CUTGAM, CUTNEU, CUTHAD,and CUTMUO are the parameters to set the minimum energies for the track-simulation of electrons, gammas, neutrons, hadrons and muons. DEEMAX sets the maximal energy loss in the simulation of a tracking step and BCUTE, DCUTE influences the frequency of Bremsstrahlung and δ-ray processes

stricted to special detector studies as for example in the determination of the PLUG sampling fraction in ch.5.2. The detailed simulation options cannot be used for mass production of Monte Carlo events used in the physics analysis of the ep scattering.

For MC production a special fast simulation named H1FAST has been developed [79]. This option uses simplified geometry configurations and averaged material properties within detector volumes containing different materials. For the PLUG calorimeter the simulation of electromagnetic showers are parameterized when at least 95 % of the shower is contained in only one PLUG volume [79]. In such cases, the energy of a particle that will not escape from a calorimeter cell, is deposited in the same cell. The energy deposition takes into account the sampling fraction without further particle tracking calculations[79]. For the hadronic interaction, since the shower parameterization is not as reliable as for the electromagnetic case, no parameterization is used.

Since all MC events used for the analysis of the *ep* scattering are simulated using H1FAST, it is necessary to verify the agreement level of the fast simulation with the reference results obtained using the detailed option.

The results of the comparison of single particle event are shown in figure 5.9. The comparison concerns the simulation of 1000 charged pion started from the interaction point and distributed in the angular interval $0.9^o < \theta < 3^o$ and over the full azimuthal angle. The plots contain the total PLUG energy and the cell energy distributions for the three different simulation options: fast+GHEISHA[9], detailed+GHEISHA and detailed+CALOR. Three pion energies have been considered: 5, 10 and 20 GeV. These particle energies have very high probability of production in *ep* scatterings at HERA within the considered rapidity region, as shown in fig. 5.5, thus the comparisons constitute a relevant test for a realistic simulation of *ep* events in the PLUG.

The comparison between the three presented simulation options shows, in general, a good agreement between the fast and detailed simulations. The agreement improves with increasing energy of the particles generated. The distributions of the energy per cell (right-hand side of fig. 5.9) show that the multiplicity of the cells with energy below one GeV is under-estimated in the fast simulation. This effect, which depends mainly on the simulation of the inactive material, is considered later in the evaluation of the systematic errors in ch.6.5 and does not affect the energy deposition which is, on average, well described.

For every simulation option, the average values of the PLUG energy are below the expected values (5, 10, 20 GeV). This can be interpreted as an indication of energy losses in the material present between the interaction point and the calorimeter and this is investigated in the next section.

The inactive material between the interaction point and the PLUG

The amount of inactive material between the interaction point and the PLUG calorimeter varies between 0.8 and 5 interaction lengths. The result is a reduced signal and a non-linear response of the calorimeter.

---

[9] H1 standard.

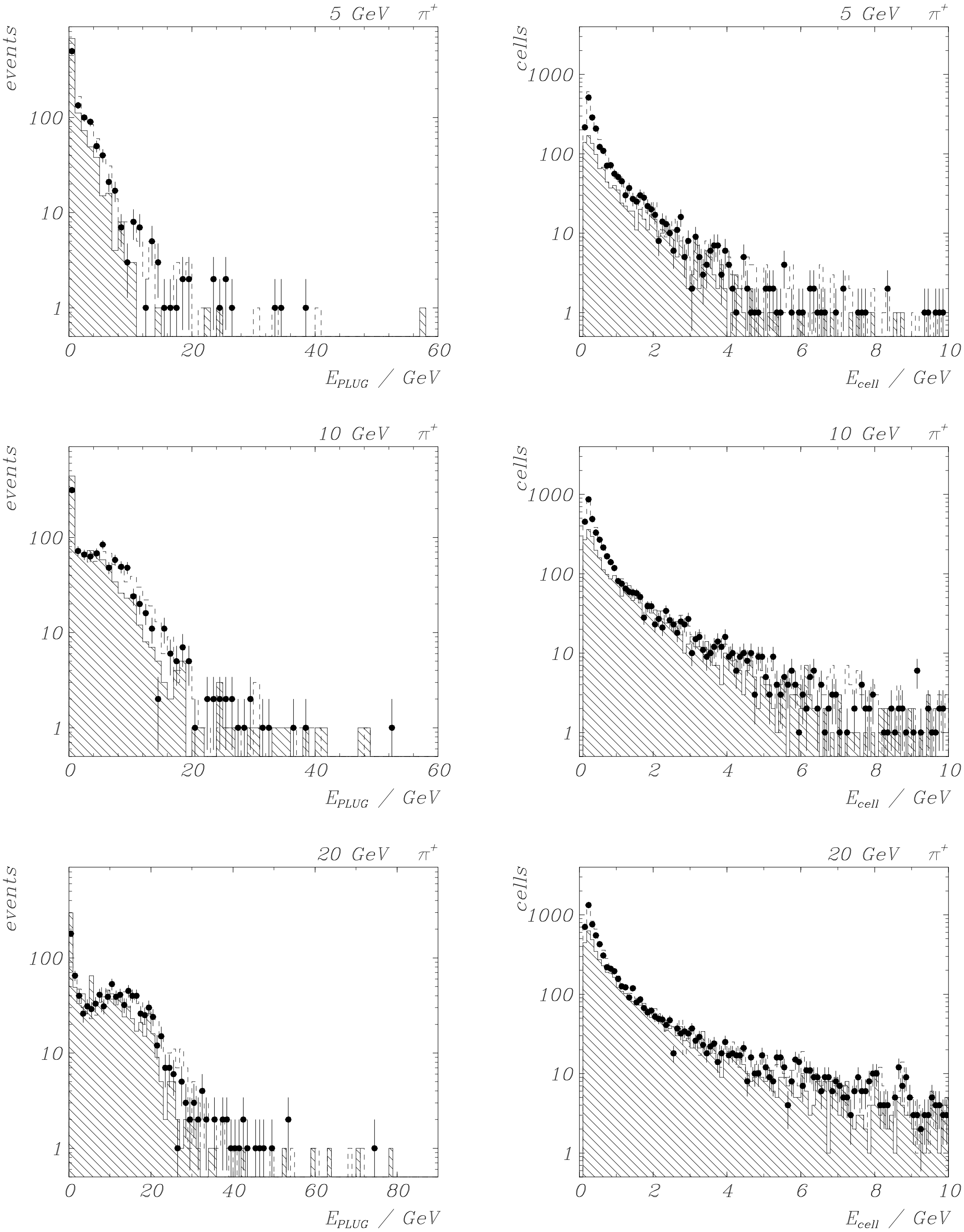

Figure 5.9: *PLUG-energy distributions and PLUG-cell energy spectra obtained using the H1SIM-GHEISHA (dots) H1SIM-CALOR (dashed histogram) and H1FAST-GHEISHA (shadowed histogram) simulation option for 5, 10 and 20 GeV charged pions.*

The mechanical structure of the H1 detector and the machine parts close to the beam pipe which constitute the inactive material are mainly: the C4 collimator and the vacuum pump placed in the forward tracker region of the beam pipe, the double walled cryostat for the liquid argon (IF region) and the flange systems between cryostat and beam pipe close to the PLUG. Figure 5.10 shows the distribution of the inactive material in interaction lengths as a function of pseudo-rapidity ($\eta = -\ln\tan\frac{\theta}{2}$). In this figure the PLUG acceptance region in angle (θ) is also indicated. A quantitative evaluation of the energy loss in the inactive material in a realistic case can be obtained by simulating events produced with a MC generator for the electron-proton DIS[10], as a particle generator. In

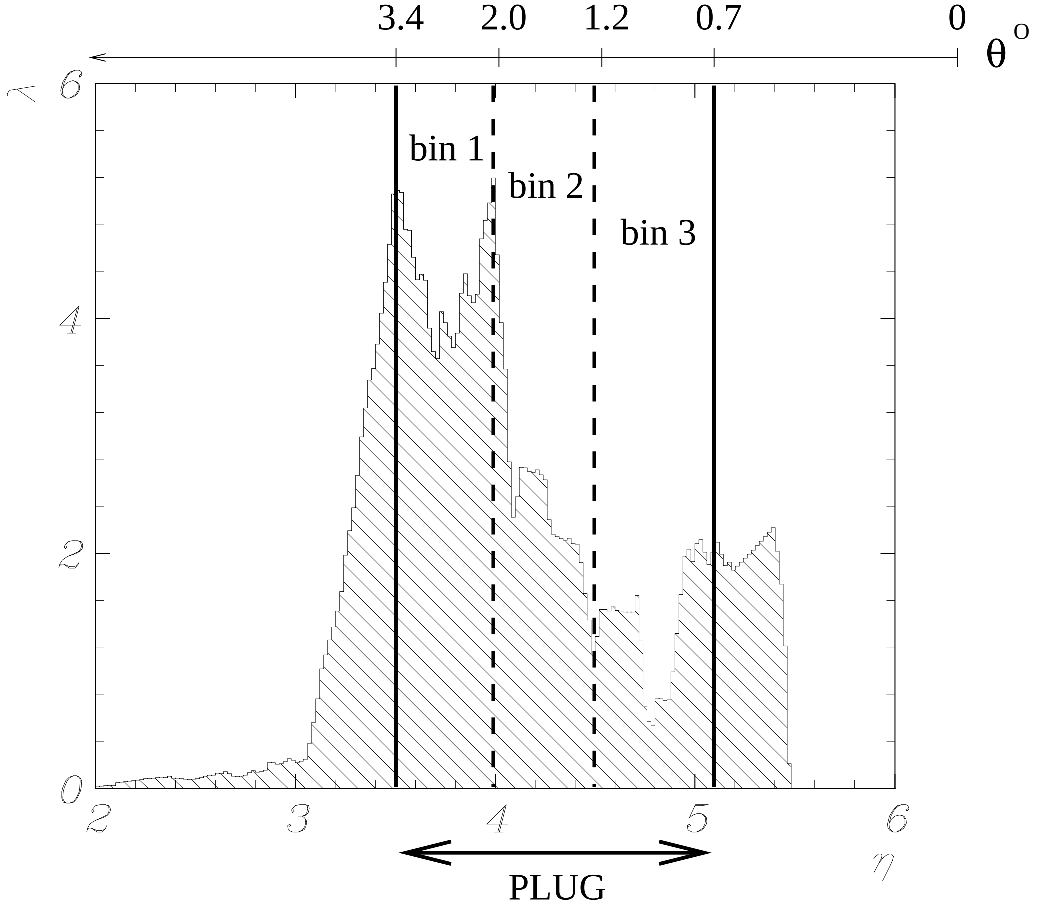

Figure 5.10: *Inactive material in front of the PLUG in term of interaction lengths λ as a function of pseudo-rapidity η (Configuration implemented in H1SIM for 1994). Indicated are three pseudo-rapidity regions (bins 1, 2, 3) defining three PLUG sections. At the lowest pseudo-rapidity the LAr cryostat (Al) and flange systems (steel) between cryostat and beam-pipe constituite the main amount of inactive material. At the highest pseudo-rapidity the main contribution is due to the C4 (W) collimator and to the beam pipe.*

---

[10] The MC generator used here was LEPTO6.1 [19].

the H1SIM simulation package it is possible to trace the energy per event deposited in the inactive material [80, 81]. Figure 5.11 shows four energy distributions: fig. a) is the total energy reconstructed in the PLUG (E_{rec}), b) the energy deposited in the inactive material between the PLUG and interaction region (E_{dead}) c) energy deposited within H1 ($E_{rec} + E_{dead}$) and d) is the total energy (E_{gen}) emitted within the angular acceptance range $0.6^o < \theta < 3.5^o$. From the average value of these distributions it is possible to evaluate the relative quantity of energy deposited within the calorimeter, within the inactive material and the energy which escapes from the detector. The results summarized in table 5.2 indicate that in a typical *ep* scattering event, the energy detected in the PLUG is 27 % of the energy emitted in its acceptance. Thus in order to use the PLUG as a

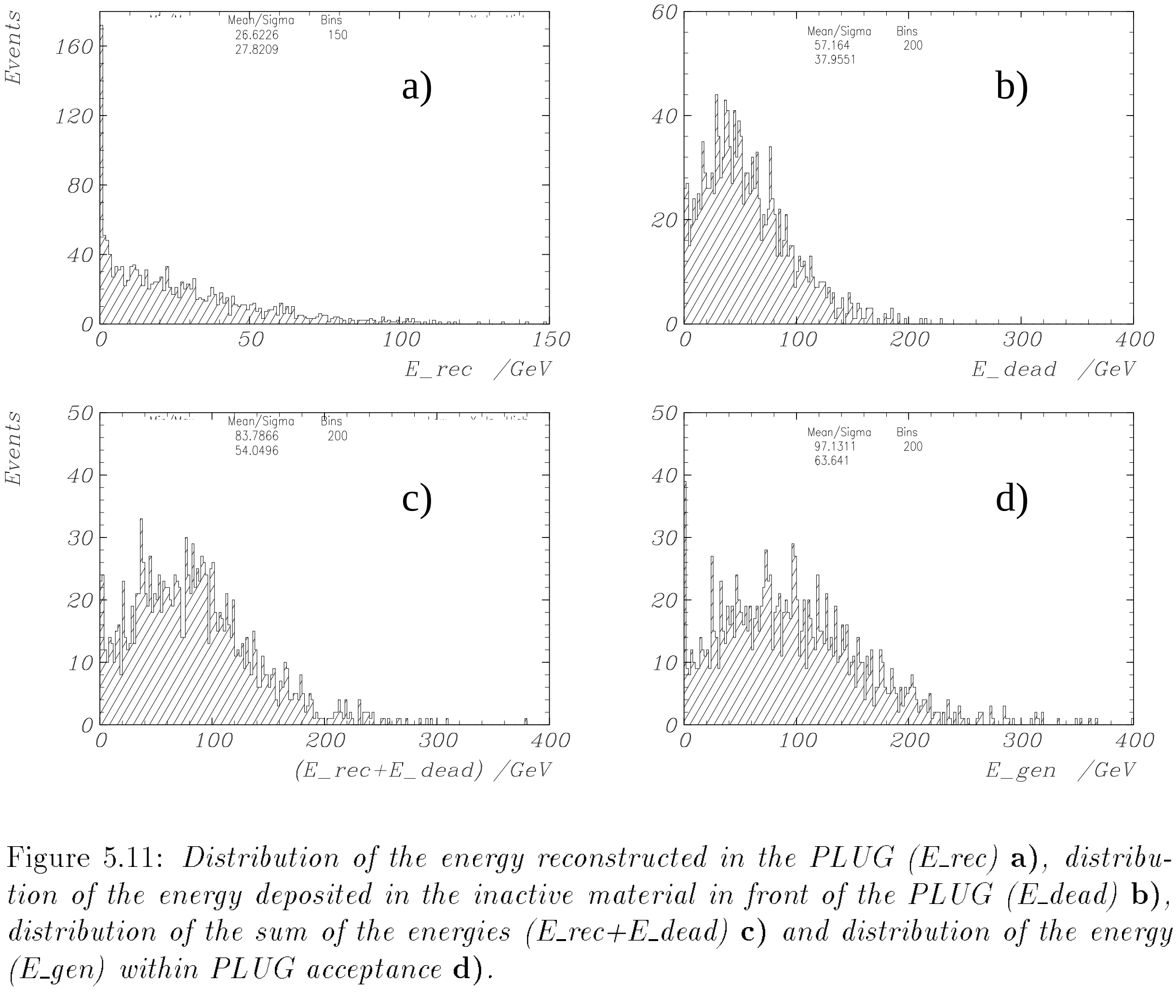

Figure 5.11: *Distribution of the energy reconstructed in the PLUG (E_rec)* **a)**, *distribution of the energy deposited in the inactive material in front of the PLUG (E_dead)* **b)**, *distribution of the sum of the energies (E_rec+E_dead)* **c)** *and distribution of the energy (E_gen) within PLUG acceptance* **d)**.

calorimeter it is necessary to correct the energy scale taking into account the energy losses affecting the measurements.

PLUG	$\simeq$ 27 %
inactive material	$\sim$ 59 %
Energy leakage	$\sim$ 14 %

Table 5.2: *Energy fraction deposited in the PLUG, in the inactive material in front of the PLUG and energy fraction lost due to the leakage, for a typical DIS energy flow into the calorimeter acceptance region.*

5.5 The inactive-material correction

The results of the simulation obtained in the previous section emphasize the difficulty of performing energy measurements using the PLUG, in the presence of inactive material ($0.8 < \lambda < 5$) screening the calorimeter.
In this section the possibility to perform an energy determination of the particles emitted within the PLUG-angular acceptance is investigated. A method to correct the PLUG-energy measurement based on MC simulation and on the knowledge of the inactive material distribution shown in fig. 5.10 is developed. The method makes use of the analogue response and of the good granularity of the calorimeter and allows a satisfactory correlation between generated and corrected energy.
In the following section the performance of the PLUG calorimeter within H1 after the inactive material correction is presented also in terms of energy resolution. Figure 5.12 summarizes the results obtained using the PLUG without correction. The simulated events used to produce the distributions have been generated using LEPTO6.1 with the mear option which corresponds to the ARIADNE4.03 program and have a squared 4-momentum transferred within the interval $5 \leq Q^2 \leq 100$ GeV^2. The upper plot shows the expected and the measured PLUG energy distributions plotted on a logarithmic scale. Both the shape and the average values of the distributions are in disagreement, being $\langle E_{gen} \rangle \approx 3.6 \cdot \langle E_{rec} \rangle$. The correlation between the two variables, shown in the bottom plot of fig. 5.12, provides evidence for the detection inefficiency produced by the inactive material and a consequent attenuation of the calorimeter signal. With this correlation the measurement of the energy emitted within the PLUG acceptance is not practicable.
As shown in figure 5.11, the observed difference can be understood in terms of energy deposition between the interaction point and the calorimeter and in terms of energy leakage out of the calorimeter. A correction of the measured energy, which re-establishes the correlation between measured and generated particles energy can be obtained considering the inactive material presence and the limited dimensions of the PLUG.
To correct the data it is necessary to determine the relationship between the reconstructed (E_{rec}) and generated energy (E_{gen}) distributions. The first order approximation of the correction reads:

$$E_{cor}(E_{rec}) = E_{rec} \cdot C \tag{5.7}$$

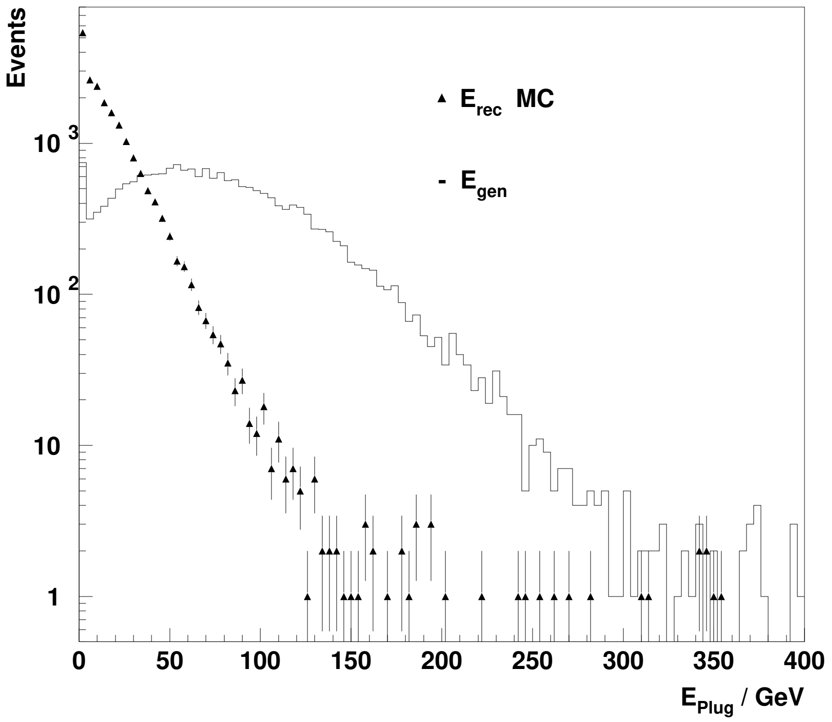

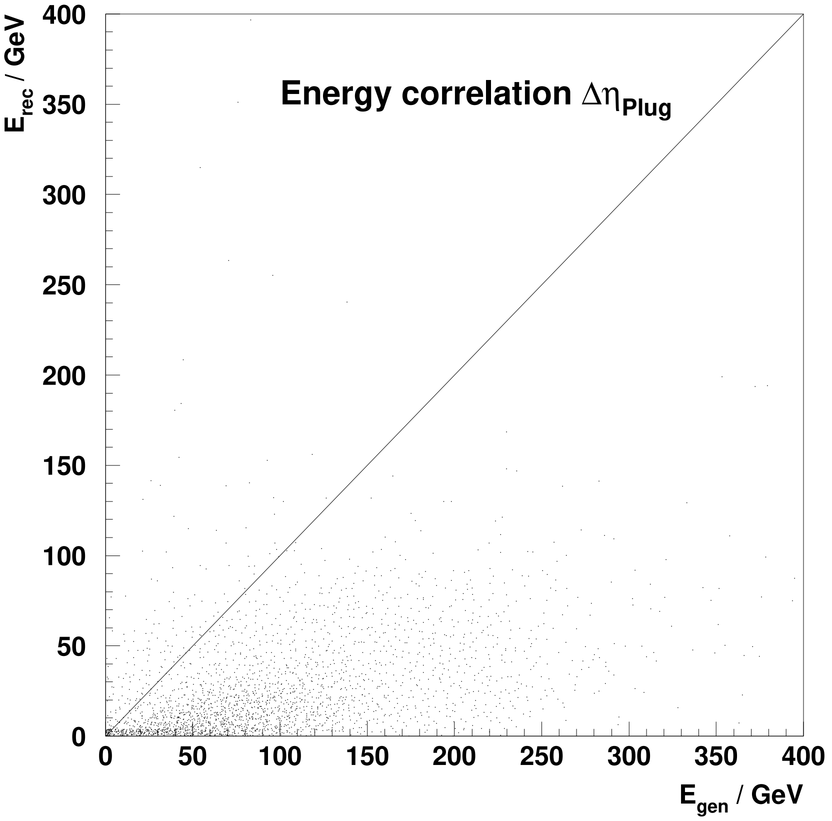

Figure 5.12: *The upper figure shows the distribution of PLUG reconstructed energy and the generated energy in the PLUG acceptance. The lower plot shows the poor correlation between the reconstructed and the generated energies.*

where E_{cor} is the corrected energy and C a constant obtained as ratio of the average values of the considered distributions:

$$C = \frac{\langle E_{gen} \rangle}{\langle E_{rec} \rangle} \tag{5.8}$$

In the ideal case the event by event correlation $E_{gen} \equiv E_{cor}$ would be required. This cannot be achieved using the first order correction given in (5.7). However using the equations (5.7) and (5.8) and by cosidering avarage values it follows that:

$$\langle E_{cor}(E_{rec}) \rangle = \langle E_{gen} \rangle$$

This relation is valid for the average values, whereas the energy determination event by event performed using eq. (5.7) is, in general, not correct. This is because the linear transformation introduced does not change the shape of the measured energy distribution (E_{rec}), which remains substantially different from the distribution of the generated energy (see fig. 5.12).

A more sophisticated correction can be obtained by introducing an energy dependence of the correction factor C. This is justified by the presence of the inactive material in front of the calorimeter which produces a non-linear response in energy of the PLUG. Furthermore because of the strong variation of the inactive material amount with pseudo-rapidity, the correction function will also be angular dependent. The general form of the correction function reads:

$$E_{cor} = f(E_{rec}, c_1, ..., c_n) \tag{5.9}$$

where c_i are parameters.

A method to calculate and parameterize the correction function is presented in the following. The calculation is based upon MC simulated events. The procedure used consists of a number of steps. As first the most probable value of generated energy which produces a reconstructed energy within a given interval is calculated. This is done for 16 intervals of the PLUG reconstructed energy. The intervals used are indicated in table 5.3. for each one of these intervals the distribution of generated energy can be produced; examples are shown in figure 5.13. For low values of the reconstructed energy the distributions shown are asymmetric around the peak value. In these cases the average generated energy does not coincide with the most probable value and moreover there is a systematic shift between the two estimators (most probable and average value). The purpose of the correction function is the energy evaluation on an event by event basis and not on average, thus given a value of reconstructed energy in the PLUG, the correction function must estimate the most probable value of generated energy. In such a case the energy associated with the event after the correction has a higher probability to be the true generated energy of the event.

To estimate correctly the value with the largest probability of occurrence it is necessary to determine the peak positions of the distributions. This is done by fitting the distributions around the peaks using Gaussian functions to minimize the statistical fluctuations from bin to bin in the distributions of the generated energy.

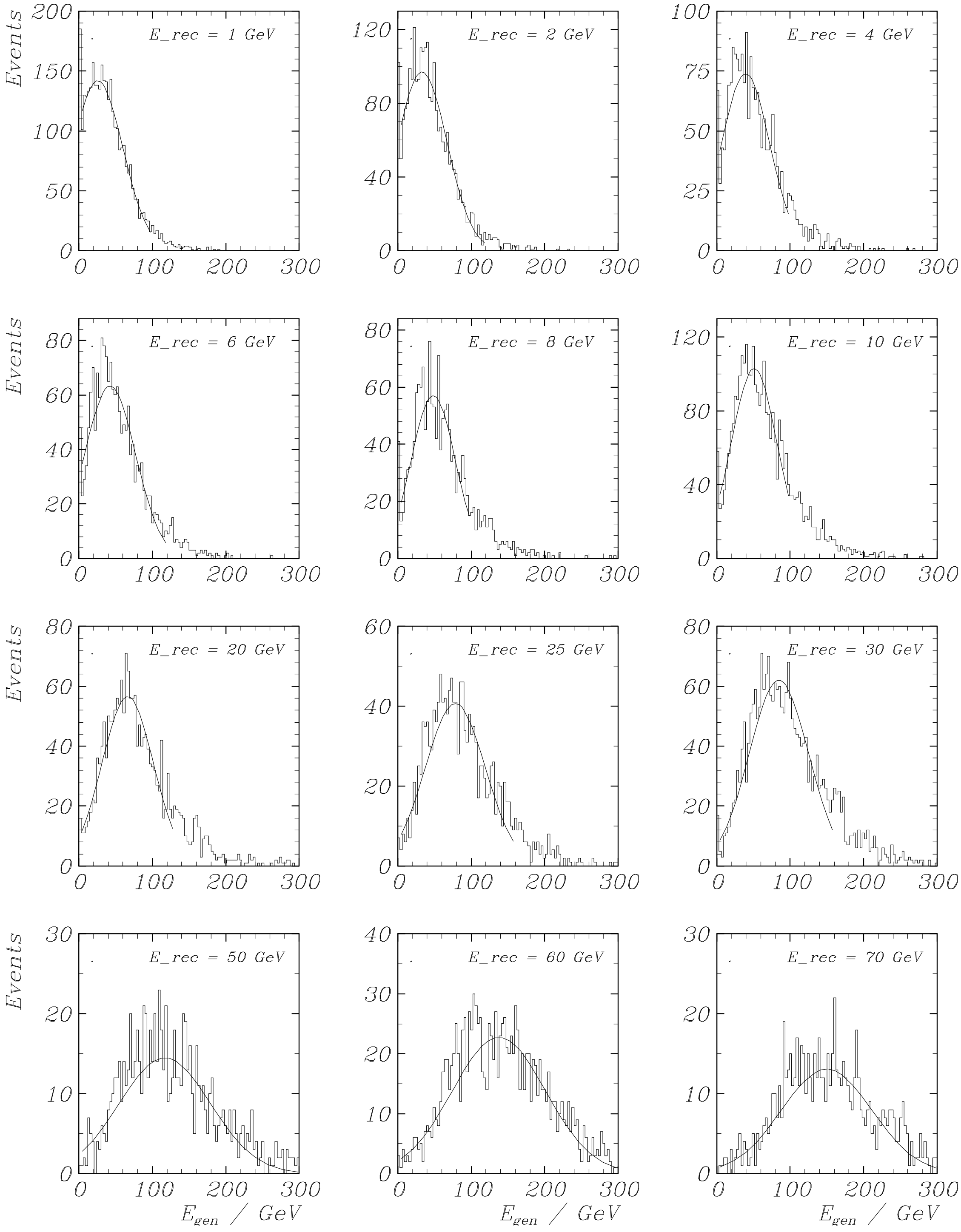

Figure 5.13: *Distributions of the generated energy* E_{gen} *for a given interval around* E_{rec} *and fits to determine the most probable values* $(E_{gen})_{mp}$*. The MC simulation used here was LEPTO6.1 with MEAR option (Ariadne 4.03)*

Int.	$(E^l_{rec};E^u_{rec})$ GeV	Int.	$(E^l_{rec};E^u_{rec})$ GeV
1	(0.5;1.5)	2	(1.5;2.5)
3	(3.5;4.5)	4	(5.5;6.5)
5	(7.5;8.5)	6	(9;11)
7	(14;16)	8	(19;21)
9	(24;26)	10	(28;32)
11	(38;42)	12	(48;52)
13	(55;65)	14	(65;75)
15	(75;95)	16	(95;125)

Table 5.3: *Intervals of reconstructed energy (E_{rec}) used for the production of the generated energy distribution (fig.5.13) ($E^l;E^u$) indicate lower and upper bound of the considered intervals of reconstructed energy in the PLUG.*

This procedure has been repeated using two different QCD-MC models[11] available within the program LEPTO6.1 in the MEPS[12] and MEAR[13] option in order to minimize the physical model dependency of the correction.

The final most probable values plotted in figure 5.14 are obtained averaging over the results of the two MC-models.

The parameterization of the correction function is performed by fitting the obtained numeric relation with the function:

$$f(E_{rec}) = \begin{cases} a_1 + b_1(\frac{E_{rec}}{E_0})^{0.45} + c_1(\frac{E_{rec}}{E_0})^4 & E_{rec} < 18 \text{ GeV} \\ a_2 + b_2\frac{E_{rec}}{E_0} & E_{rec} \geq 18 \text{ GeV} \end{cases} \tag{5.10}$$

and further by imposing the continuity of the first derivative at the point (18 GeV) where the function becomes linear, the following coefficients are obtained:

a_1	=	1.7545	GeV	a_2	=	37.770	GeV
b_1	=	17.567	GeV	b_2	=	1.587	GeV
c_1	=	$7.5318 \cdot 10^{-7}$	GeV	E_0	=	1	GeV

The constant parameter E_0 has been used to normalize the dimension of the variable in the eq. (5.10). The value of the parameter $a_1 = 1.7545$ GeV indicates that even by reconstructing zero energy in the PLUG, there is a sizeable probability that the generated energy is around the non zero value a_1 . This prediction of the used parameterization is consistent with the presence of the inactive material, which can completely absorb low energy particles precluding their detection in the calorimeter.

Thus far the correction function has been calculated by the implicit assumption that the distribution of the inactive material as a function of angle is constant. The achievement of this correction is summarized in fig. 5.15. The correction improves the energy deter-

---

[11] Simulating the DIS processes with Leading Order Matrix Element calculation + parton shower (PS) and color dipole model (CDM).

[12] Matrix Element + Parton Shower.

[13] Matrix Element + Ariadne (CDM).

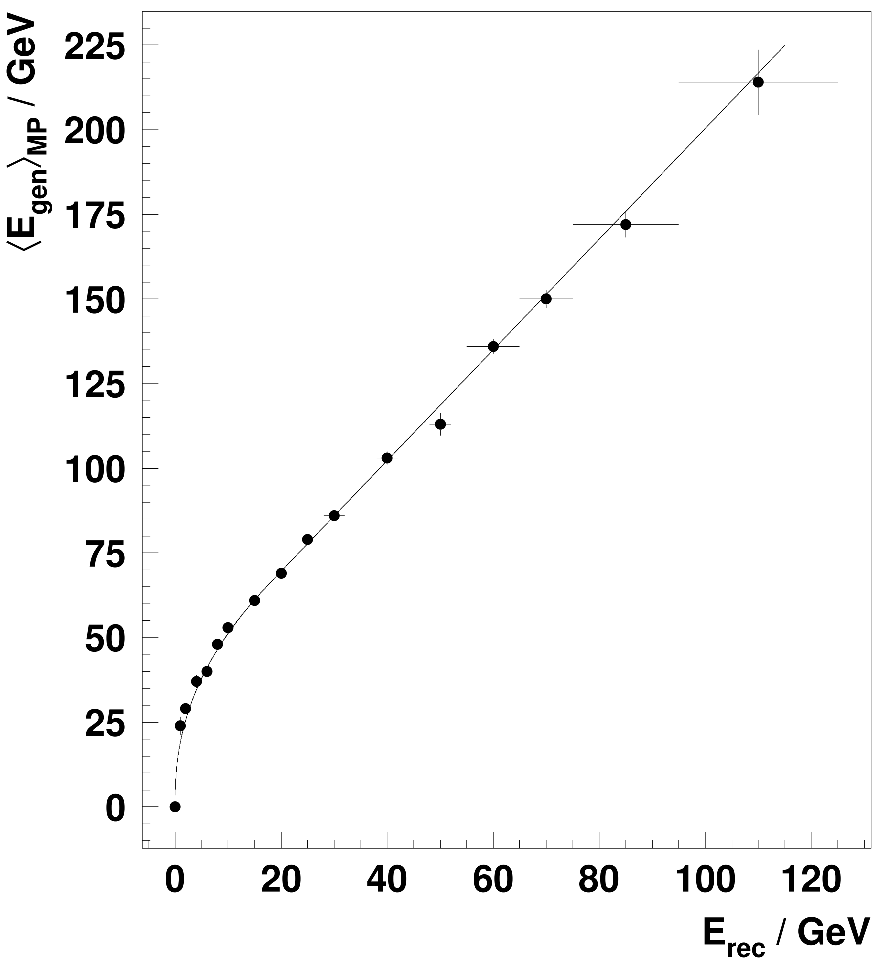

Figure 5.14: *Most probable values of generated energy* $(E_{gen})_{mp}$ *vs.* $\langle E_{rec} \rangle$ *and parameterization curve.*

mination without correction (compare fig.5.15 with 5.12), but it is still not sufficient to describe the distribution of the generated energy (E_{gen}). To improve the energy determination an angular dependence of the correction function is introduced and the obtained results are discussed.

Angular dependent correction function

The inactive material distribution has a strong angular dependence (see fig.5.10). This suggests the possibility to improve the energy determination using further parameters in the correction function which take into account the variation with η (or θ) of the inactive material distribution in front of the PLUG.
A possibility to introduce such parameters in the correction function (5.10) is to multiply

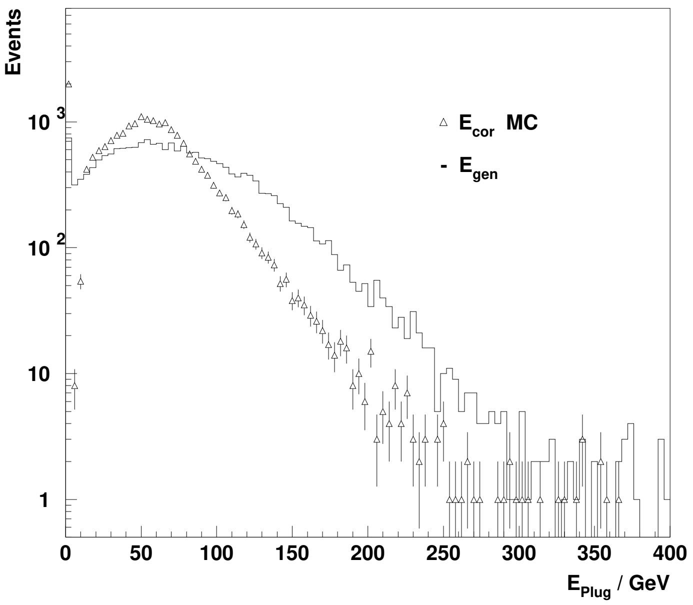

Figure 5.15: *The plot shows the distribution of PLUG energy obtained using only the energy dependent correction function compared to the generated energy in the PLUG acceptance.*

the function with a angular dependent factor. Thus the correction function reads:

$$E_{cor}(E_{rec}, \eta) = f(E_{rec}) \cdot c(\eta) \tag{5.11}$$

where $c(\eta)$ is a factor which depends on the pseudo-rapidity η (or θ) of the calorimeter cell.
As shown in figure 5.10, a reasonable choice to divide the pseudo-rapidity region covered by the PLUG is to consider the three intervals listed in table 5.4. With this choice the (5.11) can be rewritten in a simplified form:

$$E_{cor}(E_{rec}, \eta) = f(E_{rec}) \cdot c_i \tag{5.12}$$

where the index i is related to pseudo rapidity region considered.

PLUG section	η region	inactive material λ
bin 1	$3.5 < \eta \leq 4.0$	~ 4.2
bin 2	$4.0 < \eta \leq 4.5$	~ 2.4
bin 3	$4.5 < \eta \leq 5.1$	~ 1.5

Table 5.4: *Pseudo rapidity intervals used to locate three regions of the PLUG calorimeter and average inactive material amount within the intervals.*

This choice has been made on the following basis:

1. the intervals have almost the same extension in η, this is important because on average a similar particle multiplicity is expected in equally extended rapidity intervals;
2. the amount of inactive material is on average as different as possible between the different intervals. This permits the choice of different parameters for the three regions and therefore a better parameterization of the correction;
3. the smallest angular section of the PLUG (i.e. bin 3) has a radial dimension larger than the innermost PLUG Si-detectors.

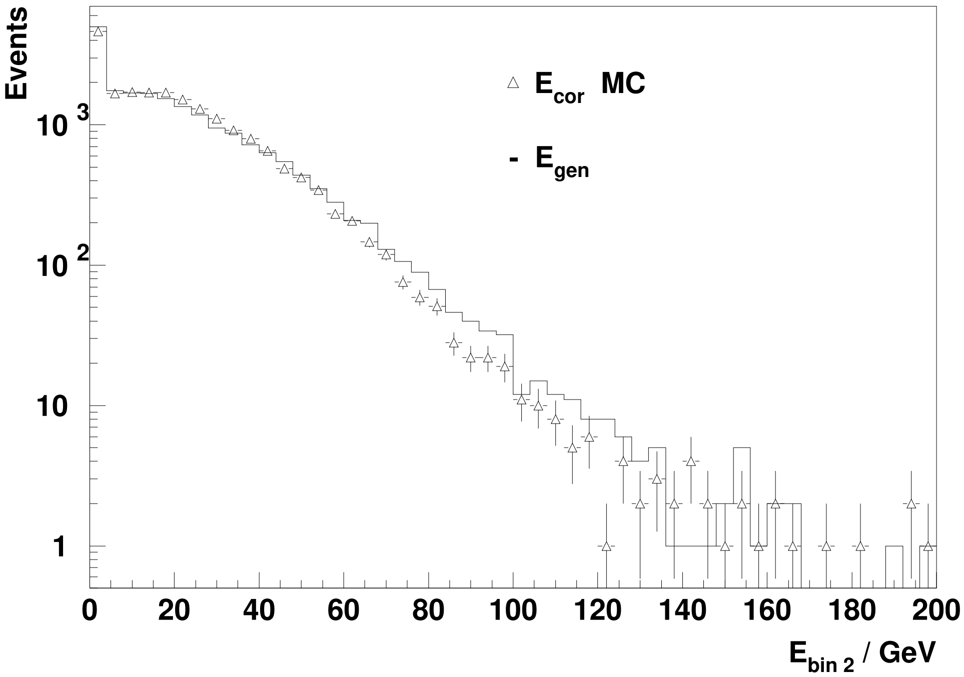

Figure 5.16: *Generated and corrected energy distributions in the pseudo-rapidity bin 2 of the PLUG. The correction function E_{cor} (eq. (5.12))is applied using the parameter $c_2 = 1$.*

In the central interval of the PLUG (bin 2), the average amount of inactive material ($\sim 2.4\lambda$) is approximately equal to the average value over the total PLUG acceptance. This observation is consistent with the results of the energy distribution comparison between corrected and generated energy in the central angular region of the PLUG. Figure 5.16 shows that, if the correction function (5.10) is applied to the reconstructed energy in the region indicated with bin 2 in fig.5.10, the distribution obtained agrees well with the distribution of the energy generated in this region. The agreement obtained in the bin 2 together with the disagreement shown in fig. 5.15 demonstrates that the energy distributions in the regions indicated by bins 1 and 3 are not sufficiently corrected.

In the case of the distributions in bin 1, this can be understood in terms of inactive material since the corrected distribution decreases more steeply with increasing the energy than the distribution of the generated energy. In this region the amount of inactive material is almost two times larger than that in the bin 2 region, as can be observed in fig. 5.10. An improvement of the description of the expected distribution can be obtained by multiplying the correction function (5.10) with a factor $c_1(\eta)$ larger than one. The optimization of this parameter leads to a value $c_1 = 1.3$. Figure 5.17 shows the comparison between corrected and generated energy in this case. The large amount of inactive material decreases the detection efficiency for low energetic particles hampering a better determination of the energy.

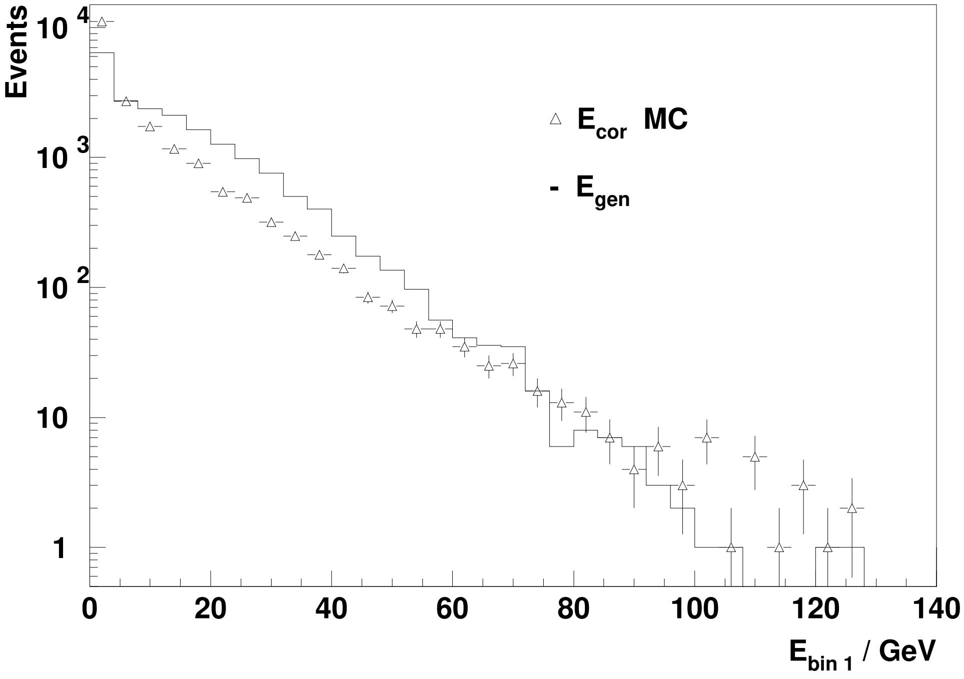

Figure 5.17: *Energy distributions in bin 1 of the PLUG angular acceptance. The correction function E_{cor} (eq. (5.12)) is applied using the parameter* $c_1 = 1.3$.

Another important effect, that can be considered for the improvement of the correction function, is the particle leakage from the calorimeter volume during the shower development. This effect which is due to the limited dimension of the PLUG, is of particular importance in the higher pseudo rapidity region as demonstrated in table 5.5, where the relative volumes of the three considered PLUG sections are given.

The dimensions of the expected hadronic shower in the PLUG are comparable with the dimension of the calorimeter itself. Therefore in pseudo rapidity bin 3 of the PLUG only the core of the shower is sampled and as such a factor $c_3(\eta) > 1$ is expected to provide an improved correction. A further effect in this direction is that, the energy of the emitted particles rises approaching the proton beam. The dimension of the associated particle showers increase and therefore a larger fraction of energy escapes from the calorimeter.

PLUG section	V(bin i) / V(PLUG)
bin 1	$\simeq$ 37 %
bin 2	$\simeq$ 47 %
bin 3	$\simeq$ 16 %

Table 5.5: *Fractions of the total PLUG volume in each pseudo rapidity bin. The bin definition is given in table 5.4 and the graphical representation in fig. 5.10.*

An excellent agreement[14] between the corrected and generated energy distributions in bin 3 is achieved using a factor $c_3(\eta) = 1.5$. This is shown in fig. 5.18. The rather large value of the factor $c_3(\eta)$ is qualitatively justified considering the energy leakage in the beam pipe aperture and beyond the calorimeter.

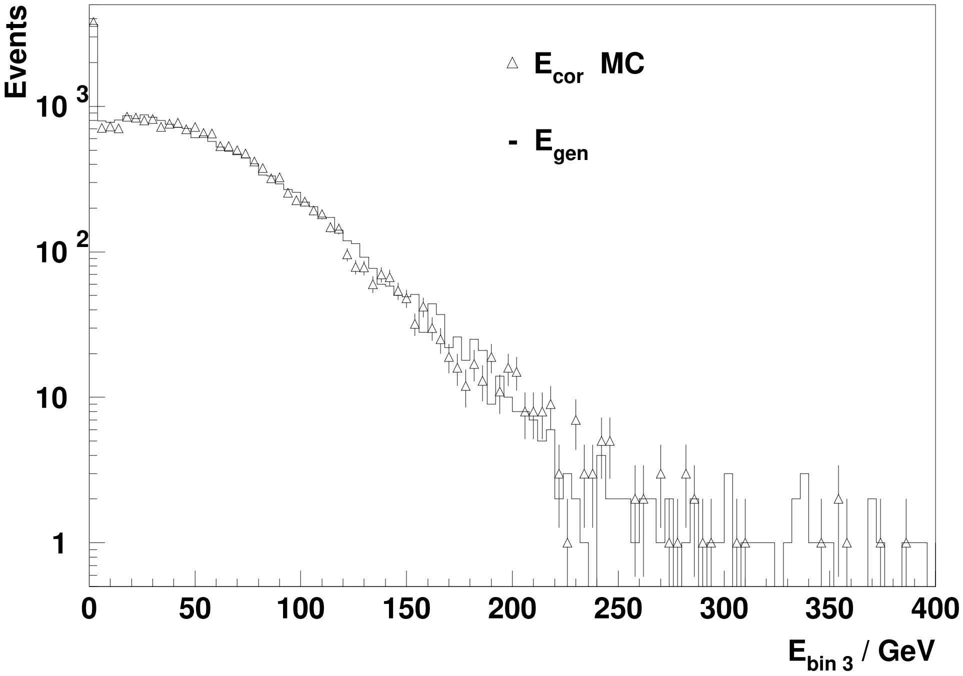

Figure 5.18: *Energy distributions in bin 3 of the PLUG angular acceptance. The correction function E_{cor} (eq. (5.12)) is applied using the parameter $c_3 = 1.5$.*

A significant improvement of the distribution description concerning bin 1 cannot be obtained even by calculating a correction function as those expressed in eq. 5.10 for the sub region called bin 1. The application of this method is hampered by the amount $(4 \div 5\ \lambda)$ of inactive material affecting this region (approximately 2 times larger compared to those in bin 2) which absorbs on average 95% of the energy due to 5 GeV pions as demonstrated

---

[14] The MC-model used for this comparison was LEPTO6.1 with the MEAR option.

by fig.4.1. The limited description of the energy distribution in bin 1 does not largely influence the total energy determination; in fact on average the sum of the three PLUG sections depends to an extent of 85 % on the energies emitted solely in bins 2 and 3, which are themselves very well reproduced.

Figure 5.19 shows the correlation of the corrected energy using the angle dependent correction function versus the generated energy. The corrected and generated energies are on average reasonably correlated. In order to estimate the achieved improvement, the correlation shown here should be compared with correlation shown in fig.5.12.

The modest resolution caused by the presence of the inactive material in front of the calorimeter is evidenced by the large energy fluctuations. In fact for a given value the corrected energy the associated generated energy spans in a wide range. A quantitative evaluation of the energy resolution is performed in the next section.

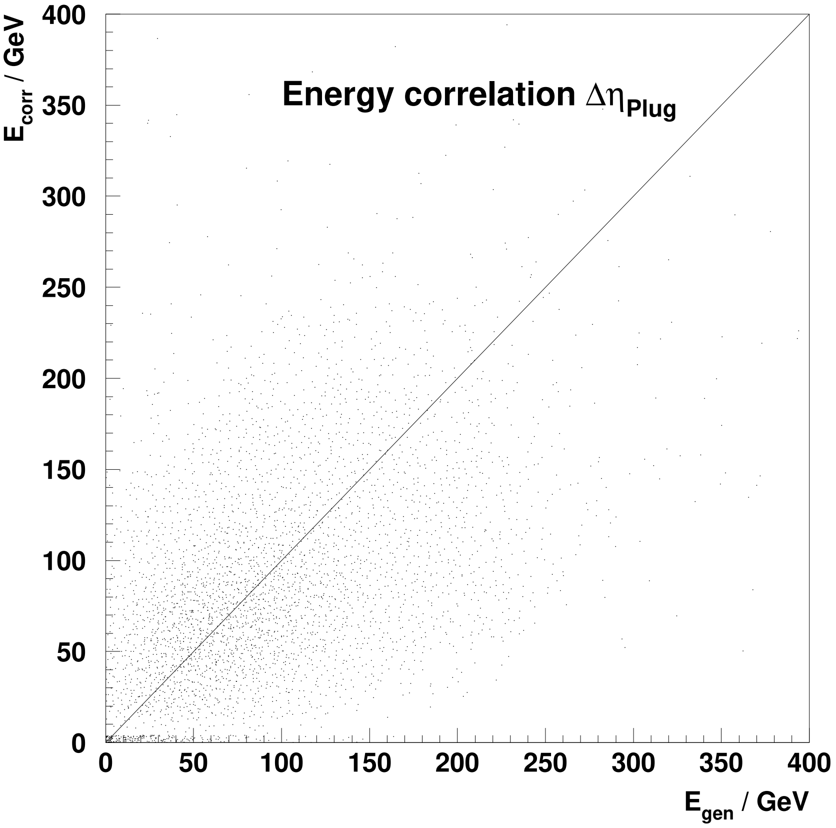

Figure 5.19: *Energy correlation after the angular dependent correction. The corrected energy E_{cor} versus the generated energy E_{gen} is plotted.*

The total PLUG energy distributions are shown in fig.5.20; these concern the energy obtained without correction (E_{rec}), the energy obtained using the angle dependent correction function (E_{cor}) and the distribution of the energy as generated from MC (E_{gen}). The shape of the corrected and generated energy distributions agrees for energy larger than 20 GeV. Below this energy value the correction is limited by the detection inefficiency due to the inactive material. The corrected energy overshoots the generated energy distribution around 80 GeV while around 160 GeV the opposite effect can be observed.

A further general correction described in ch. 6.2 takes into account the small discrepancy

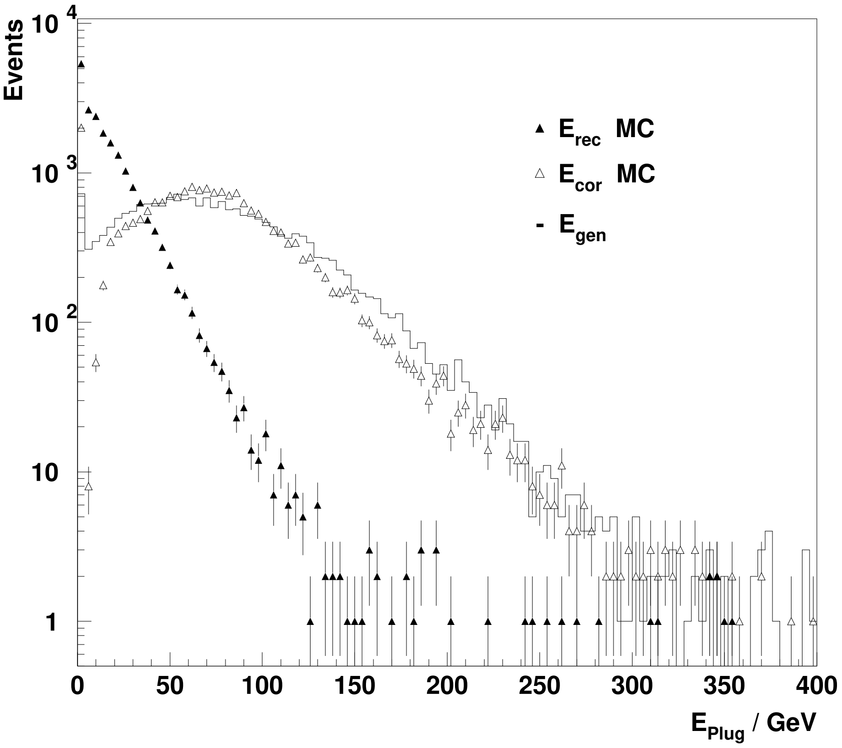

Figure 5.20: *PLUG energy distribution without correction* (E_{rec})*, with correction* (E_{cor}) *and as generated in the PLUG acceptance* (E_{gen})*. For energy larger than 20 GeV the two last two distributions show a reasonable agreement.*

here and permits confident energy measurements.

The dependence of the developed correction on the MC model has been investigated as a function of the energy in order to estimate the systematic error on energy determination. The ratio bin by bin, generated over corrected energy for each of the three pseudo rapidity bins and for the full PLUG coverage has been built for two MC models[15]. This is shown in figure 5.21. The systematic variation of the bin by bin correction is on average over the energy spectrum within 10 %. Larger differences can be observed for total PLUG energy E_{PLUG} larger than 160 GeV. However the fraction of events with a generated energy in the PLUG acceptance larger than 160 is lower than 5 %.

In conclusion, even with the large amount of inactive material in front of the PLUG, the possibility to perform energy determination of particles emitted in the pseudo rapidity region $3.5 < \eta < 5.1$ has been demonstrated. The energy correlation (fig. 5.19) demonstrates the feasibility of the energy correction on an event by event basis. The reconstruction of the PLUG energy distribution for energies larger than 20 GeV is obtained and for the PLUG sub-regions bin 2 and 3 the corrected and the generated energy distributions are in good agreement over the full energy spectrum.

---

[15] LEPTO65 / ARIADNE4.03

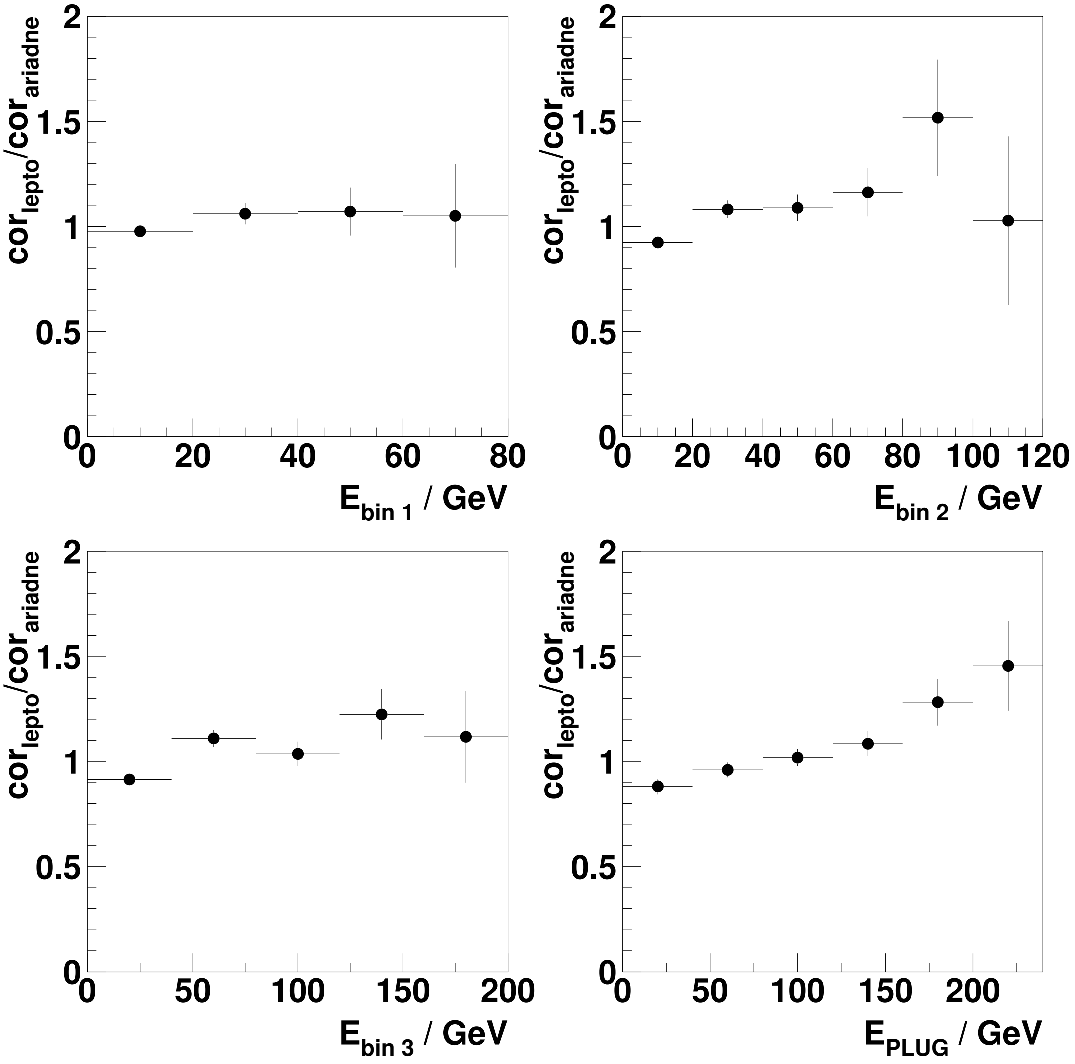

Figure 5.21: *Ratio of the corrections bin by bin* $cor_{lepto}/cor_{ariadne}$ *for the three sub pseudo-rapidity PLUG regions and for the their sum.*

5.6 Energy resolution in the experiment

In this section the energy resolution of the PLUG calorimeter within the H1 experimental environment is investigated. In a typical *ep* DIS event the color connection between the proton remnant and the scattered parton produces through the fragmentation (see ch. 2.4) several particles (hadrons) with differing energies. The expected multiplicity distribution of particles emitted into the PLUG angular acceptance is show in fig. 5.22 in the case of the three different MC models considered previously in ch. 5.2. The multiplicity

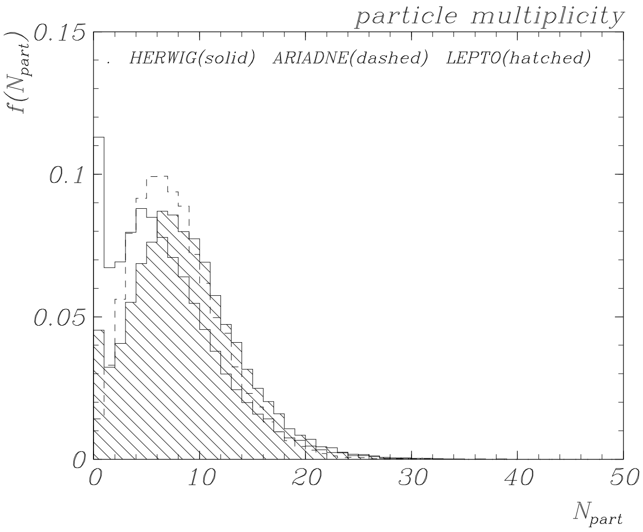

Figure 5.22: *Multiplicity distribution generated in the PLUG angular acceptance.*

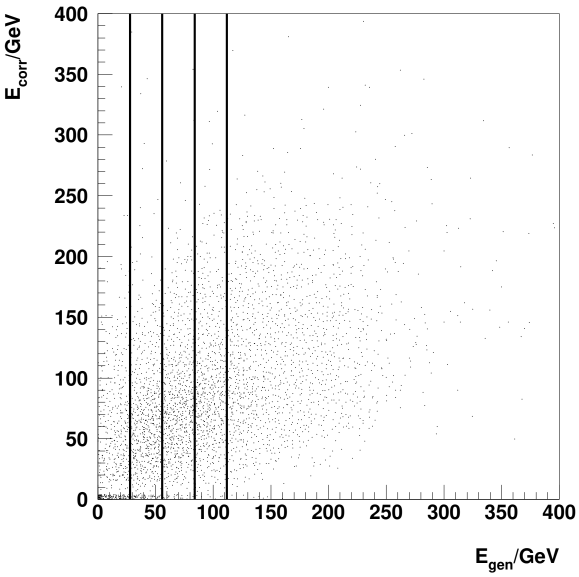

Figure 5.23: *Energy correlation plot. The events within the vertical slices have been used to produce the distribution of the corrected energy in fig.5.24.*

of particles with an energy larger than a few GeV reaching the calorimeter is about 5 per event and the resulting hadronic showers cannot be spatially separated from each other. This is intrinsically impossible, when the shower dimension is on average larger than the distance between two primary particles hitting the PLUG so that the two originating showers overlap for more than 50% of their volume. Under these conditions it is convenient to investigate the energy resolution of the calorimeter for the expected particle flow per event. This has been done using a sample of simulated data containing events with a squared momentum transferred, within the range $5 < Q^2 < 100$ GeV^2. The evaluation of the effective energy resolution of the PLUG is presented here for event energies from a few to more than 100 GeV. The events used for the resolution evaluation can be represented in a correlation plot similar to that shown in fig. 5.19, but containing more events.
Figure 5.23 shows such a plot where 4 intervals of generated energy have been indicated with vertical bars. By selecting the events within one of the four chosen intervals, it is possible to produce the distributions of corrected energy shown in fig.5.24. The determination of the width of the distribution and of the averaged value of generated energy in the considered interval, permits the calculation of the PLUG resolution in H1 for these simulated events. The obtained resolution results are indicated in fig. 5.25. For generated energies below 30 GeV the resolution does not permit energy determination on an event by event basis. This results from the poor detection efficiency for low energetic particles due to the presence of the inactive material and the concomitant increase of the fluctuation of the calorimeter response. For event energies larger than 30 GeV the resolution improves and its value reaches 35% for event energies around 100 GeV. Events of generated energy larger than 112 GeV have been not considered in the energy resolution plot. The reason is the large energy leakage from the calorimeter with the subsequent saturation effect in the calorimeter response due to the dimension of the showers associated with the event. The response saturation effect for events with a generated energy between $112 < E_{gen} < 280$ GeV is summarized in table 5.6. In the last column of the same table the fraction of events F generated with an energy $E_{gen} > \langle E_{gen} \rangle$ is given. F gives an estimate of the contribution to the energy flow due to the events with $E_{gen} > \langle E_{gen} \rangle_I$ where I indicates the energy interval on which the average $\langle E_{gen} \rangle_I$ have been calculated.

I(E_{gen})	$\langle E_{gen} \rangle_I \pm RMS$ GeV	$\langle E_{cor} \rangle_I \pm RMS$ GeV	$\langle E_{cor} \rangle_I / \langle E_{gen} \rangle_I$ %	F %
(112,140)	125 ± 7.9	96.5 ± 42.8	77	13.9
(140,168)	152.4 ± 7.9	107.5 ± 45.5	71	5.7
(168,196)	179.6 ± 7.6	118.6 ± 47.2	66	2.6
(196,224)	207.9 ± 7.7	127.7 ± 53.8	61	1.2
(224,252)	235 ± 7.5	143.3 ± 65.1	61	0.6
(252,280)	263.7 ± 7.8	162.3 ± 65.7	61	0.3

Table 5.6: *The first column contains the interval definitions of generated energy in the PLUG acceptance (I(E_{gen})), the second the averaged generated energy $\langle E_{gen} \rangle_I$ with its root mean squared (RMS), the third the averaged corrected energy $\langle E_{cor} \rangle_I$ and its RMS as a measurement of the fluctuation; the fourth is the signal saturation of the calorimeter response and the fifth the fraction F of events with $E_{gen} > \langle E_{gen} \rangle_I$.*

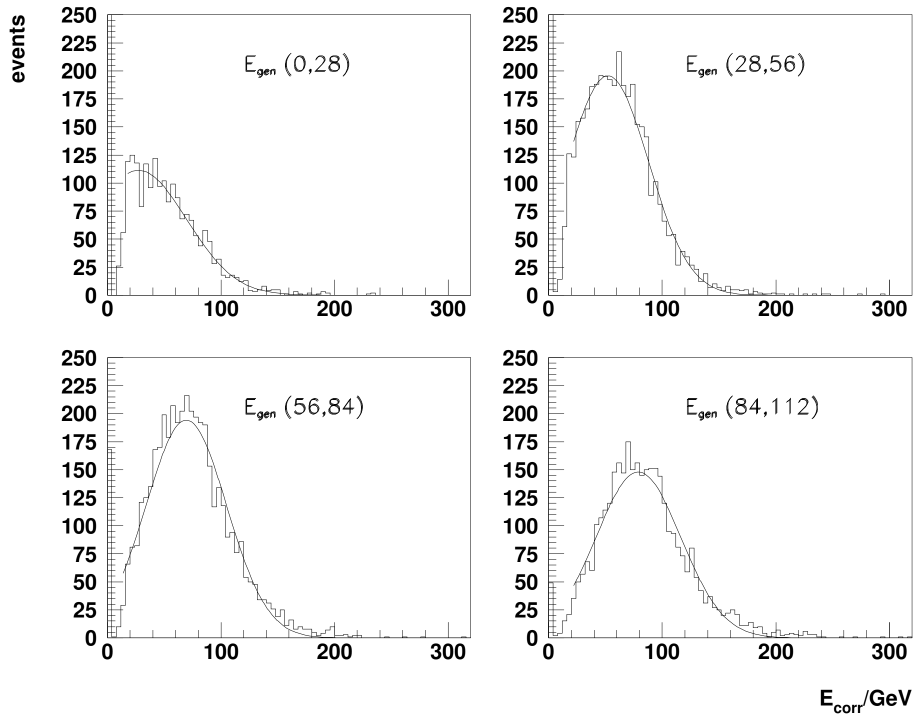

Figure 5.24: *Distributions of the corrected energy for different intervals of generated energy* E_{gen} *shown in the plots. The curves are obtained performing Gaussian fits and avoiding the regions of low corrected energy where the detector is limited in efficiency.*

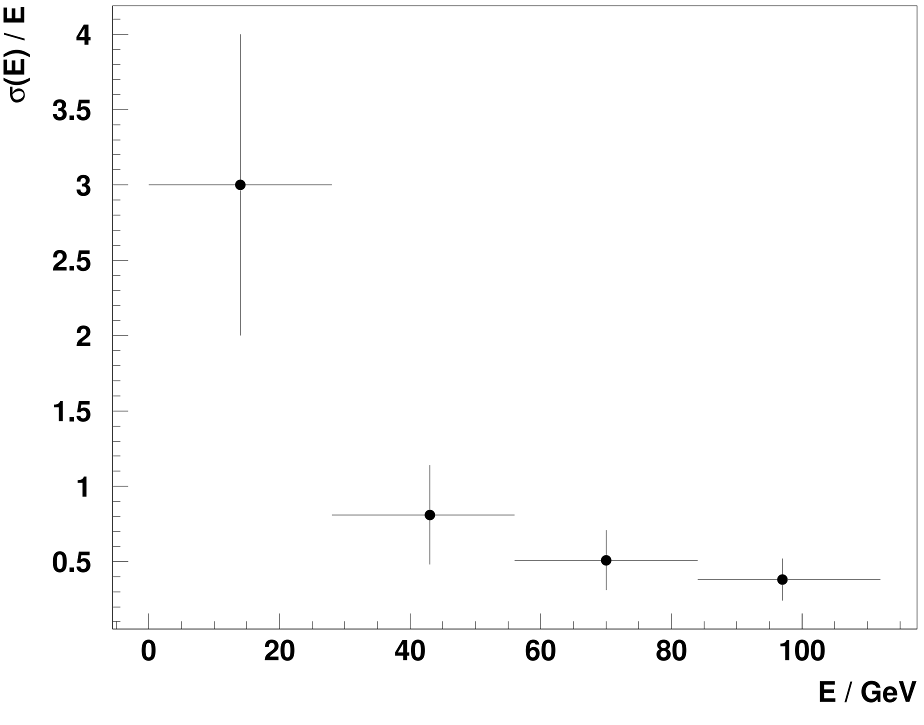

Figure 5.25: *PLUG Energy resolution in the H1 experiment as obtained from simulated data.*

5.7 Plug energy distributions for real data

In order to demonstrate the feasibility to correct real data, the distributions of the energy in the PLUG, before and after the correction, are shown and compared with MC simulations. The events used are selected according to the criteria discussed in the ch. 6.1 and are in a region of the phase space $(x; Q^2)$ bounded such that $5 < Q^2 < 100$ GeV^2 and $10^{-4} < x < 10^{-2}$. Figure 5.26 shows the data-MC comparison at the reconstruction level (i.e. without correction). The distribution of the reconstructed energy in the PLUG (i.e. before the correction) is well described using different MC simulation models. In particular good agreement between data and simulated distribution is achieved using the model implemented in Ariadne (fig. 5.26). Under these condition it is expected that the correction developed using this simulation will produce reliable results for real data.

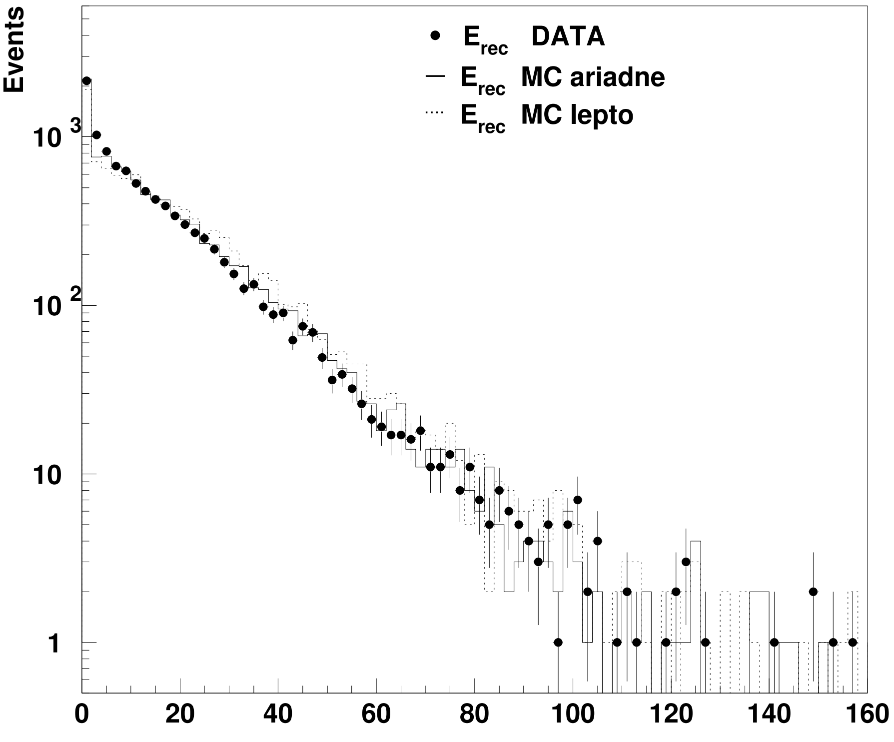

Figure 5.26: *PLUG total energy distributions before correction E_{rec}. Data and two MC-model are compared (the MC-model being Ariadne4.03 and Lepto6.1 MEPS).*

Figure 5.27 shows the total PLUG-energy distribution after the correction and the distributions of the generated energy for two models. The corrected energy distributions for data in the three pseudo rapidity regions of the PLUG are shown in fig. 5.28. The generated energy obtained using the two MC models are superimposed on the same plots. The energy distributions from data are well described by the models in pseudo rapidity bins 1 and 2 for energies larger than 50 GeV. The better description of the data distribution in bin 3 is achieved for energies below 80 GeV. Finally two further control plots

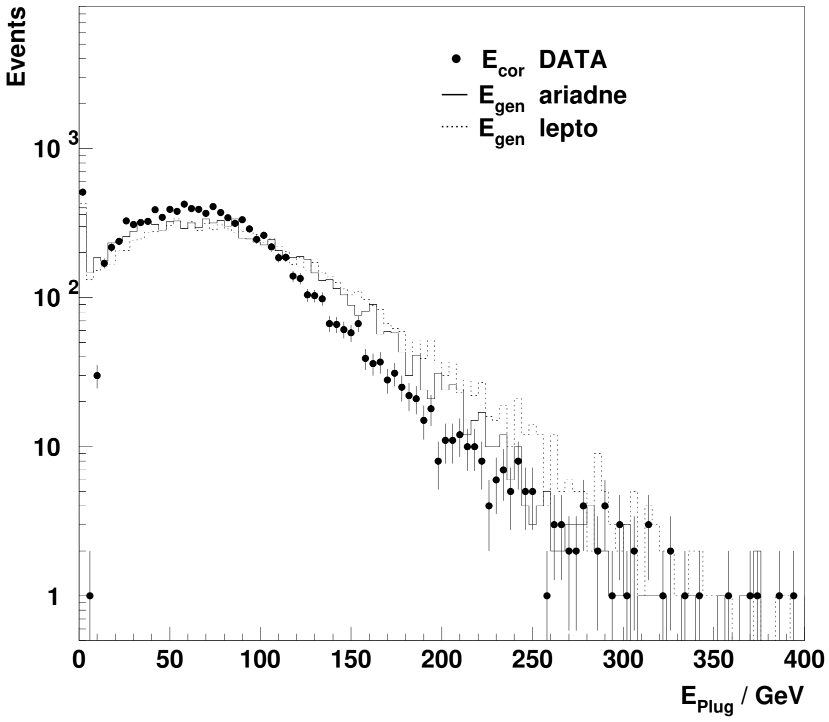

Figure 5.27: *Total energy distribution after correction E_{cor} compared to generated energy distributions E_{gen}.*

confirm the reliability of the correction function. The first in fig.5.29 shows the averaged energy per event as a function of the longitudinal section of the calorimeter. This is an averaged measurement of the event shower development in the PLUG. The longitudinal development of the energy deposition is similar for data and MC, the slope is steeper for the data points. In the last layer there is an enhancement of the signal in the data which is not observed in the simulations. This effect can be interpreted as the detection of back scattered particles generated by the interaction of the proton beam with the C3 collimator placed beyond the PLUG. A similar effect due to back scattering particles is also observed in the H1 tail catcher [82].

The second control plot (fig. 5.30) shows the data and MC comparison of the averaged corrected energy per event as a function of the pseudo rapidity. The data and the models substantially agree; the largest discrepancy being in the extreme pseudo rapidity bin where higher energy flows are expected.

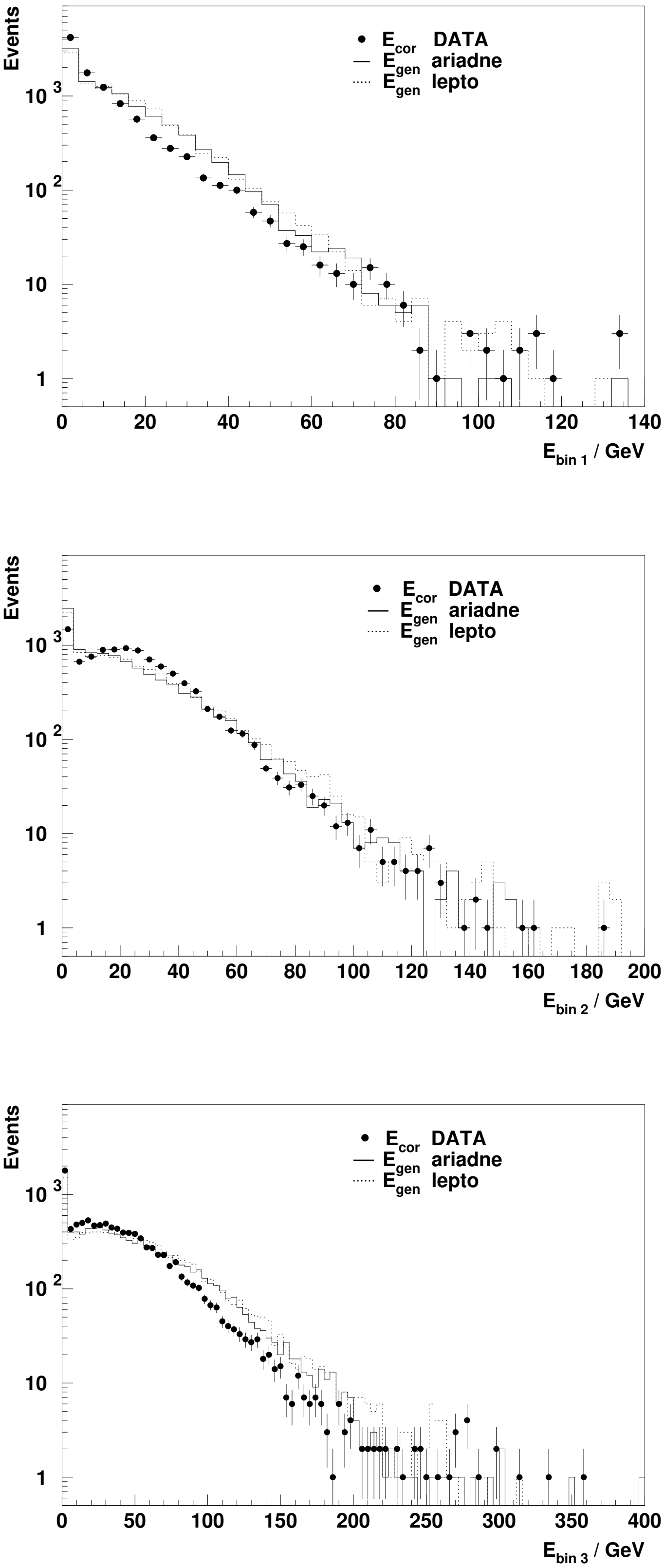

Figure 5.28: *The energy distributions in the three pseudo rapidity regions of the PLUG are shown. Corrected data* E_{cor} *are compared with generated energy distributions from MC models* E_{gen} *.*

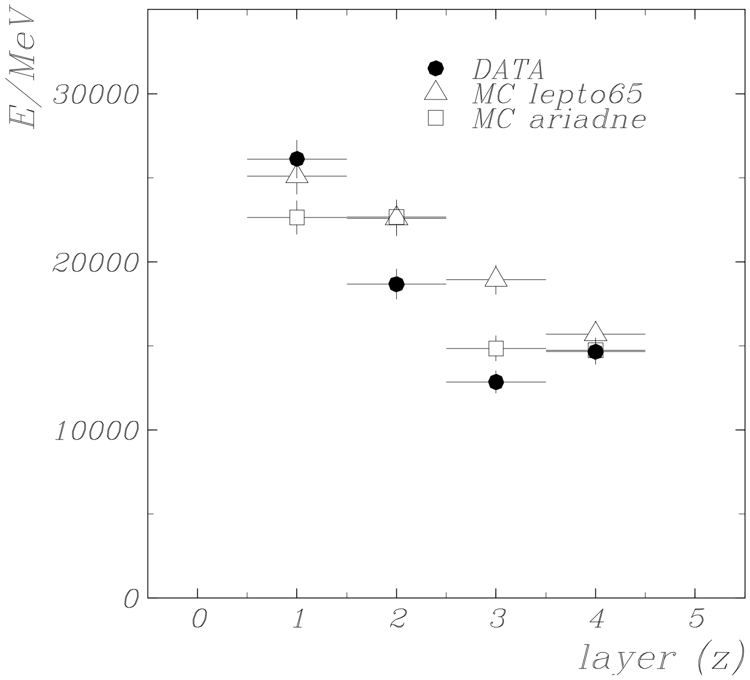

Figure 5.29: *Energy deposition in the 4 layers of the Plug after inactive material correction.*

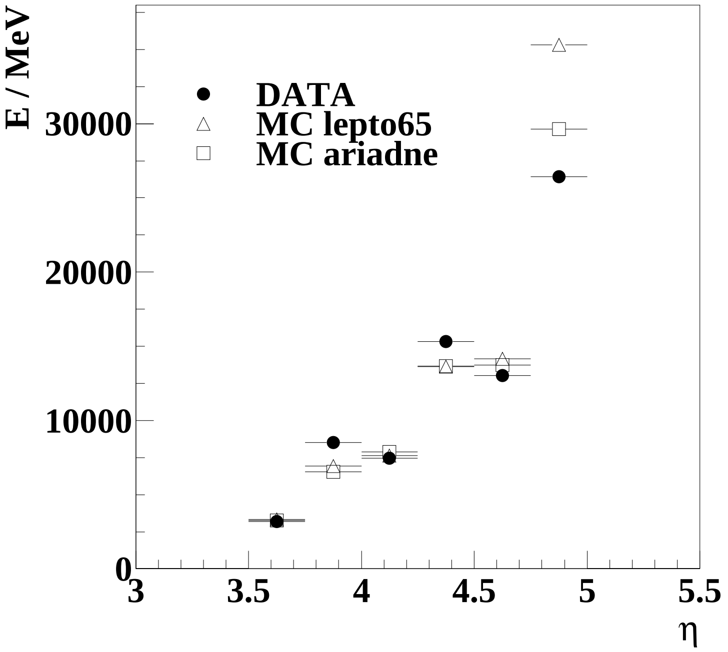

Figure 5.30: *Averaged corrected energy per event as a function of pseudo rapidity.*

5.8 Test of the correction function using data

As pointed out into the introduction in order to perform measurements on the widest phase space region, the electron-proton interaction point has been shifted for a limited period of the 1994 luminosity run. The shifted vertex data offer the possibility to verify the stability of the energy correction with the change in the PLUG acceptance determined by the shift of the interaction point. This test based on real data is independent of MC simulations.

Two samples of events with different z coordinates of the interaction point have been considered. The first sample, called A, is a data subset with nominal vertex position. The selected events have negative z coordinate of the interaction point ($z_A < 0$ cm) in order to maximize the change of PLUG acceptance with respect to the second sample, called B. The resulting averaged interaction point of the events in the sample A is:

$$\langle z_A \rangle \; = \; -6.0 \pm 0.1 \text{ cm}$$

The sample B is a part of the shifted vertex data with averaged interaction point:

$$\langle z_B \rangle \; = \; 67.7 \pm 0.3 \text{ cm}$$

The events of the sample A are selected according the criteria specified in ch. 6.1 for the nominal vertex sample, with the further requirements to have x and Q^2 within the intervals:

$$4 \cdot 10^{-4} < x < 2 \cdot 10^{-3} \qquad \text{and} \qquad 8 < Q^2 < 20 \text{ GeV}^2$$

The sample B contains shifted vertex events selected as described in ch.6.1 but additionally having x and Q^2 within the intervals

$$10^{-4} < x < 3 \cdot 10^{-3} \qquad \text{and} \qquad 10 < Q^2 < 20 \text{ GeV}^2$$

With this choice of the conditions on the kinematic variables the samples A and B have similar average values of x and Q^2:

$$\langle x_A \rangle = (8.9 \pm 0.1) \cdot 10^{-4} \qquad\qquad \langle Q^2_A \rangle = 14.4 \pm 0.1 \text{ GeV}^2$$

$$\langle x_B \rangle = (8.7 \pm 0.1) \cdot 10^{-4} \qquad\qquad \langle Q^2_B \rangle = 13.9 \pm 0.1 \text{ GeV}^2$$

thus the two samples are almost equivalent in respect of the event kinematics and expected energy flow.

The two experimental conditions, schematically illustrated in fig.5.31, realize two different inactive material configurations in front of the PLUG. The displacement in the forward direction of the interaction point produces a decrease of the forward acceptance of the detector.

Figure 5.32 shows the inactive material distribution with the central section of the PLUG called bin 2_A and 2_B respectively (for the samples A and B) indicated. The pseudo-rapidity decrease of $\Delta\eta = 0.2$ corresponds to a large increase ($\sim$ 50%) of the inactive material amount in front of the central region of the PLUG (bin 2). Therefore the

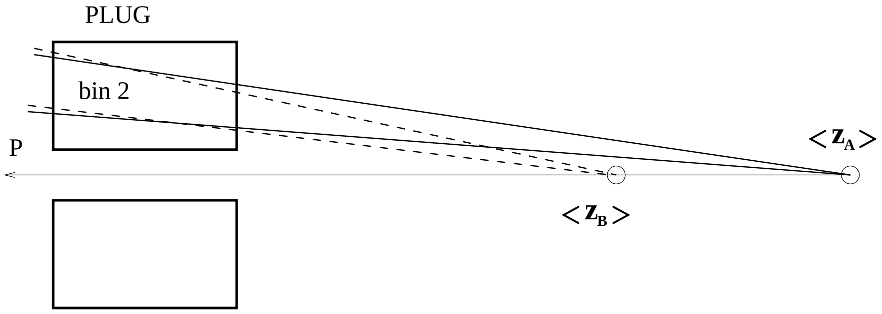

Figure 5.31: *The consequence of the vertex displacement on the Plug acceptance in a schematic representation.*

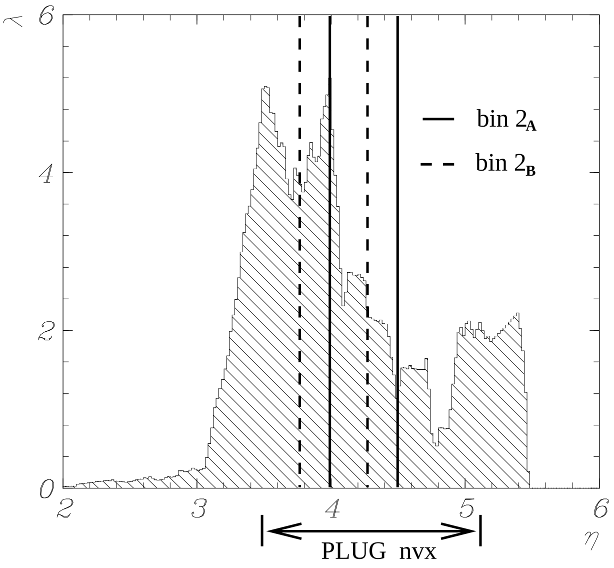

Figure 5.32: *Inactive material distribution with the pseudo rapidity bin 2_A and 2_B superimposed upon it.*

reconstructed energy per event in this region of the PLUG using the sample B is expected to be lower than that obtained using the sample A. The comparison of the reconstructed energy distribution using the two samples is shown in fig. 5.33. The relative decrease of the averaged reconstructed energy is of 22 % and also depends on the averaged rapidity of bins 2_A and 2_B (see later).
The distributions of the energy in the central region of the PLUG after the correction are presented in fig. 5.34. As expected the correction function for the sample B introduces larger correction on average due to the inactive material increase. The averaged correction factors for the two samples can be evaluated considering the ratios of the averaged corrected energy over the averaged reconstructed energy:

$$C_A = \langle E_{cor} \rangle / \langle E_{rec} \rangle \cong 3.22$$

$$C_B = \langle E_{cor} \rangle / \langle E_{rec} \rangle \cong 3.68$$

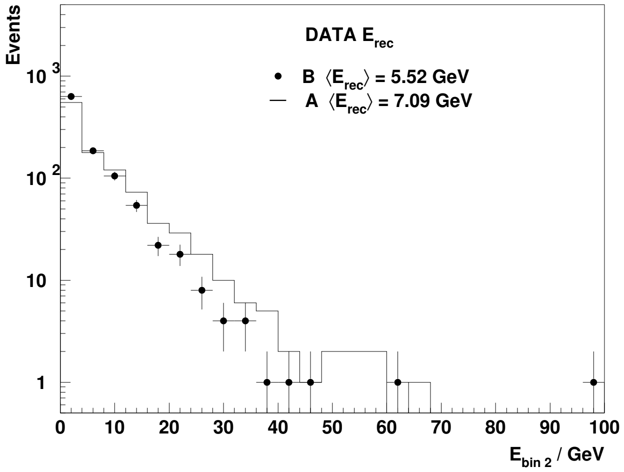

Figure 5.33: *Distributions of the reconstructed energy in the central pseudo rapidity bin of the PLUG.*

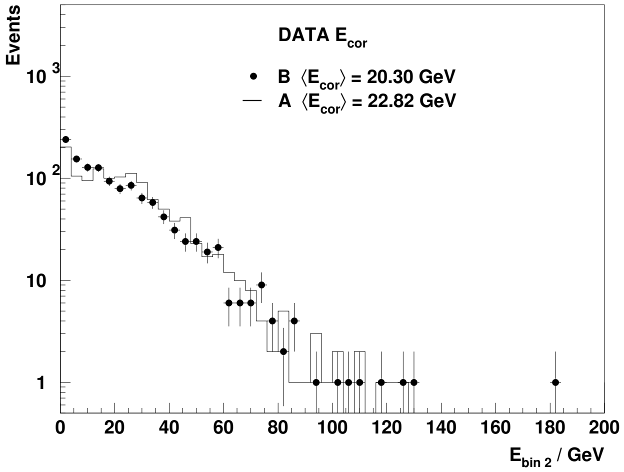

Figure 5.34: *Distributions of the corrected energy in the central pseudo rapidity bin of the PLUG.*

Since $C_B > C_A$ the increase of the inactive material which affects the energy determination on the sample B, is correctly taken into account by the correction function.
The relative difference of the averaged corrected energy is:

$$\frac{\Delta\langle E_{cor}\rangle}{\langle E_{cor}\rangle} = \frac{\langle E_{cor}\rangle_A - \langle E_{cor}\rangle_B}{\langle E_{cor}\rangle_A} \simeq 0.11 \tag{5.13}$$

where, $\langle E_{cor}\rangle_A > \langle E_{cor}\rangle_B$.

It is possible now, using MC generators, to estimate how changes the averaged energy per event in the two pseudo-rapidity intervals called bin 2_A and 2_B having same extension,

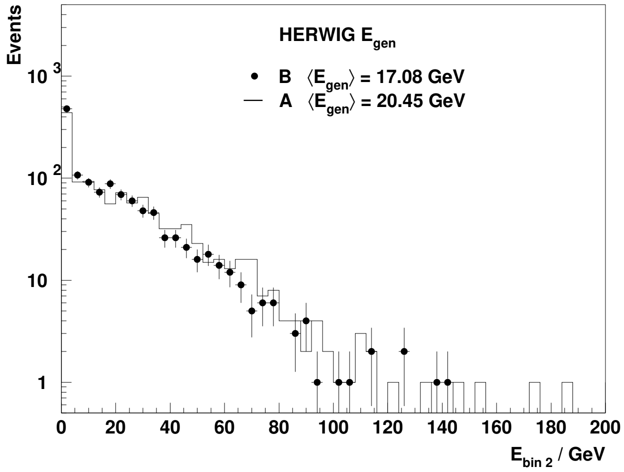

Figure 5.35: *Distributions of the MC generated energy in the central pseudo rapidity bin of the PLUG.*

but shifted from each other by $\Delta\eta = 0.2$ pseudo-rapidity units. The comparison of the relative variation of averaged energy expressed in eq. (5.13) for the corrected data with that expected from MC generator allows one to verify the precision of the correction.
Figure 5.35 shows the distributions of the energy per event emitted within bin 2_A and bin 2_B using the Herwig MC generator. The relative variation of averaged generated energy due to the pseudo rapidity shift is:

$$\frac{\Delta\langle E_{gen}\rangle}{\langle E_{gen}\rangle} = \frac{\langle E_{gen}\rangle_A - \langle E_{gen}\rangle_B}{\langle E_{gen}\rangle_A} \simeq 0.14 \qquad (5.14)$$

using Herwig and 16 % using Ariadne [16]. By comparing the variations expressed in eq. (5.13) and (5.14) it is possible to conclude that assuming the correction function is correct for bin 2_A there is on the energy determination in bin 2_B a maximal overcorrection of $\sim 5\%$ if the Ariadne result is considered (or $\sim 3\%$ using Herwig).
This is an excellent result if the magnitude of the correction given by C_A is considered. The 5 % represents an estimate, for the bin 2 region, of the systematic error due to the inactive material correction determination that is used in ch. 6.5 in the total evaluation of the systematic error.

---

[16] Herwig and Ariadne are the MC models that show the biggest defference with each other

Chapter 6

Physics analysis using the PLUG

In the previous chapter, the feasibility of performing energy measurements using the PLUG calorimeter has been investigated. In particular the energy resolution and the linearity of the response achieved on the energy measurement of particles emitted within the PLUG angular region has been presented for a wide range of energies.

In this chapter measurements of the transverse energy flow as a function of the pseudo rapidity obtained within the H1 experiment are presented. The measurements are performed in the laboratory and in the center of mass systems. Particular emphasis is given to the pseudo rapidity region covered by the PLUG calorimeter.

The measurements concern deep inelastic scattering events with a squared transfered momentum $Q^2 < 100$ GeV^2 recorded during the 1994 HERA luminosity run period.

The data analysis is performed by dividing the phase space into several regions and measuring the transverse energy flow for each region (i.e. a bin in phase space). This permits the determination of the evolution of the measured quantities as a function of two considered kinematic variables.

The kinematic variables x and Q^2 are used to define the phase space of the events produced in the ep scattering.

A useful representation of the events investigated in this analysis is obtained considering the kinematic plane (defined by x and Q^2) in which each point represent one event. Figure 6.1 shows how the events populate the phase space after the event selection. The requirements which define the data selection are discussed in the next section.

The selected events belong to two different data sets: the first in which the interaction region was around the nominal interaction point[1], called the nominal vertex sample (NVX), and the second, called the shifted vertex sample (SVX), was obtained by shifting the interaction position in the forward direction along the z-axis[2].

The forward shift of the z-coordinate of the interaction point produces a shift in acceptance of the H1 detector. The small reduction ($\sim 0.12^o$ degree) of the forward acceptance corresponds an extension from $\theta_{\rm NVX} = 173^o$ to $\theta_{\rm SVX} = 176$ of the backward acceptance

---

[1] The nominal value was $z_{nominal} = 5$ cm.

[2] The nominal value for the SVX data sample was $z_{shift} = 67$ cm.

with the detection of scattered particles to larger values of polar angle θ. A desired consequence is an enhancement of the accessible phase space to lower values of x and Q^2 for the physics analysis using the data of the SVX sample as can be seen from figure 6.1.

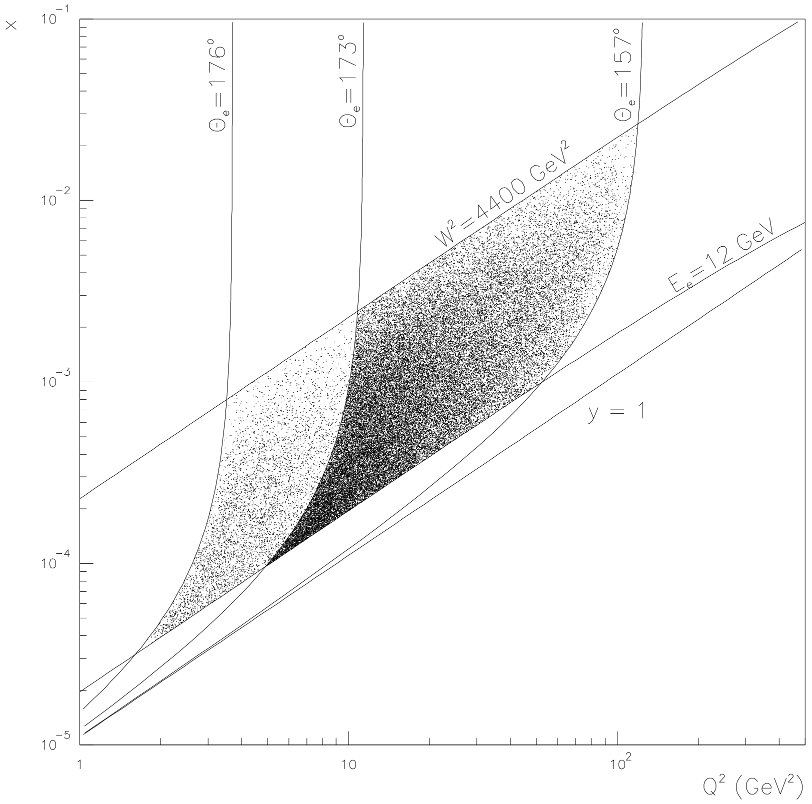

Figure 6.1: *Selected events and cuts in the kinematic plane* $(x; Q^2)$ *(see ch. 6.1).* θ_e *is the polar angle individuating the direction of the scattered electron. The curves* $\theta_e = 157^o$ *and* $\theta_e = 176^o$ *indicate the achieved acceptance using both data samples.* $\theta_e = 173^o$ *gives the max. acceptance for the NVX sample.*

6.1 Event selection

The events for the analysis carried out in this work constitute a subset of the total amount of data collected during the luminosity run period 1994.
The selected events pass through the trigger Levels 1 and 4 (see ch. 3.3) of the data acquisition and the Level 5 in which the information from all sub-detectors is completely reconstructed. After this first selection procedure the data are classified according to physics classes [3].

---

[3] The class of event used as starting point of the selection is called class 11 its definition is given in [84]

The acquired runs[4] considered in the data selection fulfill the condition to have almost every main detector operational; they are classified to have either a *good* or a *medium* quality according the criteria assumed in the H1EP[5] data base for the run classification of the 1994 Luminosity period.
In general an ideal selection would contain all events representing the analyzed physics processes. At the same the selection should not include events produced by undesired processes which represent background on the measurements. This ideal situation is however not realizable using the full detector acceptance. In order to define a sample with almost ideal characteristics and which is well represented by simulated events, range of values of physical variables, reconstructed quantities and of the event kinematics must be used. These variable ranges or selection criteria, which define the measurement acceptance, are based on the precision and reliability of the measurement of the same variables. The precision and reliability determination are obtained from MC simulations of events and detector. Simulations have also to be used to correct the measurements for detector effects. As introduced in ch. 2.4 and 5.4 a correct interpretation of the events is possible when the simulation of the known physics processes and of the detector response to the same events is well established. This means that the distributions of the main physics observables of experimental data are reproduced to a satisfactory extent.
The analysis in this chapter is performed using the following H1 sub-detectors described in ch. 3.2 and 4 and grouped as follows:

1. the Time of Flight (ToF) and the veto-wall system;
2. the central jet chambers used in this analysis for the reconstruction of the interaction point (vertex of the event)
3. the Backward Electro-magnetic Calorimeter (BEMC) and the Backward Proportional Chamber (BPC), used for the scattered electron identification and the measurement of its energy and position;
4. the Liquid Argon and the PLUG calorimeter for the measurement of energy and position of the particles associated to the hadronic system X.

The selection criteria (cuts) used to define the data sample have been developed within the "flow and spectra" physics working group of the H1 collaboration. The same have been used in a similar way in previous analysises of the hadronic final states [90, 92, 93, 83]. These cuts are explained below.
The distributions shown in the following concern data and MC samples after the cuts discussed in this section.

---

[4] The run is a small unit of acquired data. Typically a run contains a number of the order of 10^4 events. In every run, parameters of the detector, trigger or electronics can be re-adjusted.

[5] The run classification *good* means that all major systems are operational (major systems are: JC1-2, LAr, Muons, BPC, Lumi, BEMC, MWPC, FTplanar). *Medium* means that one or more major systems are out of operation or several minor systems out of operation (minor systems are: FwMuons, COZ, CIZ, FPS, CST, PLUG, BST, FTradial, FNC, RZ-trigger, DCRPhi-trigger, z-vrtx-trigger, FwMuon-trigger).

- The high rate background originated upstream of the main detectors from beam-gas and beam-wall interaction events is rejected using the veto signals from the ToF and veto Wall systems.
  A further condition to suppress background events is the bound on the z-coordinate of the vertex in a coordinate window defined by $|z_{vertex} - \overline{z}| < 30$ cm.
  The distributions of the vertex z-coordinate for data and MC is shown in fig. 6.2 for the NVX and SVX samples. Both data distribution of the reconstructed interaction points are Gaussian as expected.

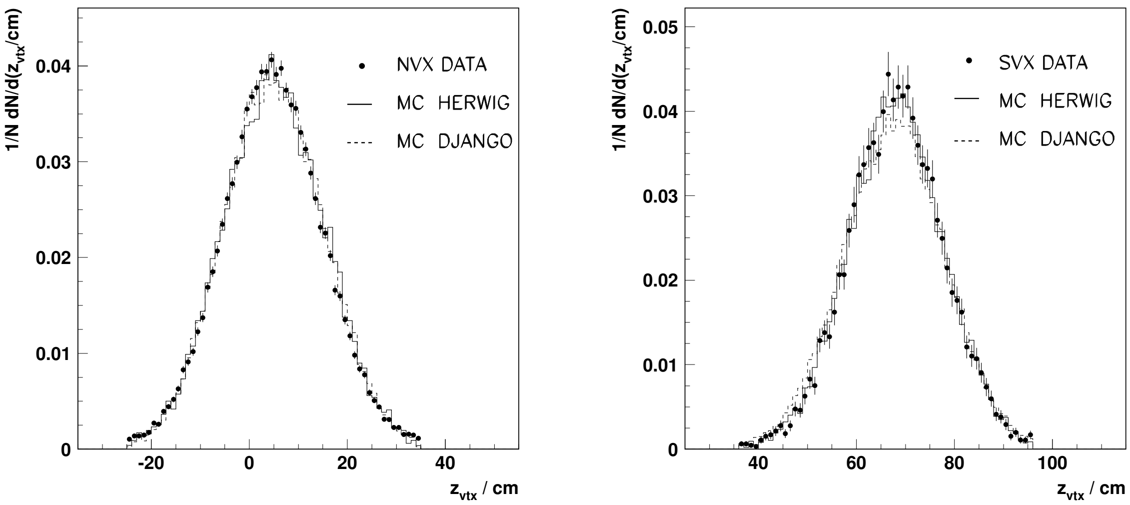

Figure 6.2: *Distributions of the z-coordinate of the reconstructed event vertex for the* NVX *and* SVX *selections. Shown are the data compared to MC simulation.*

- The determination of the event vertex, reconstructed using the charged particle tracks in the central jet chambers and the electron candidate hit in the BPC, permit the determination of the scattering angle θ of the electron. The reconstructed polar direction must be within the interval $157^o < \theta < 173^o$ for the NVX sample and within $164^o < \theta < 176^o$ for the SVX sample. Furthermore in order to ensure the full containment of the electro-magnetic shower in the BEMC, the radial coordinate of the hit in the BPC $r_{BPC} = (x_{BPC}^2 + y_{BPC}^2)^{\frac{1}{2}}$ should be within the range $15 < r_{BPC} < 60$ cm and additionally have $|x_{BPC}| + |y_{BPC}| > 18$ cm.
  The distributions of the reconstructed angles are shown in fig. 6.3.
  The electron identification in the BEMC is based on the combined information from the BEMC and BPC sub-detectors. The electron candidate is defined as the most energetic BEMC cluster having an energy weighted cluster radius (ECRA estimator) smaller than 4 cm and a BPC hit within a radius of 4 cm around the cluster center of gravity [85].
  The electron energy is required to be larger than 12 GeV, in order to suppress photo-production events with mis-identified electrons. The energy cut on the electron cluster ensures 100% trigger efficiency [86]. By requiring hits in the proportional

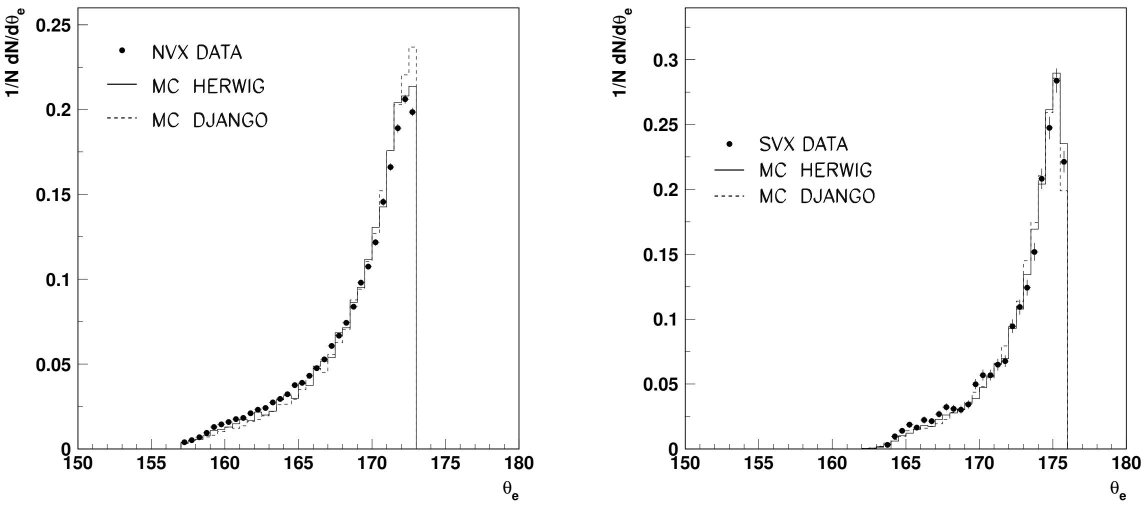

Figure 6.3: *Distribution of the electron scattering angle θ for the* NVX *and* SVX *selections. Data are compared to MC simulations.*

chamber corresponding to the BEMC cluster mis-identification of gammas as electrons is avoided. Figure 6.4 shows the energy distribution of the scattered electron.

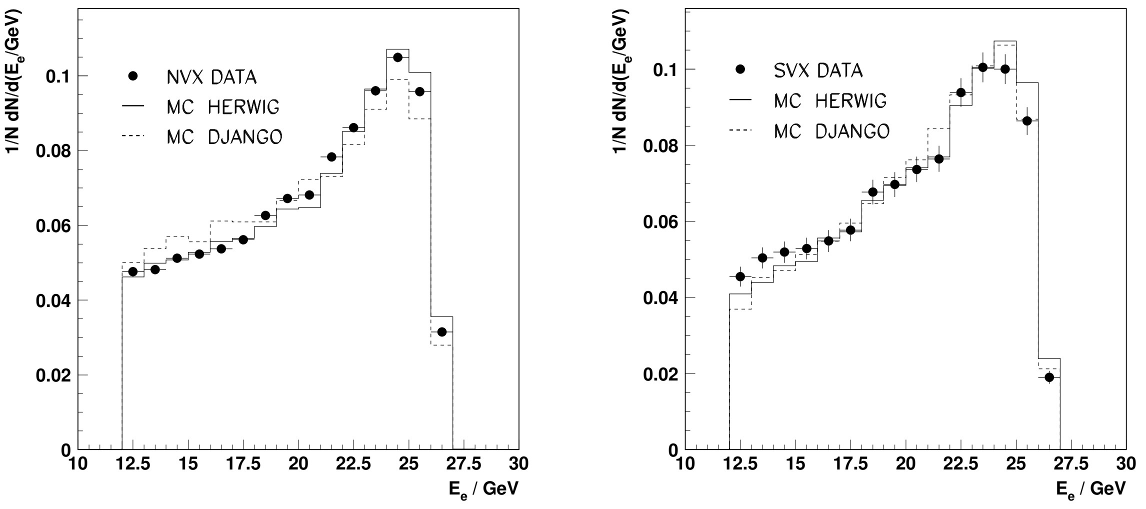

Figure 6.4: *Distribution of the scattered electron energy for the NVX and SVX selections. The data are compared to MC simulation.*

The event selection with the scattered electron in the BEMC ensures a DIS event selection with a transfered four momentum, $Q^2 < 100$ GeV^2 as is shown in fig. 6.1.

- The value of the total quantity $E - p_z$ reconstructed in the detector as $\sum_i (E - p_z)_i$ with i running over all calorimeter clusters, is required to be within the range $30 < E - p_z < 70$ GeV. The expected value for $E - p_z$ is $2E_e$ in which E_e is the electron beam energy and whereby the equivalence follows from energy and momentum conservation.
  Proton-induced background events can produce values of $E - p_z$ larger than 70 GeV which are suppressed by this cut. On the other hand, untagged photo-production events where the electron remains undetected in the beam pipe, may produce small values of $E - p_z$ and are efficiently rejected by the condition $E - p_z > 30$ GeV. The same is valid for initial state radiation (ISR) in which the interacting electron has an energy $E_e < 27.5$ GeV. Fig. 6.5 shows the $E - p_z$ distribution for the data and the MC simulations after all cuts are applied.

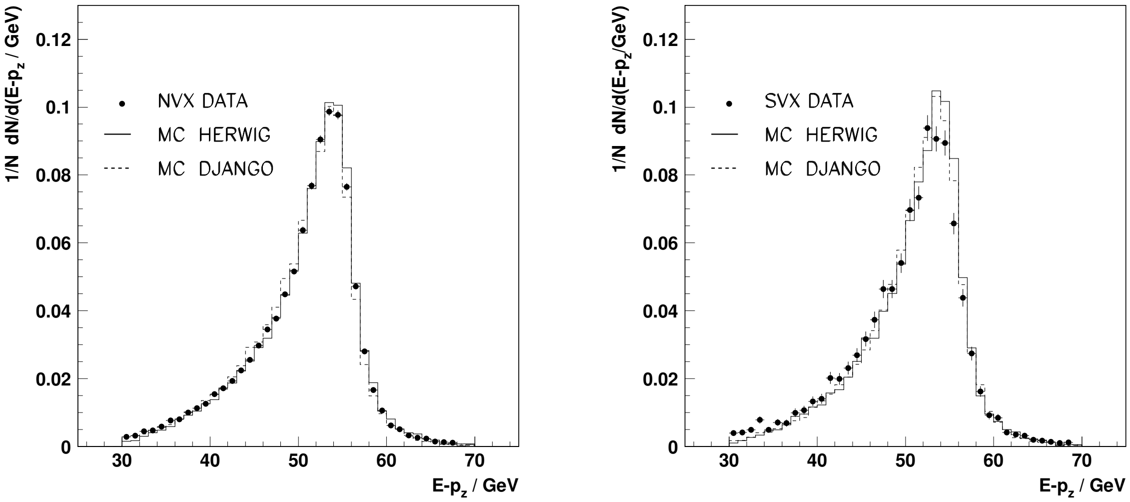

Figure 6.5: *Distribution of $E - p_z$ for the NVX and SVX selections. Shown are the data compared to MC simulations.*

- The rapidity gap events (ch. 3.4) are excluded by requiring more than 0.5 GeV between $4.4^o < \theta < 15^o$ in the calorimeter.

Cuts on the reconstructed kinematic variables

The kinematic variables introduced in ch. 2.1 can be evaluated with different reconstruction methods based on measurable quantities within the detectors. A review of the different methods can be found in [87].

In this work the determination of the event kinematic make use of the polar angle and energy of the scattered electron, and of the given nominal electron-beam energy (electron method). From the electron method follows:

$$Q_e^2 = 2E_eE_e'(1+\cos\theta_e) \tag{6.1}$$

$$y_e = 1 - \frac{E_e'}{E_e}(1-\cos\theta_e) \tag{6.2}$$

where E_e' is the energy of the scattered electron; the calculation of x follows from the relationship:

$$Q^2 = sxy \tag{6.3}$$

The Jaquet-Blondel method [36] using hadronic quantities and the double angle method have been considered for the cut on the invariant mass of the hadronic system and to check the consistency of the results.

In the phase space region considered, the electron method produces on average the better overall resolution on the determination of the kinematic variables and has been therefore used.

The cuts applied on the kinematic variables are as follows: on the invariant mass squared of the hadronic system W_e^2 [6], the cut $W_e^2 > 4400$ GeV^2 ensures, in general a certain level of hadronic activity in the detector. Furthermore in order to suppress events with radiative processes the same condition is applied to this variable calculated from hadronic quantity W_h^2. The distributions of $W_{e,h}^2$ calculated with the electron and the hadron methods are shown in fig.6.6. The different shape of the distributions of the variables W_e^2 and W_h^2 depend on the different detector acceptance and resolution to scattered electrons and hadrons.

The cut on W_e^2 and on the scattered electron energy $E_e' > 12$ GeV limit the variable y to within the interval $0.05 < y < 0.6$; the distribution of y in comparison with MC is shown in fig. 6.7. Finally the distributions of the kinematic variables x and Q^2 and the comparisons with MC simulations are shown in figure 6.8.

The selection cuts adopted constrain the kinematic variables x and Q^2 to within the range:

$$10^{-4} < x < 2 \cdot 10^{-2} \qquad 5 < Q^2 < 100 \text{ GeV}^2$$

in the case of the NVX data and between

$$4 \cdot 10^{-5} < x < 2 \cdot 10^{-3} \qquad 2.5 < Q^2 < 50 \text{ GeV}^2$$

for the SVX data sample (see fig. 6.10 and 6.11). In the latter sample the contamination due to photo-production 3%. These contributions have been estimated by MC studies in an analysis using identical cuts [83].

All the plots shown in this section present the comparison of data with the MC simulation. The different data distributions are on average well described by both shown simulation. This permits the correction of the data to the detector effects by using the simulated data as described in the following section.

Figure 6.9 shows the event display of a typical event selected using the presented criteria.

---

[6] The sub-script e indicates that the calculation follows from the electron variables

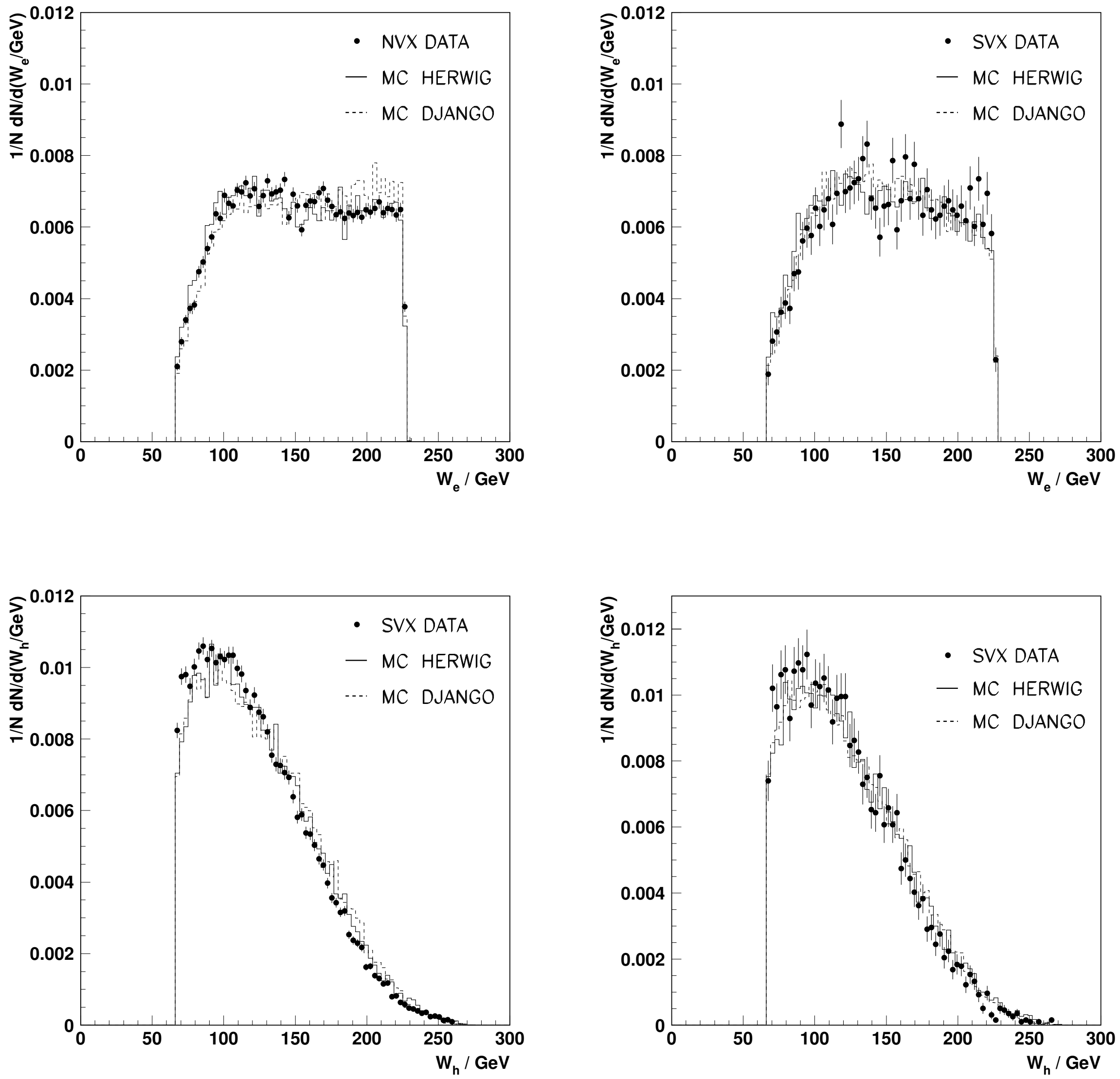

Figure 6.6: *Distribution of the invariant mass of the* $\gamma^* - P$ *system calculated from the electron variables* W_e *and from hadronic variables* W_h *both for the NVX and SVX selections. The data are compared with the MC simulations.*

6.2 Data corrections

The experimental measurements are always influenced by detector effects[7]. In order to correct data to detector effects and to estimate the error magnitudes, MC simulations are used as explained in the following.

---

[7] There are different effects which depend on detector characteristics as for example resolution, sensitivity, precision, linearity range and so on. All kind of detector characteristics and interplay determines the response function $R(x_1....x_n)$ of the detector.

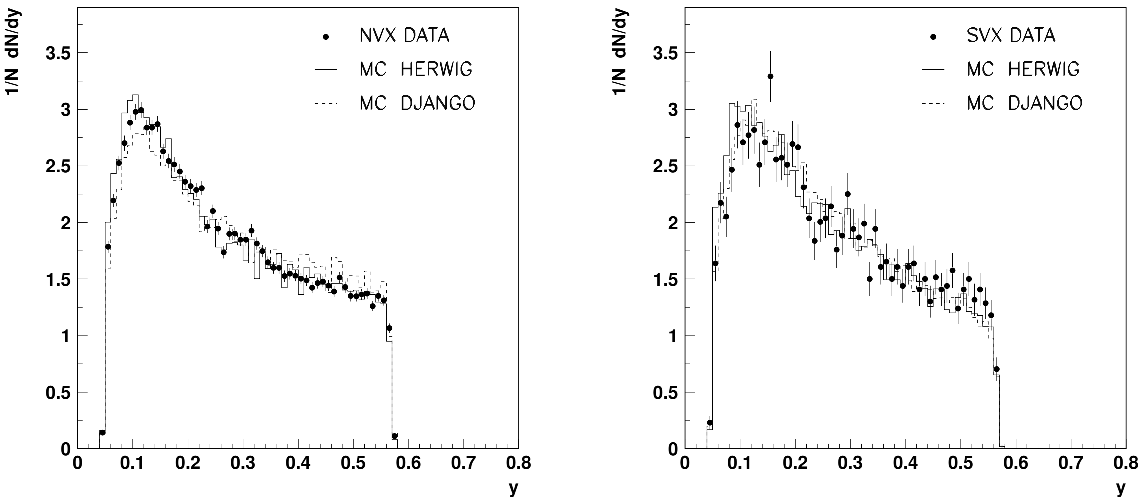

Figure 6.7: *Distribution of the kinematic variable y for the NVX and SVX selections. Shown are data compared to MC simulations.*

The corrected data are detector independent, therefore they can be compared with models, theories and eventually with other experimental results.
The correction procedure used here, takes into account detector effects and also the effects on the measurement produced by the radiative events. In the latter case the event kinematic may be wrongly reconstructed producing event migration between the phase space bins and thus distorting the measurements.
The detector effect can be evaluated using simulated data from a MC-model which describes the general features of the data. As shown in the previous section only in this case it is possible to use the measurement for comparison with theory, MC models or other experimental results. This is the case for the MC-models used in this work as shown in the previous section. The radiative corrections are performed with the DJANGO MC-generator[88] as illustrated in [83].
The measurements of physics variables is in general a derived measurement. Thus the measurement of the true distribution $f(u)$ of a physical variable u is performed by measuring the distribution $s(v)$ of the variable v which is typically a detector signal correlated with u. The relationship between the distribution at the detector level $s(v)$ and the true distribution $f(u)$ can be expressed using the following integral equation:

$$s(v) = \int R(u,v)f(u)du + b(v) \tag{6.4}$$

where the function $R(u,v)$ represents the response function of the detector and the function $b(y)$ the distribution of the background to the signal [89].
The problem consists therefore in the resolution of eq. (6.4) with respect to the function $f(u)$. In the real case the functions $s(v)$, $b(v)$ and $f(u)$ can have the form of discrete binned distributions. The numerical equation system associated with the equation 6.4

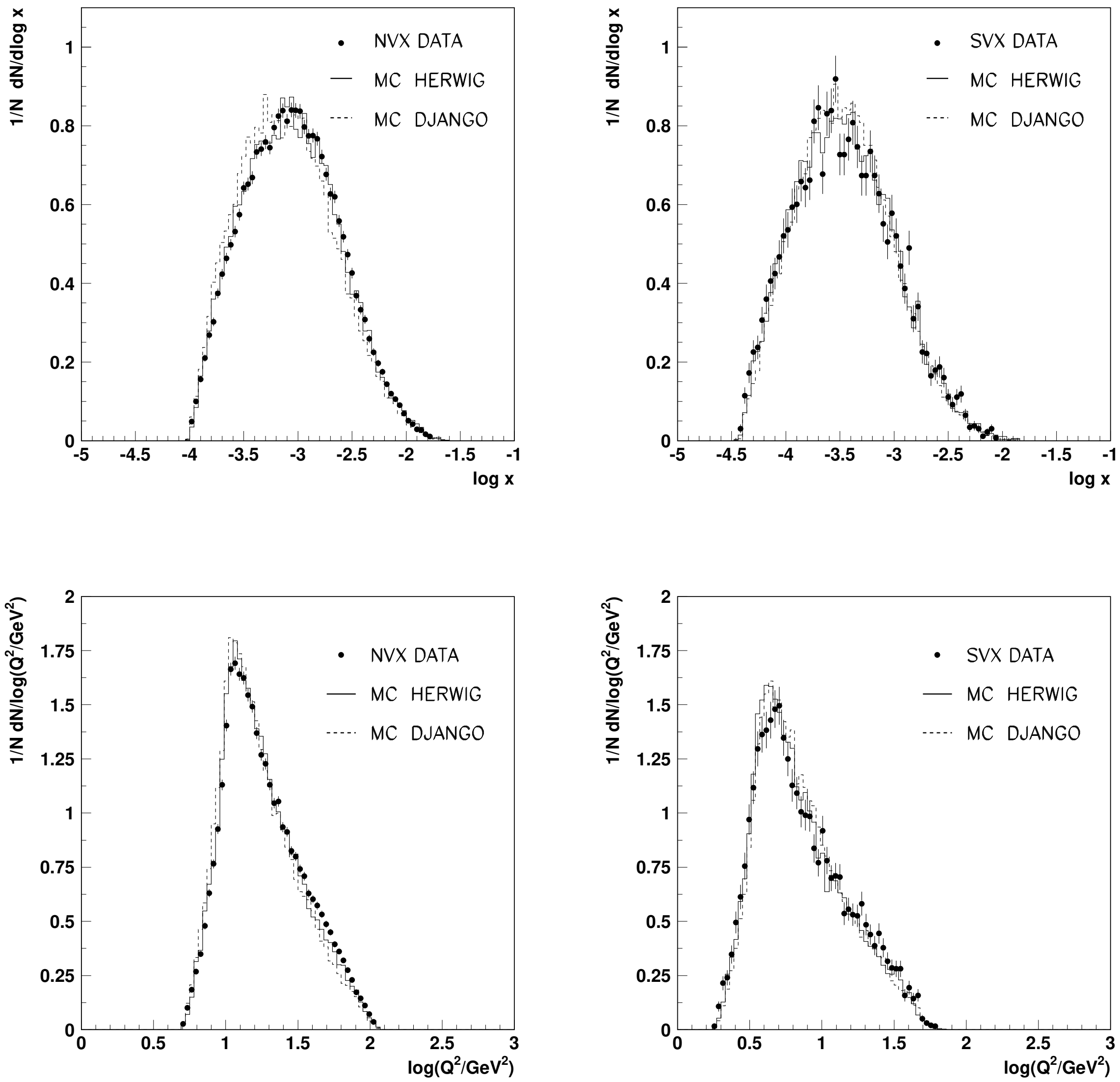

Figure 6.8: *Distribution of the kinematic variables x and Q^2 for both the NVX and SVX samples. The data are compared to MC simulations.*

reads:

$$s_k = \sum_i R_{i,k} f_i + b_i \qquad \text{with } (i,k = 1...n) \tag{6.5}$$

where *i,k* are bin indexes and n is the number of bins. If the measured signal v is well correlated with the variable u and the bin extension is not small with respect to the signal resolution, it follows that the non-diagonal matrix elements $R_{i,k}$ with $i \neq k$ can be set to zero to a good approximation. In this case the solution of the equation 6.5 is straight

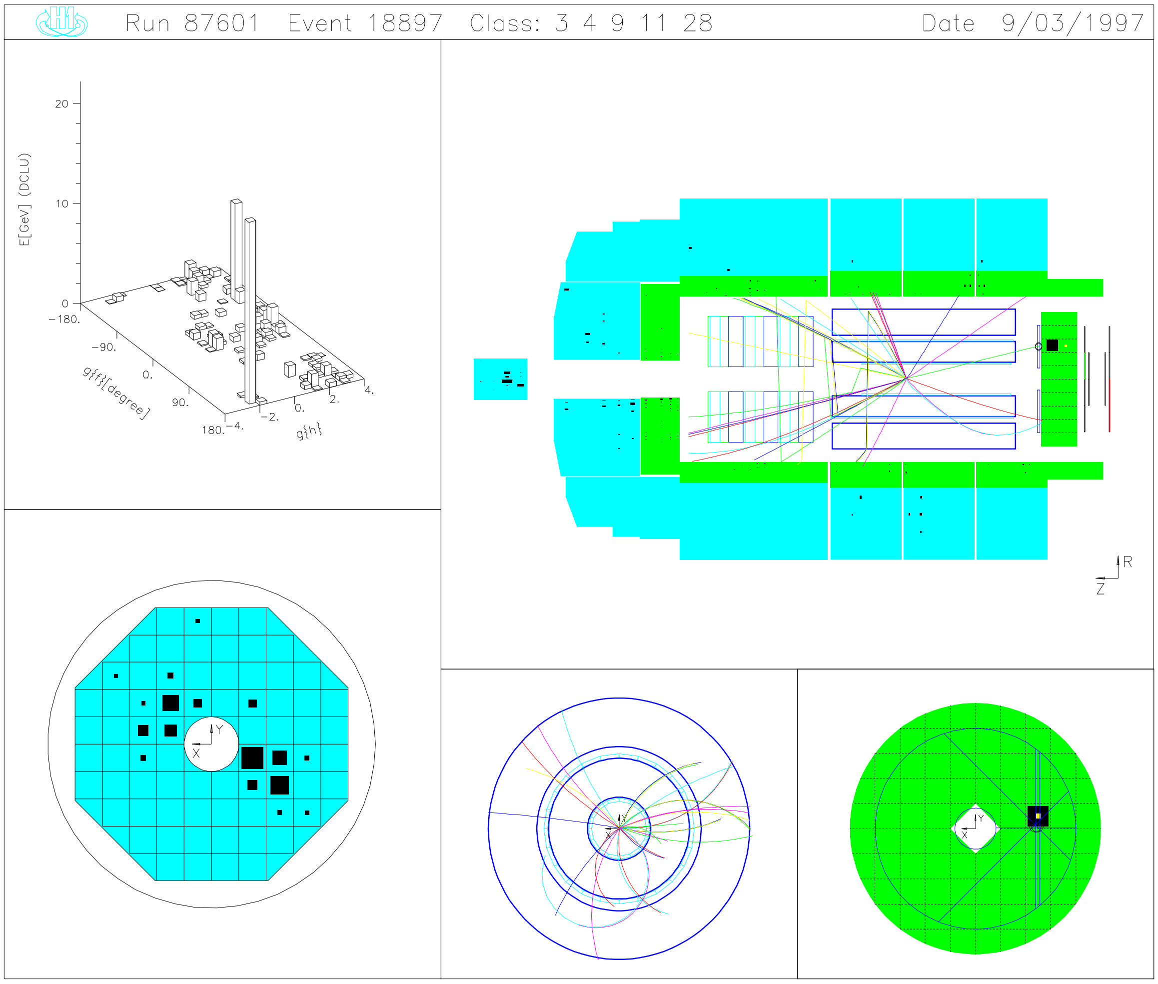

Figure 6.9: *Display of a typical DIS event (NVX selection). In the R-Z view (large figure) the response of PLUG, LAr, Inner Tracking Systems, BEMC and ToF are shown. On the right X-Y views are shown. In the upper corner the BPC superimposed to the BEMC and in the lower corner the sum of the 4 PLUG layers.*

forward:

$$f_i = \frac{s_k - b_i}{R_{i,k}} \qquad \text{with} \;\; (i = k = 1...n) \tag{6.6}$$

The factors $1/R_{i,i}$ can be calculated as the ratio: $1/R_{i,i} = f_i^{MC}/s_i^{MC}$ where s_i^{MC} and f_i^{MC} are calculated using MC simulated events.
The distribution value at the j-th of the n interval becomes:

$$f_j = (s_j - b_j) \cdot \frac{f_j^{MC}}{s_j^{MC}} \qquad \text{with} \;\; (j = 1...n) \tag{6.7}$$

6.3 Transverse energy flow

In this section the corrected differential distributions of the averaged transverse energy flow per event and pseudo-rapidity (η) units are presented. The measurement of this observable, performed in different sub-regions (bins) of phase space, is reported in this and in the subsequent section. It extends the existing published data [90, 91, 92, 93, 94] by adding results in a pseudo rapidity region [8] where no previous measurement has been ever performed.

The measurement of the transverse energy flow at HERA is motivated by the possibility to extend the knowledge regarding the parton dynamics within hadronic matter, in the low x region of the available phase space. The measurement of the proton structure function $F_2(x, Q^2)$ which rises steeply with decreasing x [95, 96] is compatible with the two different evolution equations (DGLAP and BFKL). The measurement of $F_2(x, Q^2)$ can be based only on the determination of the variables associated with the scattered electron, neglecting the properties of the hadronic final states. Thus it may not provide conclusive results in discriminating which evolution equation best describes the parton dynamics at low x, because of the missing information on the hadronic final stated.

It has been proposed [34, 98, 99, 100] that the hadronic final state in DIS events, might provide observables more sensitive to the parton dynamics than the structure function.

One example of a variable assuming different values in the case of the DGLAP and the BFKL approaches is the transverse energy flow in the central rapidity region between the current-jet and the proton remnant [101, 102].

Even more detailed information related to the hadronic final state in Deep Inelastic Scattering at HERA is given by the transverse energy flow as a function of the pseudo-rapidity. Starting from these motivations, the energy flow measurement is compared with the MC predictions from the models presented in ch. 2.4.

In previous DIS and e^+e^- experiments the properties of the hadronic final state were well described using the available MC models. Thus it is interesting to verify the predictions of the models in the new phase space region accessible at HERA as a test of the understanding of the hadronic matter with the present theory.

Phase space partition

In order to perform the energy flow measurement as a function of x for almost fixed Q^2 values, a partition in x and Q^2 as indicated in figures 6.10 and 6.11 has been chosen. On the figures which represent the kinematic plane, the angular acceptance and the major cuts on the event kinematics are indicated. Furthermore average values and the resolution[9] of the two kinematic variables used is shown within each phase space bin. The choice of the dimension of the interval $\Delta_i(x)$ and $\Delta_i(Q^2)$ should be larger than the errors $\sigma_i(x)$ and $\sigma_i(Q^2)$. This criterion limits the migration of events even between adjacent bins

---

[8] Towards the proton remnant fragmentation region

[9] The resolution for a kinematic variable v is calculated as follows: $\frac{\sigma(v)}{v} = \sqrt{\sum_i \left(\frac{v_i^{gen} - v_i^{rec}}{v_i^{gen}}\right)^2}$

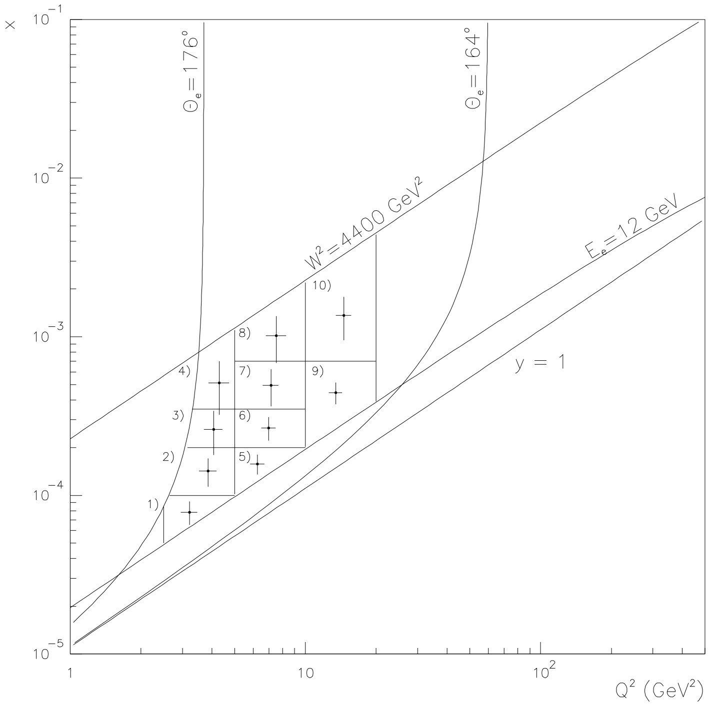

Figure 6.10: *Phase space partition for the SVX data sample. The sub-regions (bins) are indicated with the number from 1 to 10 and contain each one the point individuated by the average values of x and* Q^2 *calculated in the bin. The error bars represent the variable resolution multiplied by the variable average.*

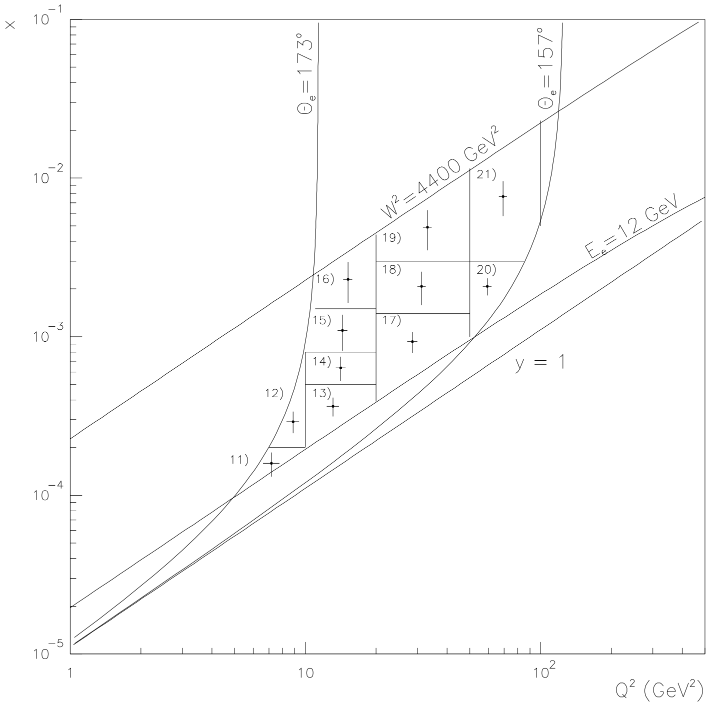

Figure 6.11: *Phase space partition for the NVX data. The bins are indicated with the number from 11 to 21. The average values of x and* Q^2 *calculated in each bin are shown with error bars representing the variable resolution multiplied the variable average.*

and ensures a large number of events per phase space bin thereby minimizing statistical fluctuations on the measurements [83].

Correction factors

According eq. (6.7) in order to correct the averaged transverse energy flow as a function of the pseudo rapidity, it is necessary to calculate the correction factors f_j^{MC}/s_j^{MC} depending on the detector response. This should be performed in each pseudo rapidity bin in which the transverse energy flow is measured. The correction factors are obtained by considering the MC simulation at the generator level and after the full detector simulation. The calculation of the factors, f_j^{MC}/s_j^{MC}, for the bin by bin correction for the transverse energy flow as a function of pseudo rapidity is performed using simulated events as follows:

$$\frac{f_j^{MC}}{s_j^{MC}} = \frac{\langle E_t^{gen}(\eta_j) \rangle}{\langle E_t^{rec}(\eta_j) \rangle} \tag{6.8}$$

where $\langle E_t^{(gen),(rec)}(\eta_j) \rangle$ indicate the average transverse energy in the interval η_j as generated by the MC (gen) or after the full detector simulation (rec).
In figure 6.12 and 6.13 the values of the factors are plotted for values of η between $-3 < \eta < 5$ corresponding to the maximal acceptance achievable with the H1 calorimeter systems. In each of the 21 plots, the last three points in the forward region between $3.5 < \eta < 5$ refer to the acceptance correction for the PLUG calorimeter. Their values decrease with increasing pseudo rapidity. For the pseudo rapidity bins 2 and 3 of the PLUG (see tab.5.4) the factors are close to unity being larger for bin 2 and smaller for bin 3. In the region affected by the largest amount of inactive material, pseudo rapidity bin 1, the factor is around 1.5 and is in general smaller for the phase space regions from 1 to 10 (fig. 6.12) in the SVX sample. Because of the acceptance shift (in the SVX sample) the pseudo rapidity interval $3 < \eta < 3.5$ is populated by both LAr and PLUG measurements. Two effects are responsible for the high values of the correction function in this pseudo rapidity bin: the de-population of the bin from LAr cells and population with PLUG cells mostly affected by the inactive material.

Measurement

The corrected transverse energy flow per event in the laboratory system is shown in fig. 6.14 for the SVX sample and in figures 6.15 and 6.16 for the NVX sample showing different MC models. The measurement in bin 21 (fig. 6.15 or 6.16) shows a transverse energy distribution strongly peaked around 0.5 pseudo rapidity units. The maximum E_t is around 5.4 GeV; the high value of E_t depends on the large transverse energy of the electron in the laboratory frame. It is evident that this enhanced peak structure tends to disappear for the phase space bin below 7 (fig. 6.15). In this phase space region (low x and Q^2 values) the distribution of the transverse energy flow appears almost constant within the interval $-1 < \eta < 3$. The average value is slightly below 2 GeV.
A comprehensive overview for the considered phase space is shown in fig. 6.17. In this

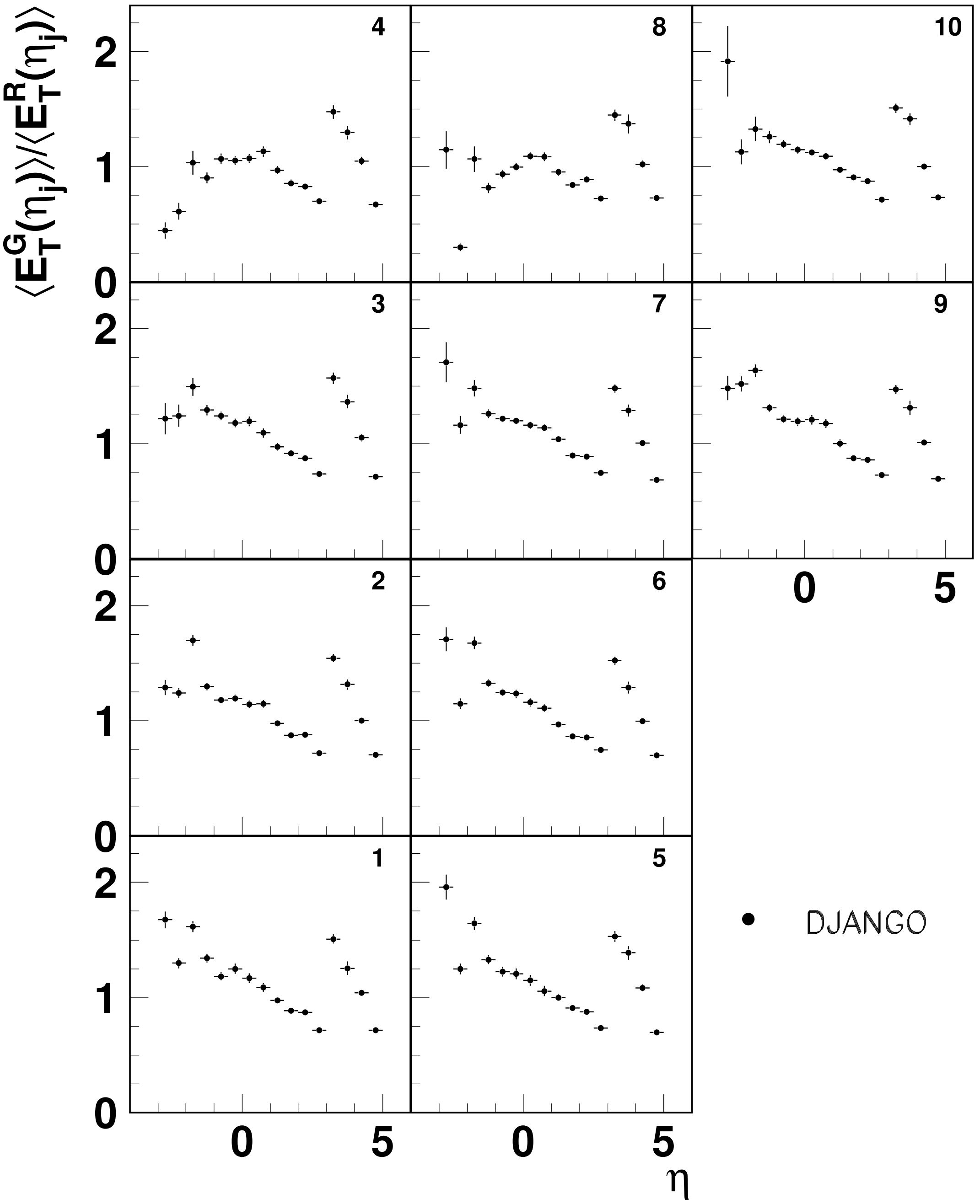

Figure 6.12: *Correction factors to the transverse energy flow for the η_j interval in the 10 bins of the phase space (SVX sample). Correction in the laboratory system.*

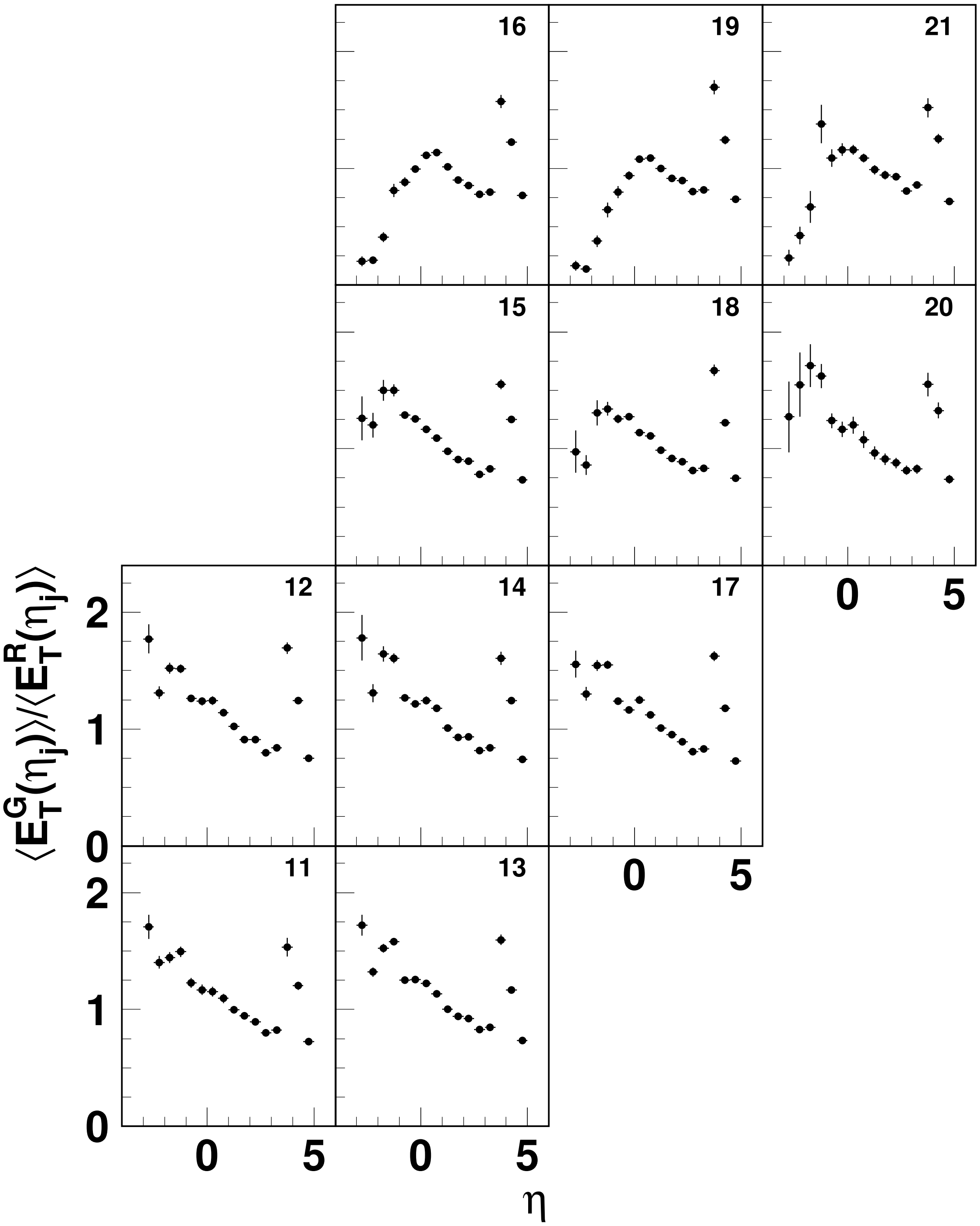

Figure 6.13: *Correction factors to the transverse energy flow for the η_j interval in the 11 bins indicated with the numbers (11...21) of the phase space (NVX sample). Correction in the laboratory system.*

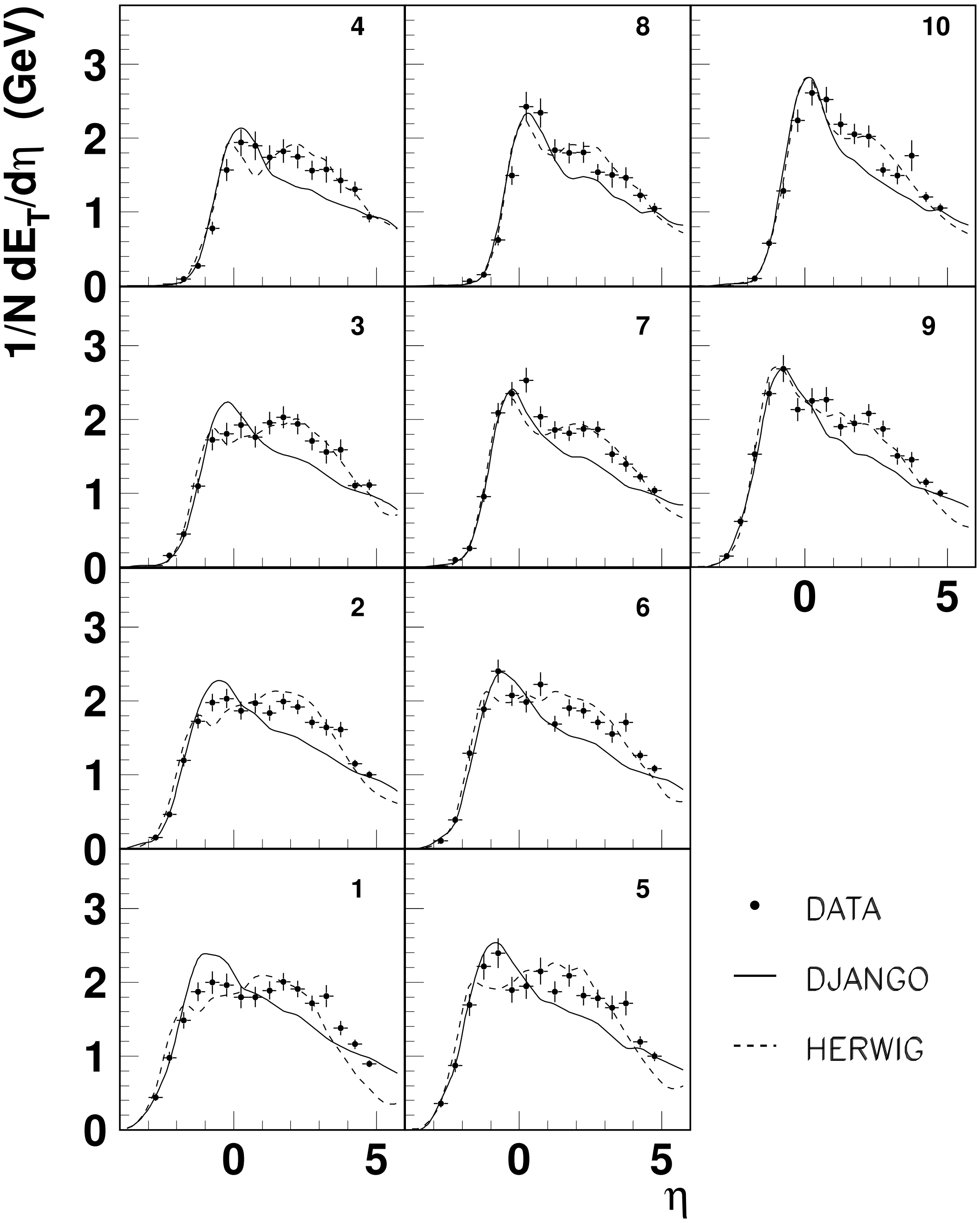

Figure 6.14: *The transverse energy flow as a function of the pseudo rapidity η in the laboratory system. The measurement concerns the SVX sample and the phase space partition as shown in fig. 6.10. The data is compared with the DJANGO and HERWIG MC-models. Only the statistical errors are shown.*

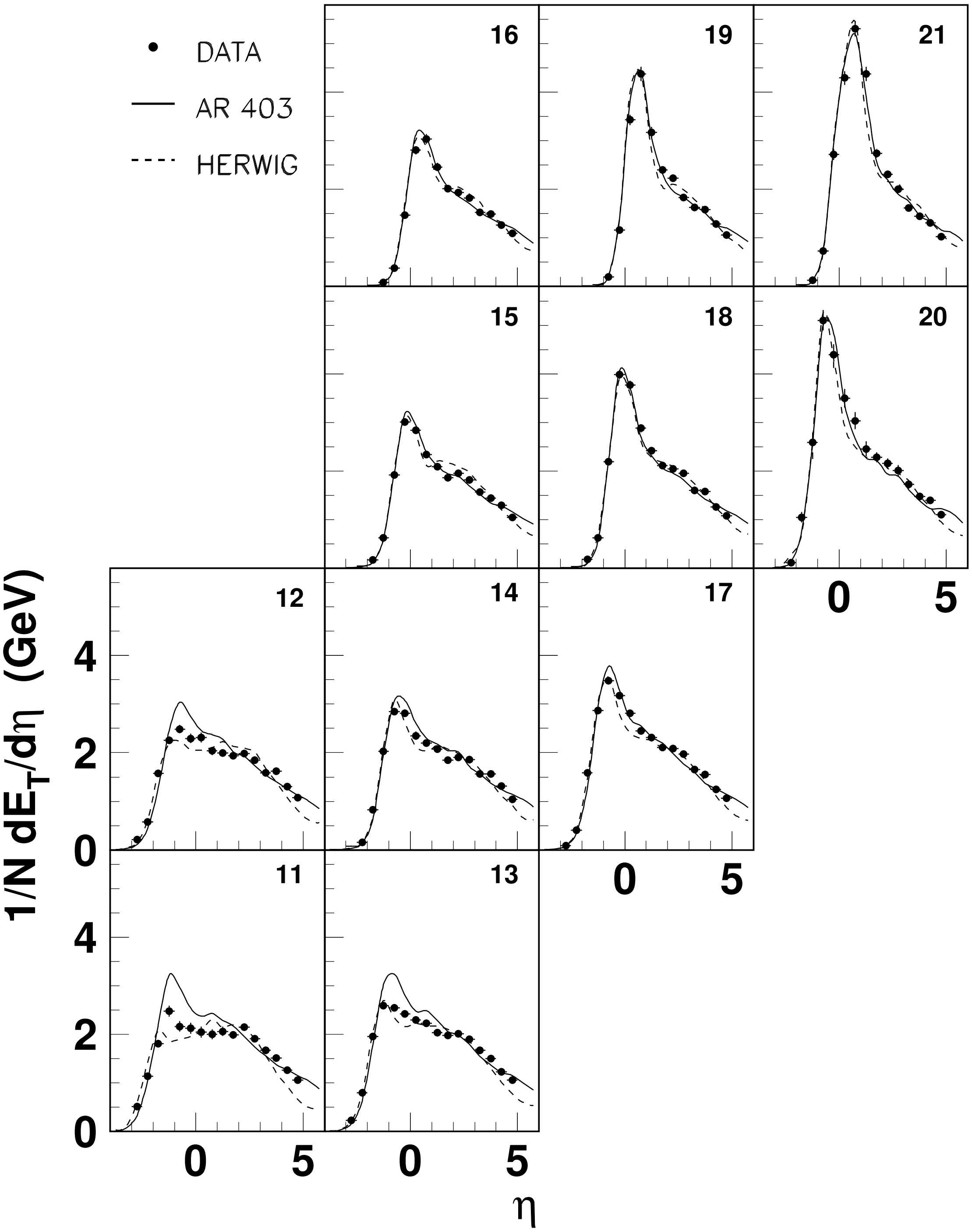

Figure 6.15: *The transverse energy flow as a function of the pseudo rapidity* η *in the laboratory system. The measurement concerns the NVX sample and the phase space partition as shown in fig. 6.11. The data is compared with the ARIADNE 4.03 and HERWIG MC-models. Only the statistical errors are shown.*

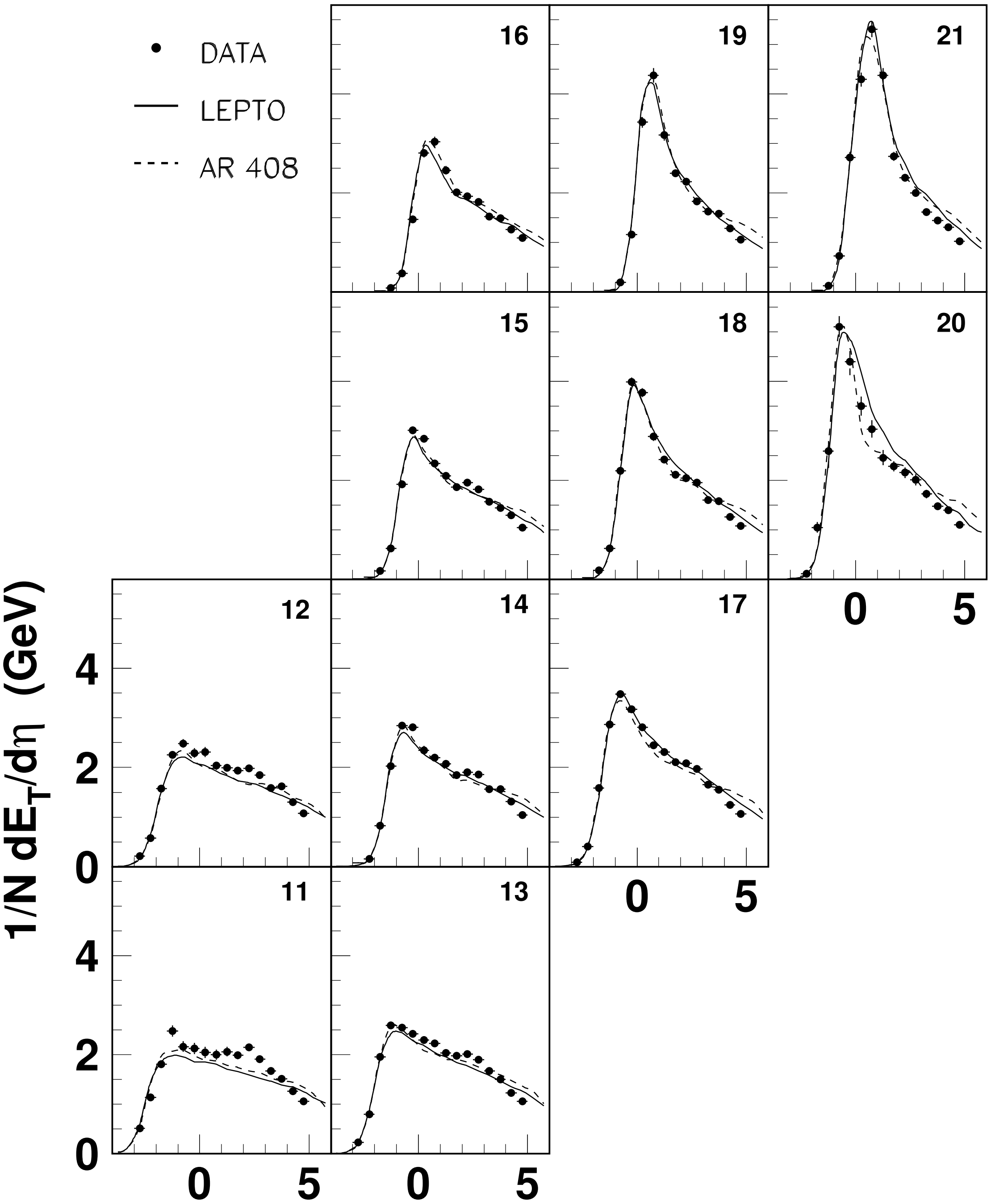

Figure 6.16: *The transverse energy flow as a function of the pseudo rapidity η in the laboratory system. The measurement concerns the NVX sample and the phase space partition as shown in fig. 6.11. The data are compared with the LEPTO6.5 and ARIADNE 4.08 MC-models. Only the statistical errors are shown.*

figure the PLUG measurement points are show with systematic and statistical errors added in quadrature. The evaluation of the systematic errors used in the last plots is performed in ch. 6.5.

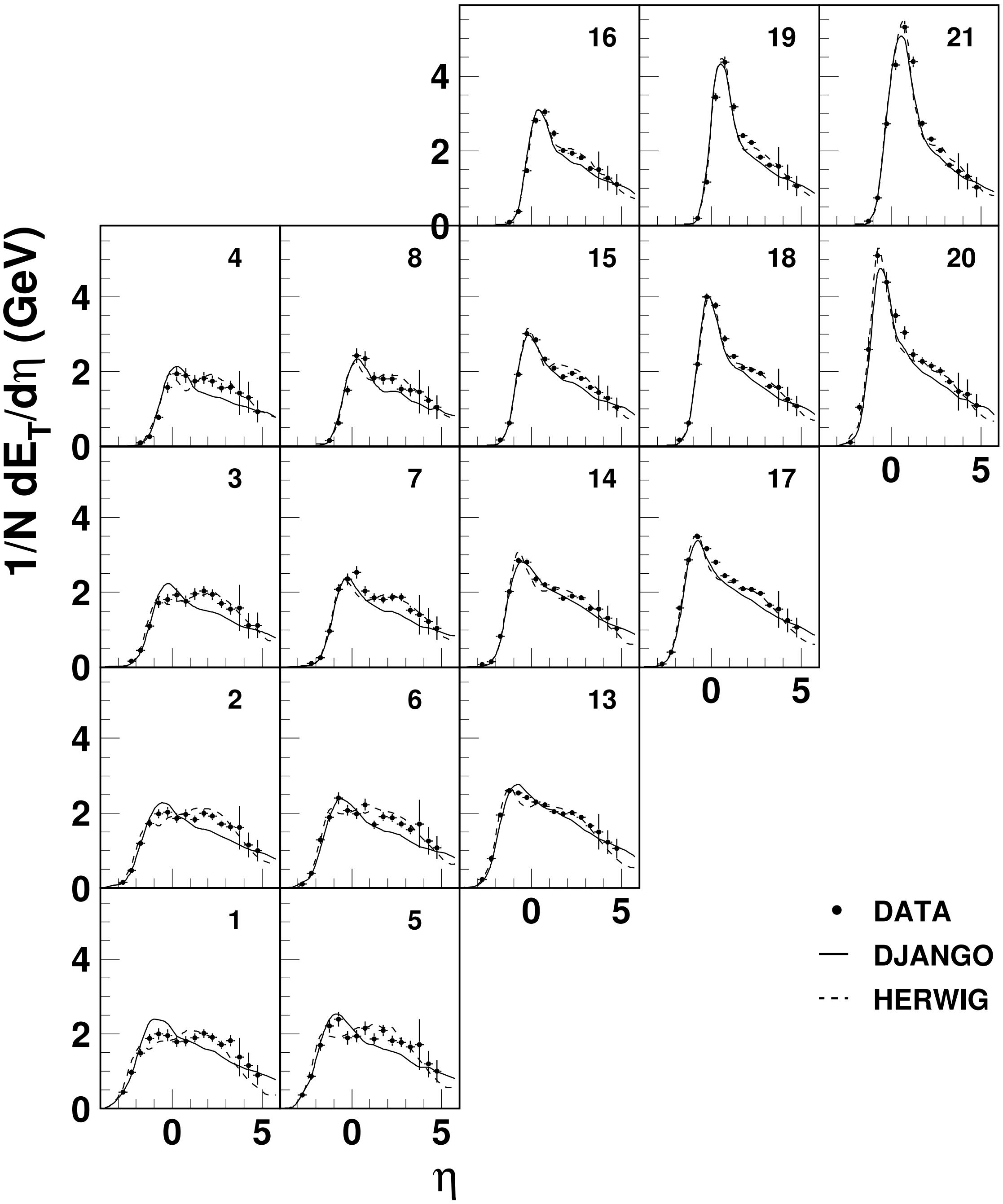

Figure 6.17: *The transverse energy flow as a function of the pseudo rapidity η in the laboratory system. The measurement concerns the NVX sample and the phase space partition as shown in fig. 6.11. The data are compared with the DJANGO and HERWIG MC-models. The errors on the PLUG measurement points include statistical and systematic contributions.*

6.4 Measurement in the hadronic center of mass system

The asymmetric momentum beams within of the HERA machine, make the use of a frame system different from the laboratory system worthwhile. In order to be able to compare the data with the theory or with other experimental results, the hadronic center of mass system (CMS) is the most natural choice for measurements concerning the hadronic final state. In fact in such a system the transversal component of the exchanged photon momentum is equal to zero. Thus the transverse energy measured depends only on the dynamic of the partons in the protons and not from the scattered electron transverse energy.

The hadronic center of mass system is the center of mass system of the the virtual photon γ^* and the incoming proton P.

This system moves within the laboratory with a velocity:

$$\overline{\beta} = \frac{\overline{q} + \overline{P}}{E_q + E_P} \tag{6.9}$$

calculated from the components of the 4-momentum $q \equiv (E_q; \overline{q})$ associated to the virtual photon and $P \equiv (E_P; \overline{P})$ to the incoming proton.

The direction of the z-axis in the CMS after the Lorentz transformation is defined by the direction of the virtual photon. With this choice the proton remnant lies within the negative region of the CMS pseudo rapidity η^*.

As in the case of the transverse energy flow measurement in the laboratory system, the correction factors for each interval of pseudo rapidity η^*, and for each of the 21 phase space sub-regions have been calculated using events simulated produced by the DJANGO MC. The results are shown in fig. 6.18 and 6.19. Since for each event the velocity $\overline{\beta}$ and consequently the Lorentz transformation may in general change, the acceptance of the detector in this frame may be shifted on an event by event basis. In the transition regions between the calorimeters the pseudo rapidity bin may not be totally filled. As a consequence, the factors can vary discontinuously from pseudo rapidity bin to bin and produce a non-reliable correction of the transverse energy in that bin. In such cases the correction factor and the associated measurement points have been excluded from the presented results. The excluded points around the boundary region between the PLUG and the LAr calorimeter are affected by the largest amount of inactive material. In this transition region the uncertainty on the correction is larger as quantified in the next section. The corrected transverse energy flow per event in the CMS is shown in fig. 6.14 for the SVX sample and in figures 6.15 and 6.16 for the NVX sample. The experimental results are compared with different MC-models. The difference between the model predictions for a certain interval of Q^2 (for ex. for $5 \leq Q^2 \leq 10$ GeV^2 are shown in the phase space sub-regions 13,14,15,16) increases with decreasing x, in particular in the negative pseudo-rapidity region η^* which is covered by the PLUG.

Figure 6.23 shows an overview of the transverse energy flow as a function of the pseudo-rapidity η^* over the full considered phase space. The measurements performed with the PLUG are shown with systematic and statistical errors added in quadrature. Even con-

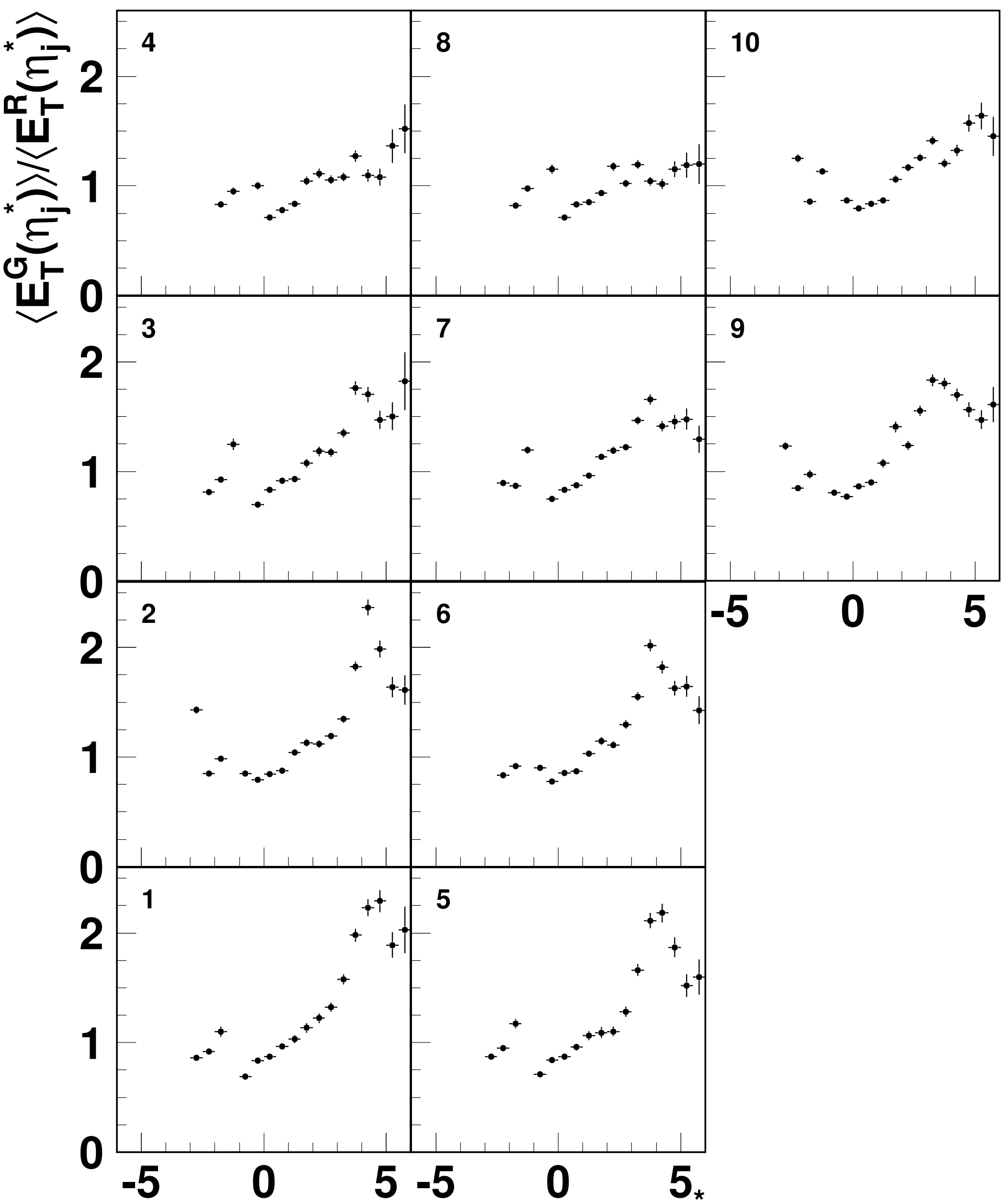

Figure 6.18: *Correction factors to the transverse energy flow for the* η_j^* *interval in the 10 bins of the phase space (SVX sample). Correction in the center of mass system.*

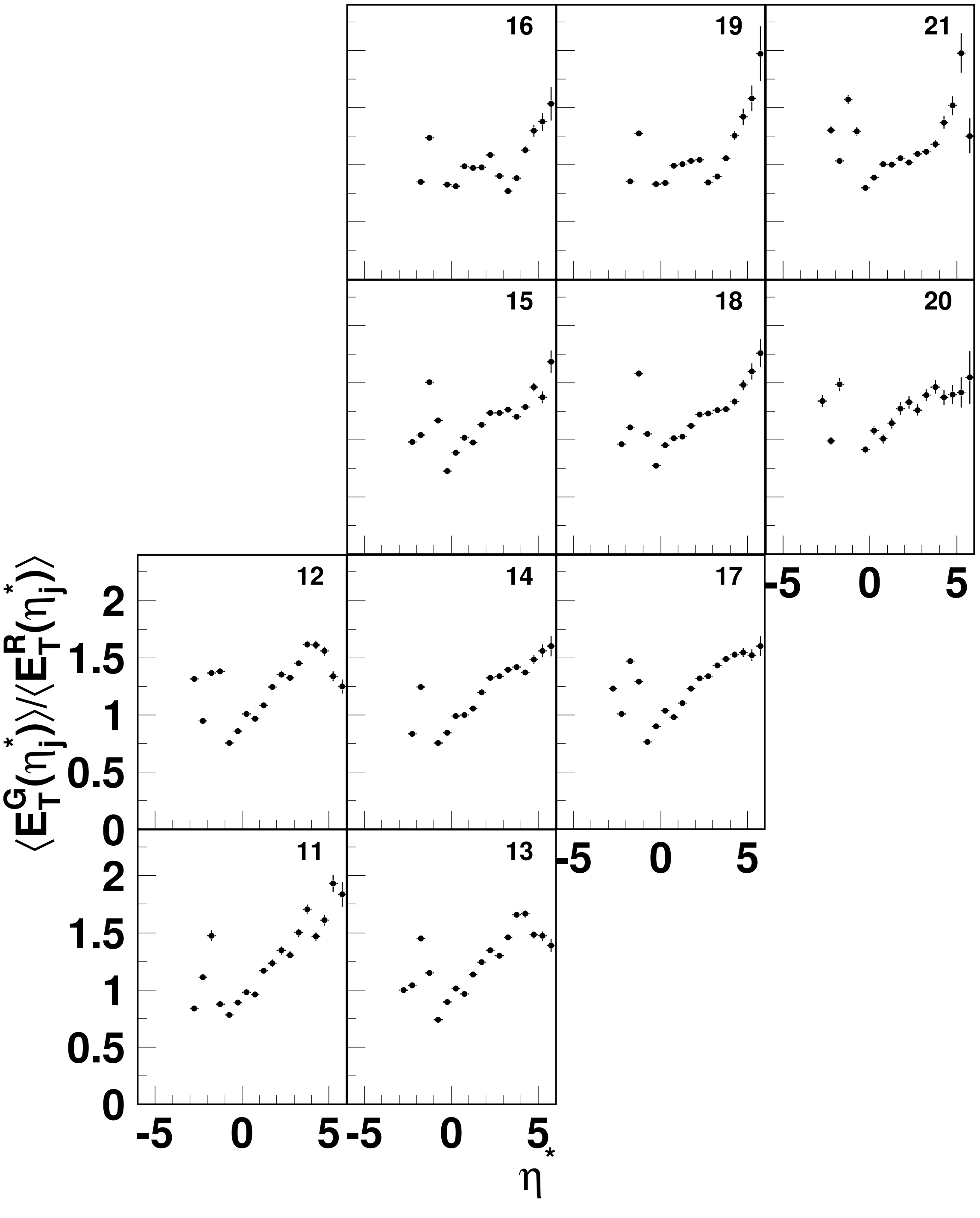

Figure 6.19: *Correction factors to the transverse energy flow for the η_j^* interval in the 11 bins indicated with the numbers (11...21) of the phase space (NVX sample). Correction in the center of mass system.*

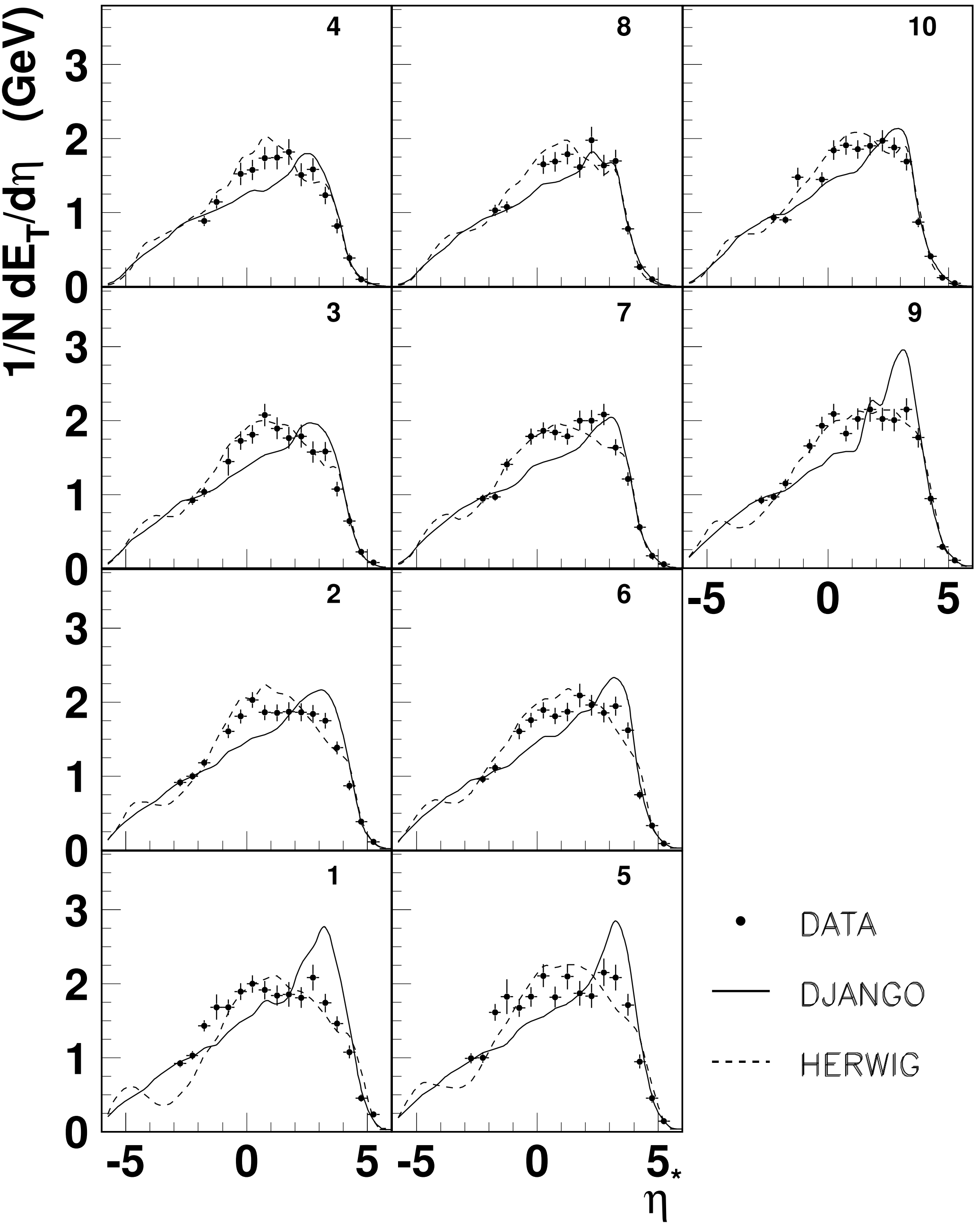

Figure 6.20: *The transverse energy flow as a function of the pseudo rapidity* η^* *in the center of mass system (CMS). The measurement concerns the SVX sample and the phase space partition as shown in fig. 6.10. The data is compared with the DJANGO and HERWIG MC-models. The statistical errors are shown.*

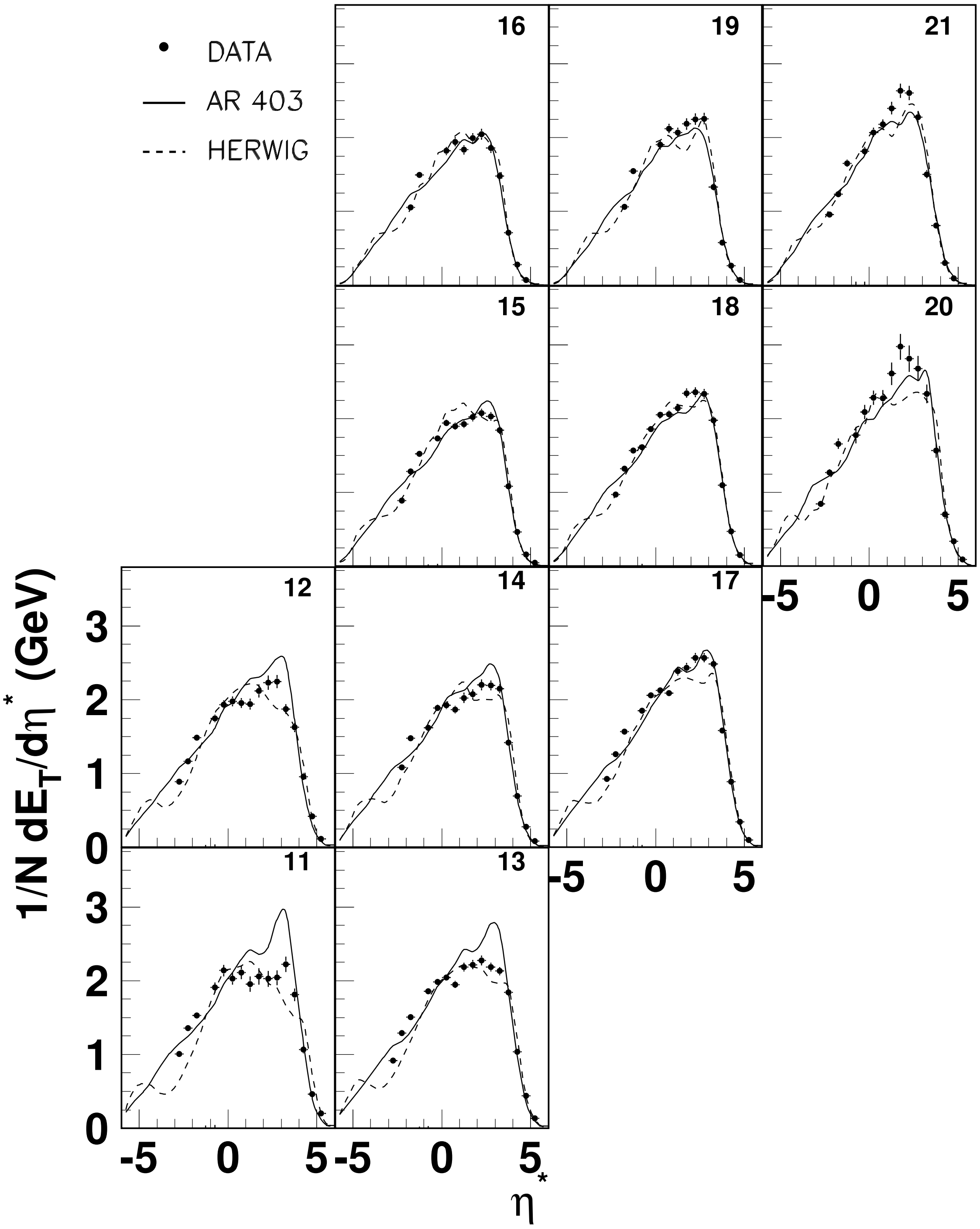

Figure 6.21: *The transverse energy flow as a function of the pseudo rapidity* η^* *in the CMS. The measurement concerns the NVX sample and the phase space partition as shown in fig. 6.11 The data is compared with the ARIADNE 4.03 and HERWIG MC-models. The statistical errors are shown.*

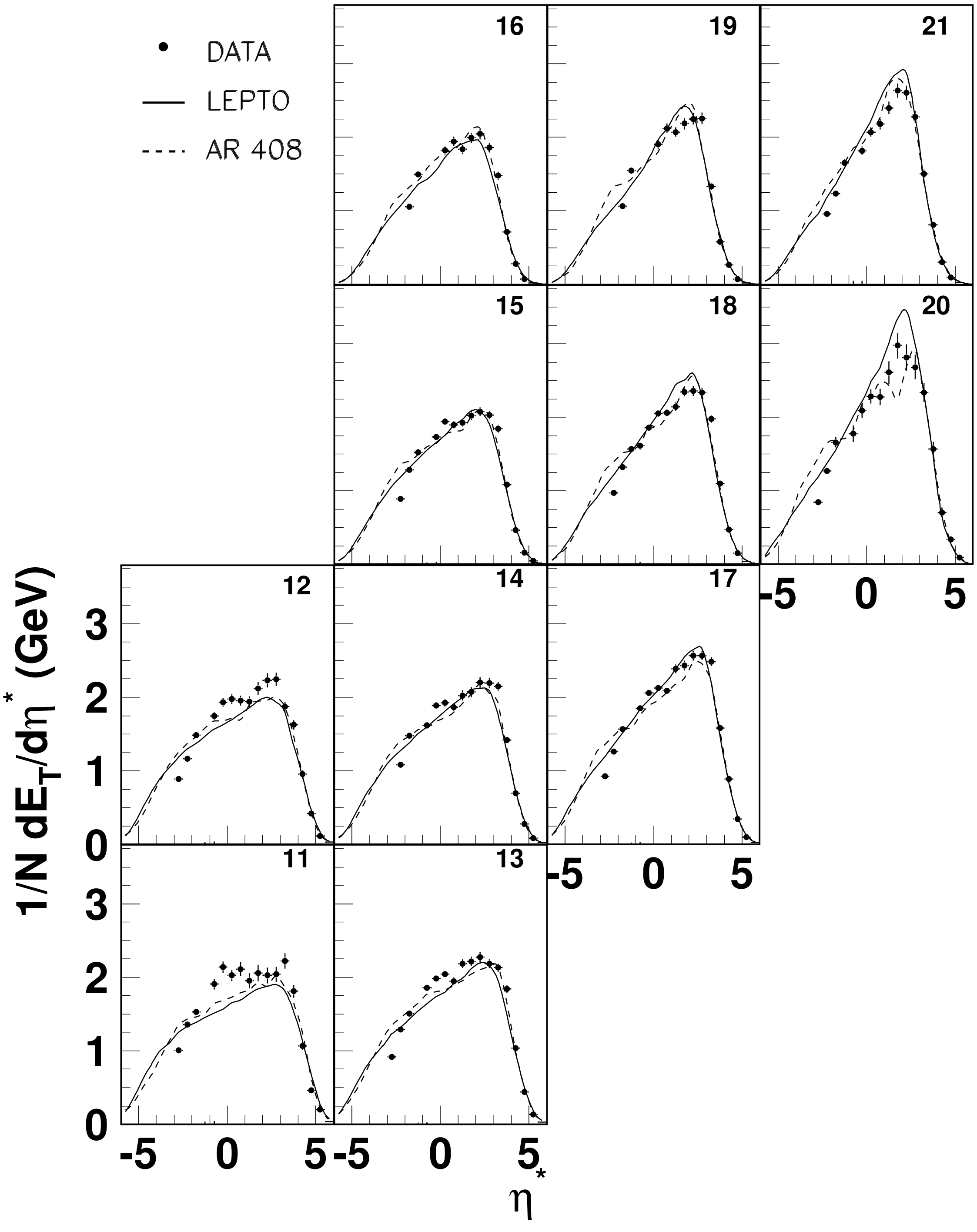

Figure 6.22: *The transverse energy flow as a function of the pseudo rapidity* η^* *in the CMS. The measurement concerns the NVX sample and the phase space partition as shown in fig. 6.11. The data is compared with the LEPTO and ARIADNE 4.08 MC-models. The statistical errors are shown.*

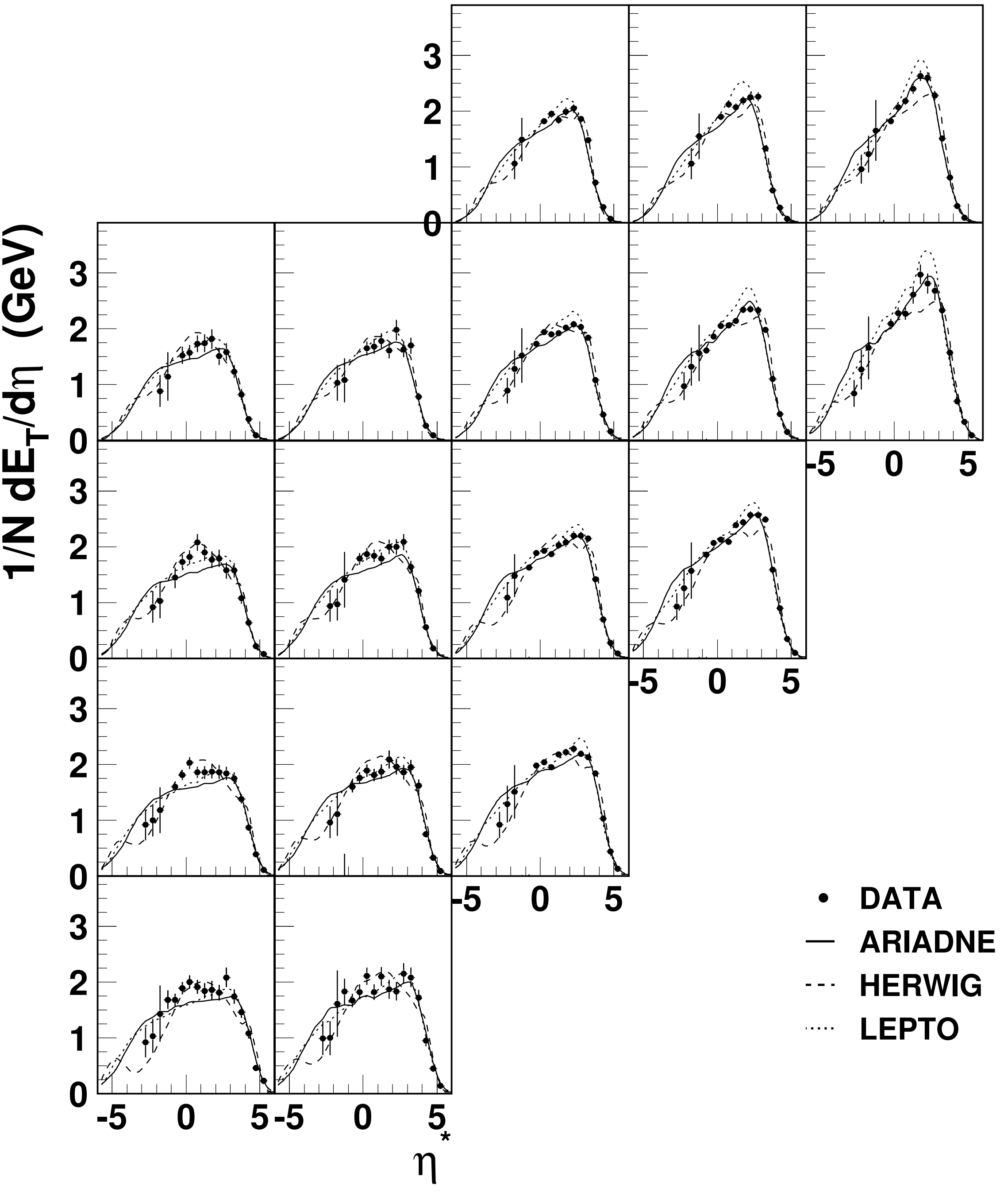

Figure 6.23: *The transverse energy flow as a function of the pseudo rapidity η^* in the CMS. The data is compared with the ARIADNE 4.08, HERWIG and LEPTO6.5 MC-models. The errors on the PLUG measurement points include statistical and systematic contributions.*

sidering the full error, the model implemented in HERWIG5.8d shows a better agreement to the experimental data than LEPTO6.5 and ARIADNE4.08.
With respect to that the interpretation of the results, assuming the MC models HERWIG and ARIADNE as in some sense representative of the DGLAP and BFKL evolution equations, indicates that the DGLAP perturbative approach even at this low value of x is fully compatible with the measurements presented here.

6.5 Systematic effects on the measurements

In this section systematic effects on the transverse energy flow measurement in the acceptance region of the PLUG calorimeter are summarized and a systematic error is evaluated. A detailed study of the systematic errors on the transverse energy measurements in the BEMC and LAr region has been performed elsewhere [83].

The first contribution to the uncertainty on the transverse energy flow is given by the error on the energy scale since $E_t = E \sin\theta$. The energy scale error has been evaluated in the ch. 5.3; its relative value $\frac{\Delta E}{E} = 0.084$ is constant over the three PLUG measurement points. The contribution due to the error on the determination of the energy deposition in the PLUG calorimeter cells, which enter in the E_t calculation because of the θ determination, depend on the precision of the shower simulation. This precision is mainly limited because the full simulated events used in the analysis are produced using the fast simulation (see ch. 5.4). Even if the energy of a shower is well reproduced in the simulated events, the cell multiplicity can not be exactly described by the fast MC. As a consequence the lateral dimension of the showers may be underestimated thus affecting the position determination (thereby the angle θ) of the energy deposition in the MC simulated events used for the corrections (ch. 5.5 and 6.2). This effect is estimated to be not larger than 1%.

The uncertainty of the inactive material correction has been investigated in ch. 5.8 using data from the SVX and NVX selections. The estimated value of the systematic error in the central region of the PLUG (bin 2) is 5%. The error value associated to bin 3 is assumed to be not larger than the value associated to bin 2. This is a reasonable assumption considering that the amount of inactive material affecting the bin 3 region is not larger, but even smaller than that affecting bin 2. From a conservative estimation 5% error is associated to the bin 3 too. According to the previous assumption an error value twice as large is associated to the region bin 1 since the amount of inactive material in front of this region is about a factor two than that in bin 2 (see fig. 5.10).

The dependency of the shower model on energy determination has been investigated comparing MC events generated with the Ariadne model and simulated using GHEISHA and Calor as shower transport codes (see ch. 5.4). The relative differences between the model in the different PLUG region are given in the table 6.1. As expected these effects are larger in the extreme sections of the calorimeter. In fact the different spatial energy distribution in the shower models influences more the calorimeter response in the PLUG sections where the energy leakage is large.

The MC-model dependency has been evaluated using the relative difference of the correction factors calculated in eq. 6.8 using DJANGO and HERWIG. Figure 6.24 shows the comparison of the factors over the total considered acceptance. The values associated to this source are given in table 6.1 too.

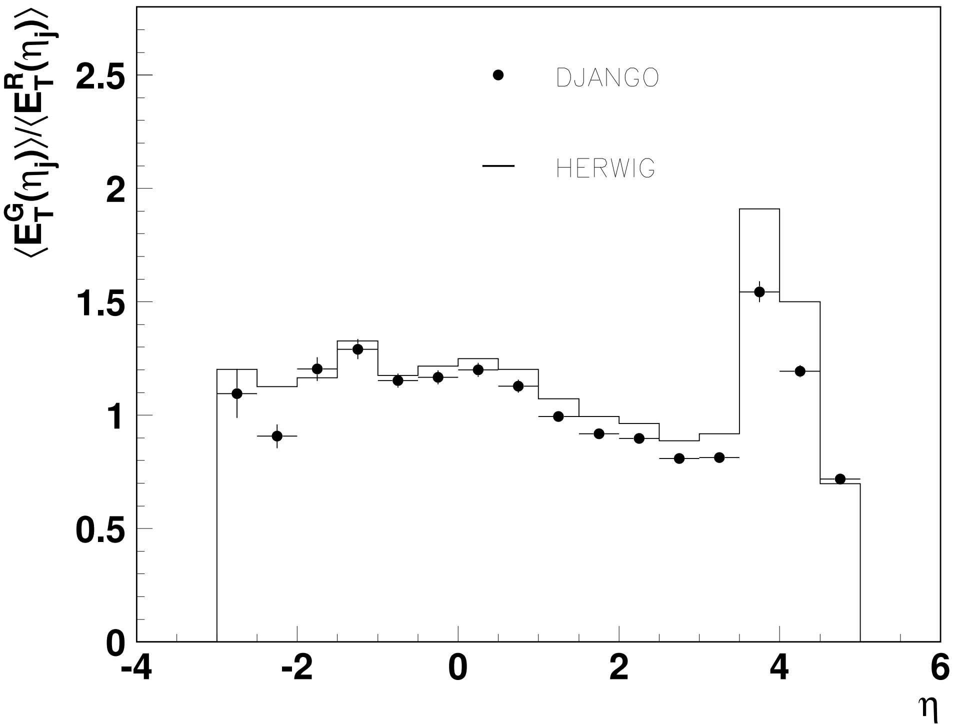

Figure 6.24: *Comparison of the correction factors obtained using two MC-models in the laboratory system. The relative difference between the corrections is large in the BEMC region because of the limited response to hadrons* $-3 < \eta < -2$*, and it is within 10% in the pseudo-rapidity region* $-2 < \eta < 3$*. The difference reach 20% in the acceptance region of the PLUG because of the inactive material and the difference in particle spectrum between the models.*

The noise and pile up effects discussed in ch. 4.6 have been subtracted from the signal according eq. 6.7. The fraction of transverse energy subtracted over the average measured value in the three PLUG regions is given in table 6.1.
In conclusion the systematic error on the transverse energy measurement changes from 31% to 23% in the different angular region of the calorimeter. The larger value of the error consistently corresponds to the region mostly affected by the inactive material.

PLUG section systematics			
error source	Bin 1	Bin 2	Bin 3
E-scale	0.084	0.084	0.084
$\sigma(\theta_{\langle n\rangle})/\langle\theta\rangle$	0.01	0.01	0.01
In. Mat. Cor.	0.10	0.05	0.05
shower code	0.22	0.10	0.20
MC-model	0.18	0.20	0.05
Quadratic sum	**0.31**	**0.24**	**0.23**
sub. pile-up	0.18	0.09	0.03

Table 6.1: *The different sources of error considered in the total systematic error evaluation of the transverse energy flow measurement using the PLUG calorimeter.*

Chapter 7

Summary and conclusions

In the present work general aspects of the H1 experiment at HERA have been presented. The main emphasis of the work was devoted to the forward silicon-copper sampling calorimeter called PLUG. It extends the calorimetry acceptance of the H1 detector by 1.5 pseudo-rapidity units. The purpose of this work was to demonstrate how the PLUG calorimeter can be used in the physics analysis of the deep inelastic scattering events. In particular the energy measurement of the hadronic final states in the region close to the beam pipe around the proton remnant has been presented in detail.

The most relevant technical aspects and the performances of the PLUG in the analysis of the *ep* scattering have been discussed. These aspects are: the calorimeter monitoring, the energy calibration, the simulation, the response linearity and the energy resolution within the configuration of H1. The energy-measurement performance, largely discussed in the fifth chapter, is strongly limited by the inactive material in front of the calorimeter. To permit the energy determination even in the presence of large amount of inactive material a energy correction has been developed. This correction technique is based on the complete simulation of DIS events in the H1 detector. The correction takes into account the uncorrected event energy measured in the PLUG (E_{rec}), its spatial distribution and the angular distribution of inactive material. The resulting corrected energy is optimized to reproduce the energy on an event by event basis. This achievement, which further permits the reconstruction of the shape of the distribution of the generated energy has been demonstrated using simulated events. The correlation plot between the energy generated within the PLUG angular acceptance versus the corrected energy in the same acceptance range demonstrate also the reliability of the correction on an event by event basis.
The PLUG energy resolution within H1 has been determined using DIS simulated events in the range between 10 and 110 GeV. From the resolution determination it follows that the energy measurement on a single event basis is possible for PLUG corrected energies from 30 to 110 GeV. In this energy window the resolution improves with increasing energy varying from 80 to 35 %. Since more than 50 % of DIS events are expected to have a PLUG energy within the given energy window, even the energy determination of forward jets within the PLUG seems feasible for future analysis.

For events with larger generated energy the calorimeter is affected by signal saturation (almost 40 % for event energy of 280 GeV) due to particle leakage from the calorimeter volume. For energies below 30 GeV, the resolution rises steeply to values much larger than 100 % because of the absorption of low energy particles in the inactive material. In such cases single event measurements are not practicable without change of the forward configuration of H1 and further corrections.

The most important result achieved in the analysis presented in chapter 6 is the transverse energy flow measurement of the hadronic final states in deep inelastic scattering.
The events belong to the region of the HERA phase space with $2.5 < Q^2 < 100$ GeV^2 and $10^{-5} < x < 10^{-2}$. The physics analysis starts from the events selection. The cuts depending on the detector, physics variables and event kinematics have been discussed and the related distributions for data and MC simulated events have been shown. The presented MC simulations demonstrate a general description of the data and permit the correction of detector effects on the measurements.
Data have been analyzed in both laboratory and center of mass (CMS) systems. The corrected transverse energy flow as a function of the pseudo-rapidity (η) measured using the PLUG calorimeter of the H1 detector has been presented. These represent the first measurements of this kind ever performed at such extreme pseudo-rapidity values.
The measurements cover the full H1 calorimeter system's acceptance. The part of the measurements performed exclusively with the PLUG are in the pseudo-rapidity regions between $3.5 < \eta < 5$ in the laboratory system and between $-3 < \eta^* < -1$ in the CMS.
The measurements in the center of mass system of the hadronic final states properties are easier to interpret than those in the laboratory system. In fact in the CMS the transverse momentum of the exchanged photon vanishes and does not contribute to the transverse energy of the hadronic final states. In this system the transverse energy of the hadrons reflects properties of the structure of the hadronic matter and of the parton dynamics within it.
Different MC models have been compared with the results of the measurements. From these comparisons and from the results on the tuning of MC simulation models to HERA physics [97] it follows that an agreement with the energy flow measurements can be reached using different models. For example, the simulation models: HERWIG and ARIADNE are flexible enough to describe fairly well data when adequately tuned.
These results even if affected by systematic error of about 25%, are useful in the fine tuning of MC models. Furthermore the presented measurements improve the detail of knowledge of the hadron structure in the very low x region of the phase space which is still considered one of the most important test fields for the QCD theory.

Bibliography

[1] W.C. Röntgen; "Sitzungsberichte der physikalisch-medizinschen Gesellschaft", Würzburg 1896.

[2] J.J. Thompson; Phil. Mag. 44 (1897) 33.

[3] R. Hofstadter; "Electron Scattering and Nuclear and Nucleon Structure", Benjamin, New York, 1963.

[4] E.D. Bloom et al.; Phys. Rev. Lett. 23 (1969) 930.

[5] R.P. Feynman; "Photon-hadron interactions", Benjamin, New York, 1972.

[6] Physics at HERA Vol. 1 and 2, proceedings of the workshop 1991; Ed. W. Buchmüller, G. Ingelman; Hamburg 1991.

[7] Future Physics at HERA Vol. 1, proceedings of the workshop 1995/96; Ed. G. Ingelman, A. De Roeck, R. Klanner; Hamburg 1996.

[8] H1 Coll., T. Ahmed et al.; Nucl. Phys. B429 (1994) 477.
H1 Coll., T. Ahmed et al.; Phys. Lett. B348 (1995) 681.

[9] E665 Coll., FERMILAB-PUB 93/065 E (March 93), NMC Coll., XII International Conference on Physics in Collisions, Boulder, Colorado, June 10-12 1992.

[10] C.G. Callan, D.J. Gross; Phys. Rev. Lett. 22 (1969) 156.

[11] J.D.Bjorken; Phys. Rev. 179 (1969) 1547.
J.D.Bjorken; Phys. Rev. 163 (1967) 1767.

[12] W. Panowsky, Proc. 14th Conf. on High Energy Physics, Vienna (1968) 23.

[13] J.P. Dishaw et al.; Phys. Lett. B 85 (1979) 142.
CDHS Coll., H.Abramowicz et al.; Nucl. Instr. and Meth. 180 (1981) 429.

[14] V.N. Gribov, L.N. Lipatov; Sov. J. Phys. 15 (1972) 438 and 675.
L.N. Lipatov; Sov. J. Phys. 20 (1975) 94.
G. Altarelli, G. Parisi; Nucl. Phys. B126 (1977) 298.
Yu.L. Dokshitser; Sov. Phys. JETP 47 (1977) 641.

[15] V.S. Fadin, E.A. Kuraev, L.N. Lipatov; Sov. Phys. JEPS 45 (1977) 199.
Ya.Ya. Balitsky, L.N. Lipatov; Sov. J. Nucl. Phys. 28 (1978) 822.

[16] G. Grindhammer; "Monte Carlo Generators for *ep* Physics ", Proc. of the work.:Physics at HERA, Vol 3, 1153, Eds W. Buchmüller and G. Ingelman, Hamburg (1991).

[17] G. Marchesini et al.; Comp. Phys. Comm. 67 (1992) 465.

[18] H. Bengtsson and T. Sjöstrand; Comp. Phys. Comm. 46 (1987) 43.

[19] G. Ingelman; "LEPTO version 6.1", Proc. of the work.:Physics at HERA, Vol 3, 1366, Ed. W. Buchmueller and G. Ingelman, Hamburg (1991).

[20] L. Lönnblad; Comp. Phys. Comm. 71 (1992) 15.

[21] L. Lönnblad; Z. Phys. C43 (1989) 625.

[22] L. Lönnblad; Z. Phys. C65 (1995) 285.

[23] T. Sjöstrand; Comp. Phys. Comm. 39 (1986) 347.
T. Sjöstrand and M. Bengtsson; Comp. Phys. Comm. 43 (1987) 367.
T. Sjöstrand; CERN-TH 6488-92 (1992).

[24] S. Wolfram; in Proc. 15th Rencontre de Moriond (1980), ed. J. Tran Thanh Van.
G. Marchesini and B. Webber; Nucl. Phys. B238 (1984) 1 B. Webber; Nucl. Phys. B238 (1984) 492.

[25] B.R. Webber; Ann. Rev. Nucl. Part. Sci. 36 (1986) 253.

[26] H1 coll. I. Abt et al.; Nucl. Instr. and Meth. A386 (1997)310.

[27] H1 Calorimeter Group, B. Andieu et al.; Nucl. Inst. and Meth. A336 (1993) 499.

[28] H1 Calorimeter Group ; B. Andieu et al.; Nucl. Inst. and Meth. A350 (1994) 57.

[29] H. Bethe and W. Heitler, Proc. Roy. Soc. A146 (1934) 83.

[30] N. Gogitidze, S. Levonian; "An Offline Luminosity Determination for the 1995 H1 e^+p Data ", H1 internal note H1-02/96-471.

[31] D. Handschuh; Dissertation, Universität Hamburg, 1993.

[32] C.W. Fabjan and R. Wigmans; "Energy measurement of Elementary particles", CERN-EP/89-64.

[33] T. Ferbel, "EXPERIMENTAL TECHNIQUES IN HIGH-ENERGY NUCLEAR AND PARTICLE PHYSICS", Addison-Wesley (1987).
K. Kleinknecht, "PARTICLE DETECTORS",Phys. Rep. 84,No.2,(1982),85.

[34] A.H. Müller; Nucl. Phys. B (Proc. Suppl.) 18C (1991) 125.

[35] J. Bartels et al.; "Associated Jet Production at HERA", DESY 96-036.

[36] A. Blondel, F. Jacquet, Pros. "Studies of an ep facility for Europe", Ed. U.Amaldi DESY 79/48 (1979) 391.

[37] ZEUS Coll., M. Derrick et al.; Phys. Lett. B 315 (1993) 481.

[38] H1 Coll., ; "A Search for Selectrons and Squark at HERA", DESY 96-082.

[39] U. Amaldi, Phys. Scripta 23 (1981) 409.

[40] C.J Fabjan, R. Wigmans;"Energy measurement of elementary particle", CERN-EP/89-64.

[41] R. Wigmans; "ADVANCES IN HADRON CALORIMETRY", CERN-PPE/91-39.

[42] M. Ruffer ($\equiv$ M. Seidel), Dissertation, Hamburg 1992, Internal Report DESY FH1K-93-01.

[43] Physical Review D "Particles and Fields", Part I (1994) Vol. 50.

[44] R. Wunstorf; "Untersuchungen zur Diodencharakteristik von Silizium-Oberflächensperrschichtdetektoren", Staatsexamarbeit, Universität Hamburg 1986.

[45] M. Bormann, et al.; Nucl. Inst. and Meth. in Phys. Res. A 257 (1987) 479.

[46] M. Bormann et al.; Nucl. Instr. and Meth. in Phys. Res. A 240 (1985) 63.

[47] E. Fretwurst et al.; Nucl. Inst. and Meth. in Phys. Res. A 288 (1990) 1.

[48] E. Fretwurst et al.;Nucl. Inst. and Meth. A 372 (1996) 368.

[49] G. Lindström; private communication.

[50] H. Neuert, "Kernphysikalische Messverfahren", Verlag G. Braun Karlsruhe 1966.

[51] M. Buck, "Monte-Carlo-Simulation zum Einfluss der Synchrotron-strahlung auf die Silizium-Detektoren des PLUG-Kalorimeters", Diplomarbeit Universität Hamburg 1996.

[52] R. Bernier, D. Breton, R.L. Chase, C. Pascaud: "H1 Calorimeter Electronics", Internal Report H1-07/92-237.

[53] K. Djidi: "DSP READ-OUT of ADC'S FOR THE H1 CALORIMETER", Internal Report H1-10/90-155.

[54] D.Breton et al.: "H1 Calorimeter Calibration Electronics", H1 internal note H1-04/92-219.

[55] F. Descamp, C. Vallee: "Data Acquisition fo the H1 Calorimeters", H1 internal note H1-10/92-256.

[56] W. Hildesheim, V. Riech, M. Seidel: "The Plug Calorimeter Users Guide", H1 internal note H1-08/94-372.

[57] G. Bernardi, S. Egli, C. Vallee; "ONLINE/OFFLINE Calorimetry Data Formats", H1-Software note number 18 february 1991.

[58] G. Bernardi, M. Jaffre, H. Kuester, Y. Sirois; "Calorimeter Reconstruction Banks, Modules and Reprocessing", H1-Software note number 14 december 1990.

[59] V. Blobel; The BOS-System, DESY Internal Report R1-88-01; Hamburg 1988.

[60] E. Panaro, M. Seidel; "Plug data reconstruction upgrade and hot channel monitoring", H1 internal note ,H1-10/94-399.

[61] M. Krueger; "Kalibration des Plug-Kalorimeters und Verbesserung des Signal-Rauschverhältisses", Diplomarbeit Universität Hamburg 1996.

[62] E. Panaro, M. Krueger, M.Seidel;"Calibration of the H1-Plug Calorimeter and comparison of Data with Monte Carlo Simulation", H1 internal note H1-09/95-455.

[63] H. Bueker; Halbleiterdetektoren für Kernstrahlung; Springer Verlag 1971.

[64] I. Fedder; "Untersuchungen an Silizium-instrumentierten Test-Kalorimetern für elektromagnetische und hadronische Schauer", Dissertation, Hamburg 1991.

[65] D.W.O. Rogers, Nucl. Instr. and Meth. 227 (1984) 535.
W.R. Nelson, H. Hirojama and D.W.O. Rogers, SLAC-265 1985.

[66] M. Eberle et al;" Electromagnetic MC-Simulations with EGS4 and GEANT - How to make them work for thin detectors - ", internal report H1-05/89-113.

[67] G. Lindström et al;"MC-Simulations with EGS4 for Calorimeters with Thin Silicon Detectors ", internal report DESY 89-104 (1989).

[68] H.C. Schleier; Diploma Thesis, Hamburg University 1992.

[69] M. Seidel; Diploma Thesis, Hamburg University 1989.

[70] R. Wigmans; Nucl. Instr. and Meth A259 (1987) 389.

[71] R. Wigmans; Nucl. Instr. and Meth A265 (1988) 273. R. Klanner; Nucl. Instr. and Meth A265 (1988) 200.

[72] F. Bruyant et al. "GEANT user's Guide", CERN Program Library Office, Jan (1993).

[73] J. Meyer et al.;"Guide for the H1 Simulation Program H1SIM", H1-Software note 3 (1989).

[74] H. Fesefeldt; "The simulation of Hadronic Showers - Physics and application ", PITHA 85/02 RWTH Aachen (1985).

[75] P.A. Aarnio et al.; FLUKA 89 Users Guide, CERN Program Library Office, (1990).

[76] HETC: Monte Carlo High-Energy Nucleon-Meson Transport Code, Oak Ridge National Laboratory RSIC Computer Code Collection CCC-178.

[77] MORSE: General Purpose Monte Carlo Multigroup Neutron and Gamma-Ray Transport Code with Combinational Geometry, Oak Ridge National Laboratory RSIC Computer Code Collection CCC-203.

[78] C. Zeitnitz, T.A. Gabriel; Nucl. Instr. and Meth. in Phys. Res. A 349 (1994) 106.

[79] M. Rudowicz;"Hadronische Schauersimulation für den H1 Detektor", Dissertation Hamburg 1992, MPI-PhE/92-14.
S. Peters;"Die parametrisierte Simulation elektromagnetischer Schauer", Dissertation Hamburg 1992, MPI-PhE/92-13.
M. Kuhlen;"The fast H1 Detektor Monte Carlo", Proc. of the XXVI HEP Int. Conf. Ed. J.R. Sanford Dallas 1992, Vol.2, 1787.

[80] G. Bernardi, W. Hildesheim, M. Kuhlen, M. Rudowicz: "Calibrated Energies", H1-Software note number 26 DESY october 1991.

[81] Z. Feng, C. Vallee: "Mapping function of H1 liquid argon calorimeter',
Internal Report H1-12/89-124.

[82] J. Ebert; private communication (FLOW+SPECTRA meeting).

[83] M.F. Hess,"Messung des transversalen Energieflusses mit dem H1-Detektor bei HERA", Dissertation, Hamburg 1996.

[84] U. Bassler, G. Bernardi, B. Gonzalez-Pineiro; "Events Classification for Neutral Current Events", H1-Software note 52 DESY 1995.

[85] U. Bassler, et. al.; "A Global DIS Event Selection for the 1993 Structure Function Measurement", H1-02/95-429 H1 internal note DESY 1995.

[86] T. Kurcă; The H1 Trigger for Neutral Current Deep Inelastic Scattering Events at Low Q^2 ; PhD Thesis Universität Hamburg 1993.

[87] S. Bentvelsen, J. Engelen, P. Kooijman; Proc. of the Work.:Physics at HERA, Vol.1, 23, Ed. W. Buchmüller, G. Ingelman, Hamburg (1991) and
K.C. Hoeger same Proc. Vol. 1, 43.

[88] G.A. Schuler, H. Spiesberger; Proc. of the Work.:Physics at HERA, Vol.3 1419, Ed. W. Buchmüller, G. Ingelman, Hamburg (1991).

[89] V. Blobel; "Unfolding methods in high-energy physics experiments", DESY 84-118 1984.

[90] H1 coll., T. Ahmed et al.; Phys. Lett. B298 (1993) 469.

[91] ZEUS coll., M. Derrick et al.; Z. Phys. C59 (1993) 231.

[92] H1 coll.,I.Abt. et al.; DESY 94-33 / Z. Phys. C63 (1994) 377.

[93] H1 coll., S.Aid et al.; DESY 95-108 / Phys. Lett. B356 (1995) 118.

[94] H1 Coll., I. Ahmed et al.; "Properties of Transverse Energy Production in Deep-Inelastic Scattering and comparisons to Monte Carlo Models", ICHEP' 96, Warsaw, Poland, July 1996.

[95] H1 collab. I. Abt et al.; Nucl. Phys. B407 (1993) 515.
H1 collab. I. Ahmed et al.; Nucl. Phys. B439 (1995) 471.

[96] ZEUS collab. M. Derrick et al. Phys. Lett. B316 (1993) 412.
ZEUS collab. M. Derrick et al. Z. Phys. C65 (1995) 379.

[97] N. Brook et al.; Proc. of the Work.:Future Physics at HERA, Vol.1 613, Ed. G. Ingelman, A. De Roech, R. Klanner Hamburg (1996).

[98] G. Marchesini, B.R. Webber, Nucl. Phys. B349 (1991) 617.

[99] J. Kwiecinski, A.D. Martin, P.J. Sutton ; Phys Rev D46 (1992) 921.

[100] M. Kuhlen ;"A new Method to Probe the Low x Parton Dynamics at HERA", MPI-PhE/96-10; hep-ph/9606246.

[101] K. Golec-Biernat et al.; Phys.Rev. D50 (1994) 217.

[102] K. Golec-Biernat et al.; Phys.Lett. B335 (1994) 220.

Acknowledgment

I would like to thank Prof. Dr. Dr. h.c. Gunnar Lindström who gave me the opportunity to join the H1 collaboration. Along the period of my permanence in Hamburg he supported me continuously making possible the realization of this work. With him also I would like to thank each one of his collaborators in the group of the Hamburg University for the help that they gave me and the friendly atmosphere that I enjoyed in the department. In particular I would like to acknowledge Dr. Volkhard Riech for his helpful suggestions and the reading of the manuscript. I want to acknowledge Dr. Eckhart Fretwurst and Dipl. Ing. Uwe Pein for the helpful explanations about the Silicon detectors. The results achieved in this work depend certainly also from their contribution to my understanding of PLUG detectors use and their technology.

It is a pleasure for me to acknowledge the colleagues with which I had the luck to share the working room during different periods along this time. Dr. Mattias Seidel who introduced me to the work connected to the PLUG calorimeter and the H1 collaboration, Dr. Gerald Lopez who helped me with discussion, suggestion and corrections to the thesis and finally Dr. Hannes Jung who took always the time to discuss with me and to answer all questions often of theoretical nature. I would like to thank each of them also for their particular friendship.

A special thank also to Dr. Tancredi Carli, Dr. Michael Kuhlen, Dr. Fabian Hess and Dr. Wolfgang Hildesheim who contribute in different way, but substantially to the development of this work.

I am indebted with almost every member of the Collaboration with which I had an active contact and the many student colleagues. I would like also to thank the DESY Directorium for the financial support and Dr. Eckhard Elsen for the hospitality in the FH1 group. Finally, I am glad to thank Susanne and Luca which always supported me in the difficult periods during these years.